Single Particle Dynamics of Anderson-like Impurity Models:

A Functional Renormalization Group Study

vorgelegt von

Ralf Hedden

aus Oldenburg (Oldb.)

Göttingen 2007

Abstract

Das Anderson-Störstellen-Modell ist ein generisches Modell, um Systeme zu beschreiben, in denen ein oder mehrere Energieniveaus an ein elektronisches Bad gekoppelt sind. Auf den Energieniveaus unterliegen die Elektronen einer Coulombwechselwirkung. Mögliche Anwendungsgebiete dieses Modells sind magnetische Atome in Metallen oder Systeme bestehend aus Quantenpunkten. Dieses Modell zeigt bereits für eine Störstelle interessante physikalische Eigenschaften, insbesondere den wohlbekannten Kondoeffekt. Bei zwei und mehr Störstellen werden die Eigenschaften des Systems im Bereich lokaler magnetischer Momente durch ein Zusammenspiel von Kondoeffekt und einer Kopplung der Spins auf den Störstellen bestimmt. Wegen des Zusammenspiels verschiedener Energieskalen stellt dieses Modell ein echtes Problem für jede mathematische Behandlung dar. Im Falle einer einzelnen Störstelle kann das Modell sehr effektiv mit Wilsons numerischer Renormierungsgruppe (NRG) behandelt werden. Da der numerische Aufwand der NRG exponentiell mit der Zahl der Störstellen steigt, kann sie im Allgemeinen nicht auf Systeme mit mehr als zwei Störstellen angewandt werden.

Die funktionale Renormierungsgruppe (fRG) ist in der Vergangenheit sehr erfolgreich auf Quanten-Störstellenprobleme angewandt worden [16]. In dieser Arbeit wird sie verwendet, um die Einteilchendynamik für Anderson-artige Quanten-Störstellensysteme im Gleichgewicht zu berechnen. Ein Vergleich mit der NRG im Fall einer Störstelle wird als Maßstab dienen, bevor Systeme mit zwei Störstellen und Quantenpunktsysteme mit zwei und drei Quantenpunkten untersucht werden. Das Zusammenspiel zwischen Kondoeffekt und magnetischer und orbitaler Ordnung wird in diesen Systemen untersucht werden. Obwohl die Abschneidevorschrift in dem hier verwendeten fRG-Schema durch Störungstheorie in zweiter Ordnung motiviert ist, liefert die fRG auch in den Fällen gute Resultate, in denen die Störungstheorie versagt. Im Allgemeinen wird sich zeigen, daß die fRG in der Lage ist, eine große Zahl verschiedener Anderson-Störstellen-Systeme zu behandeln, inklusive solcher mit asymmetrischen Energieniveaus und einer Wechselwirkung zwischen den Störstellen.

Abstract

The Anderson Impurity Model is a generic model to describe systems in which one or more energy levels are coupled to an electronic host. On the energy levels the electrons are subject to a Coulomb interaction. Possible applications of this model are magnetic atoms in a metal or quantum dot systems. Already for one impurity it displays very interesting physics including the well known Kondo effect. For two and more impurities the properties of the system in the local moment regime are determined by an interplay of the Kondo effect and the coupling between the impurity spins. Due to the interplay of multiple energy scales, this model poses a serious task for any computational tool. For a single impurity the model can be very efficiently treated using Wilson's numerical renormalization group (NRG). Since the numerical effort of NRG calculations rises exponentially with the number of impurities, generically it cannot be applied to systems with more than two impurities.

The functional renormalization group (fRG) has been very successfully applied to quantum impurity problems in the past [16]. In this work it will be used to calculate the single-particle dynamics for Anderson-like quantum impurity systems in equilibrium. A comparison to NRG in the case of a single impurity will serve as a benchmark before systems with two impurities and quantum dot systems with two and three dots will be studied. The interplay between the Kondo effect and magnetic and orbital ordering will be investigated in these systems. Although the truncation in the presented fRG scheme is motivated by second order perturbation theory, it will be shown that fRG works also in those cases where perturbation theory fails. Generally it will turn out that fRG is capable of treating a broad variety of Anderson impurity systems within the same framework, including asymmetric impurity levels and interaction between multiple impurities.

Contents

Chapter 1

Introduction

Almost all quantum many-body systems pose a considerable task to any theoretical method as soon as interaction comes into play. A huge variety of methods has been developed to calculate the properties of these systems. But although there are so many methods available, none of them can be used as a universal tool for all systems and for all applications. Especially perturbative methods can usually only focus on a specific energy window. This can either lead to divergences or to a lack of accuracy since multiple energy scales play an important role in the system under consideration. A general scheme, that has been very successfully applied to various quantum many-body problems in the past, is the renormalization group (RG) [1]. The idea behind this is to integrate out degrees of freedom in the high-energy region, avoiding infrared divergences and finally approaching the low energy region. The precise way of doing so depends on the specific system under investigation. In this work a RG scheme is used that has become known as functional Renormalization Group (fRG) [2]-[7]. It has successfully been applied to quite a number of many-body systems in the recent years [8]-[16].

In the systems that are investigated in this work the interaction is restricted locally. In this sense, they can all be considered as zero-dimensional interacting systems. They are all described by an Anderson-like Hamiltonian. That means that they consist of one or more energy levels, which are referred to as impurities, that are coupled to a bath of non-interacting electrons. The electrons from the bath can hop onto the impurities, where they will be subject to a Coulomb repulsion. This kind of models describes a rather general quantum impurity situation. Experimentally such a situation can be found when an atom with a partially unoccupied $d-$ or $f-$orbital is deposited in or on a metallic host,

like $Cr-$atoms on Au [64]. Another situation, that can be described by such a model, is a quantum dot structure, where electrons can hop in and out of the dot, while interacting only on the dot (charging effects).

Such systems of only locally interacting electrons seem to be very simple on first sight, but they display very rich physics and have all ingredients to pose a real quantum many-body problem. Their behaviour is governed by the interplay of different energy scales. With only a single impurity the model is called 'Single Impurity Anderson Model' (SIAM) and was suggested by Anderson in 1961 [19]. For large interaction strengths it can be mapped to the Kondo model by a Schrieffer-Wolff-transformation [20]. The Kondo model was suggested by J. Kondo in 1964 to describe anomalous behaviour of the resistivity at low temperatures [21]. This behaviour has been traced back to a magnetic moment of the impurity that is locally screened by the conduction electrons. It took until the seventies that Wilson's Numerical Renormalization Group (NRG) allowed to solve these models at least numerically [23].

For more than one impurity the situation is even more complex. If two or more impurity levels are coupled to the same host, an indirect interaction comes into play. This so-called RKKY-interaction leads to a coupling of the spins on the different impurity levels. Especially in the case of two impurities the question arises, whether individual magnetic moments survive and are Kondo screened or if both impurities form a singlet state.

Wilson's NRG is still the best tool to solve Anderson impurity systems. Unfortunately, the numerical effort rises exponentially with the number of correlated degrees of freedom in the model. A system with two impurities is treatable with NRG, generally a system with three impurities is already too complex. The structure of the functional RG used here is such that the numerical effort of this method does not rise exponentially but only with a power-law at worst. To be more precise, the numerical effort is directly related to the number of diagrams needed to perturbatively calculate the self-energy and the two-particle vertex function. This allows more complex systems to be investigated. It is possible to examine systems with one, two and three impurities. This work will focus on dynamical one-particle properties as the self-energy and the impurity spectral function but some static observables will be calculated as well. Only systems in equilibrium and at $T = 0$ will be studied.

First a brief derivation of the functional RG scheme used in this work will be given. The method used here has a field theoretical basis, using a generating functional for the partition function of the studied system. After introducing a cut-off into the free propagator,

an exact infinite hierarchy of flow equations will be derived. Here a scheme using one-particle irreducible vertex-function will be employed. For practical use the hierarchy will be truncated such that only an equation for the self-energy and for the two-particle vertex will remain. In this approximation these equations will be the basis for all functional RG calculation in the following chapters. The resulting self-energy will allow for the calculation for the single-particle dynamics of the quantum impurity systems.

In the next chapter the functional RG is applied to the Single Impurity Anderson Model. The model will be presented in some detail and flow equations for the self-energy and for the two-particle vertex will be derived for this special model. In the particle-hole symmetric case the self-energy and impurity spectral function will be presented and compared to the one computed with second order perturbation theory in the interaction strength and with NRG. Compared to perturbation theory, the result from fRG calculations will turn out to be a clear improvement in the low energy region. In the asymmetric case the occupancy of the impurity level will be calculated in addition to the dynamical properties mentioned before. A calculation of the impurity static spin susceptibility is presented. It will be shown that the fRG can be used to obtain reliable data as long as the interaction strength does not get too large. It will turn out that while the perturbative result is satisfying only in the symmetric case the fRG calculations work equally well in both cases. At the end of this chapter further approximation schemes motivated by perturbation theory will be discussed. Especially one scheme will be presented that combines most of the benefits with a largely reduced numerical effort.

Chapter 4 will deal with the two impurity Anderson model. Two different electronic hosts will be studied. In the first case the two impurities are coupled to a single non-interacting one-dimensional tight-binding chain. It will turn out that the fRG scheme works as well as in the one impurity case. The self-energy and impurity spectral function will be presented and analyzed. It will be shown that the coupling between the impurities always leads to a splitting of the Kondo resonance in the spectral function. A phase where both impurities are individually Kondo screened cannot be found. Using a 3d free electron gas as electronic host, the situation changes dramatically. The correlation effects decay quickly and for a sufficiently large inter-impurity distance, the system displays an individual Kondo screening of the two impurity spins.

In chapter 5 the single particle dynamics for quantum dot systems will be presented. First the $SU(N)$-symmetric SIAM will be studied to analyze the ability of fRG to describe the effects of an inter-dot interaction. The first quantum dot setup studied is a linear double

quantum dot. Depending on the strength of the hopping parameter, the system can be in three different phases. Spectral function for all three phases will be presented and analyzed. Additionally the effects of an external gate voltage and an inter-dot interaction are studied. The second quantum dot system is a linear triple quantum dot. Like the double quantum dot before, the properties of the system depend strongly on the hopping parameter. Up to now this system has only been analyzed by calculating static properties. Here, the spectral functions will be presented and analyzed. Finally a Y-shaped triple quantum dot will be studied. In addition to the dependence on the hopping parameter t an additional hopping between the outer dots will be introduced and the resulting frustration effects will be studied.

Chapter 6 will present a conclusion and an outlook.

Chapter 2

The Functional Renormalization Group

In this section a short derivation of the flow equations used to calculate the one-particle dynamics of various quantum impurity models is given. The method used here is based on a field theoretical approach that uses a generating functional for the partition functions of the investigated system. Using this generating functional, an infinite hierarchy of coupled differential equations is derived.

In the past various versions of such functional renormalization group (fRG) schemes have been discussed. In the Polchinski scheme [2] one uses amputated connected Green functions. In other schemes the amputated connected Green functions are expanded in terms of one-particle irreducible (1PI) vertex functions [3],[4],[5] or the generating functional is expanded by Wick ordered polynomials [6]. It should be noted that all these schemes are exact in all orders perturbation theory and thereby equivalent as long as treated exactly. But for practical use the infinite hierarchy of flow equations has to be truncated in some way. After that, the results do depend on the choice of the scheme.

In the following a set of flow equations for the 1PI vertex functions is derived by introducing a frequency cut-off into the free propagator. It follows the steps presented in [29]. More theoretical details on renormalization group methods in general can be found in [7].

2.1 The generating functional

The starting point of the derivation is the functional integral representation of the grand canonical partition function of the quantum mechanical system under consideration [17].

$$\frac{\mathcal{Z}}{\mathcal{Z}_0} = \frac{1}{\mathcal{Z}_0} \int \mathcal{D}\bar{\psi}\psi \exp\left\{ \left(\bar{\psi}, \left[\mathcal{G}^0\right]^{-1}\psi\right) - S_{\text{int}}\left(\{\bar{\psi}\}, \{\psi\}\right) \right\}, \tag{2.1}$$

where

$$S_{\text{int}}\left(\{\bar{\psi}\}, \{\psi\}\right) = \frac{1}{4} \sum_{k_1', k_2', k_1, k_2} \bar{v}_{k_1', k_2', k_1, k_2} \bar{\psi}_{k_1'} \bar{\psi}_{k_2'} \psi_{k_2} \psi_{k_1} \tag{2.2}$$

describes the two-particle interaction and $\mathcal{Z}_0$ corresponds to the non-interacting system. In this work only fermionic systems are of interest, so ψ and $\bar{\psi}$ are Grassman fields. The multi-indices $k_j^{(')}$ generally stand for a set of quantum numbers in a one-particle basis and a Matsubara frequency. In this work it will usually be a spin index, a Matsubara frequency and an impurity number in the case of multiple impurities. The short notation

$$\left(\bar{\psi}, \left[\mathcal{G}^0\right]^{-1}\psi\right) = \sum_{k, k'} \bar{\psi}_k \left[\mathcal{G}^0\right]_{k, k'}^{-1} \psi_{k'} \tag{2.3}$$

was used, where $\mathcal{G}^0$ is the propagator of the non-interacting system. The antisymmetrized two-particle interaction is described by $\bar{v}_{k1', k2'; k1, k2}$ including a factor $\delta_{\omega_1' + \omega_2', \omega_1 + \omega_2}$ to ensure energy conservation.

For the $m-$particle Green function the generating functional then is given by

$$\begin{aligned} \mathcal{W}\left(\{\bar{\eta}\}, \{\eta\}\right) &= \frac{1}{\mathcal{Z}_0} \int \mathcal{D}\bar{\psi}\psi \exp\left\{ \left(\bar{\psi}, \left[\mathcal{G}^0\right]^{-1}\psi\right) - S_{\text{int}}(\{\bar{\psi}\}, \{\psi\}) \right. \\ &\quad \left. - \left(\bar{\psi}, \eta\right) - \left(\bar{\eta}, \psi\right) \right\}. \end{aligned} \tag{2.4}$$

Taking the logarithm of $\mathcal{W}$, one obtains the generating functional for the connected $m-$particle Green functions $\mathcal{W}^c$, which can be calculated by derivation with respect to the external fields. Performing a Legendre transformation,

$$\Gamma\left(\{\bar{\phi}\}, \{\phi\}\right) = -\mathcal{W}^c\left(\{\bar{\eta}\}, \{\eta\}\right) - \left(\bar{\phi}, \eta\right) - \left(\bar{\eta}, \phi\right) + \left(\bar{\phi}, \left[\mathcal{G}^0\right]^{-1}\phi\right), \tag{2.5}$$

the generating functional of the 1PI vertex functions is obtained. They are calculated according to

$$\gamma_m \left(k_1', \ldots, k_m'; k_1, \ldots, k_m \right) \;=\; \frac{\delta^m}{\delta \bar{\phi}_{k_1'} \ldots \delta \bar{\phi}_{k_m'}} \frac{\delta^m}{\delta \phi_{k_m} \ldots \delta \phi_{k_1}} \Gamma \left(\{\bar{\phi}\}, \{\phi\} \right) \bigg|_{\phi=0=\bar{\phi}} . \qquad (2.6)$$

In contrast to the usual definition of Γ, the last term in eq.(2.5) has been added for convenience. The relation between the 1PI vertex function and the other Green functions can be found in various text books, e.g. [17].

The interacting part of the grand canonical potential can be calculated directly from the 0-particle vertex according to

$$\Omega = -T \ln \mathcal{Z} = T\gamma_0 - \Omega_0 , \qquad (2.7)$$

where Ω_0 is the grand canonical potential for the non-interacting case. The 1-particle Green function can be calculated from

$$G_1(k'; k) = G_1^c(k'; k) = \mathcal{G}_{k',k} = \left[\gamma_1 + \left[\mathcal{G}^0 \right]^{-1} \right]_{k',k}^{-1} \qquad (2.8)$$

with the self-energy $\Sigma = -\gamma_1$. The 2-particle vertex can be interpreted as an effective interaction.

2.2   A flow equation for Γ^Λ

The next step on the way to the flow equations is the introduction of a cut-off Λ into the non-interacting propagator. The new cut-off dependent propagator $\mathcal{G}^{0,\Lambda}$ will replace $\mathcal{G}^0$ in eq.(2.1) and eq.(2.4). $\mathcal{Z}^0$ will be replaced by $\mathcal{Z}^{0,\Lambda}$, which is calculated using $\mathcal{G}^{0,\Lambda}$ instead of $\mathcal{G}^0$. The cut-off has to satisfy the boundary conditions

$$\mathcal{G}^{0,\Lambda_0} = 0 \quad , \quad \mathcal{G}^{0,\Lambda=0} = \mathcal{G}^0 . \qquad (2.9)$$

This means, at the starting point of the flow Λ_0 all degrees of freedom are 'frozen out' and become turned on as Λ approaches 0. For $\Lambda = 0$ the original problem is recovered. In this work generally a sharp Matsubara frequency cut-off will be used. That means $\mathcal{G}^{0,\Lambda}$

is of the form

$$\mathcal{G}^{0,\Lambda} = \Theta\left(|\omega| - \Lambda\right)\mathcal{G}^0 \tag{2.10}$$

with $\Lambda_0 \to \infty$. By this replacement the quantities defined in eq.(2.1) to eq.(2.6) become dependent of Λ.

To finally derive flow equations for the generating functional one differentiates $\mathcal{W}^{c,\Lambda}$ with respect to Λ. Introducing

$$\mathcal{Q}^{\Lambda} = \frac{d}{d\Lambda}\left[\mathcal{G}^{0,\Lambda}\right]^{-1} , \tag{2.11}$$

this yields

$$\frac{d}{d\Lambda}\mathcal{W}^{c,\Lambda} = -\operatorname{Tr}\left(\mathcal{Q}^{\Lambda}\mathcal{G}^{0,\Lambda}\right) + \operatorname{Tr}\left(\mathcal{Q}^{\Lambda}\frac{\delta^2\mathcal{W}^{c,\Lambda}}{\delta\bar{\eta}\delta\eta}\right) - \left(\frac{\delta\mathcal{W}^{c,\Lambda}}{\delta\eta}, \mathcal{Q}^{\Lambda}\frac{\delta\mathcal{W}^{c,\Lambda}}{\delta\bar{\eta}}\right) . \tag{2.12}$$

Using eq.(2.12) and considering ϕ and $\bar{\phi}$ as the fundamental variables, eq.(2.5) leads to

$$\frac{d}{d\Lambda}\Gamma^{\Lambda}\left(\{\bar{\phi}\}, \{\phi\}\right) = -\frac{d}{d\Lambda}\mathcal{W}^{c,\Lambda}\left(\{\bar{\eta}^{\Lambda}\}, \{\eta^{\Lambda}\}\right) - \left(\bar{\phi}, \frac{d}{d\Lambda}\eta^{\Lambda}\right) - \left(\frac{d}{d\Lambda}\bar{\eta}^{\Lambda}, \phi\right) + (\bar{\phi}, \mathcal{Q}^{\Lambda}\phi) \tag{2.13}$$

With the help of the chain rule this can be transformed to

$$\frac{d}{d\Lambda}\Gamma^{\Lambda} = \operatorname{Tr}\left(\mathcal{Q}^{\Lambda}\mathcal{G}^{0,\Lambda}\right) - \operatorname{Tr}\left(\mathcal{Q}^{\Lambda}\frac{\delta^2\mathcal{W}^{c,\Lambda}}{\delta\bar{\eta}^{\Lambda}\delta\eta^{\Lambda}}\right) . \tag{2.14}$$

Note, that the term introduced in eq.(2.5) now exactly cancels, which justifies its earlier addition. To continue, the relation between the second functional derivatives of Γ and $\mathcal{W}^c$ is used [17]. The result is the following functional differential equation for Γ^{Λ}:

$$\frac{d}{d\Lambda}\Gamma^{\Lambda} = \operatorname{Tr}\left(\mathcal{Q}^{\Lambda}\mathcal{G}^{0,\Lambda}\right) - \operatorname{Tr}\left(\mathcal{Q}^{\Lambda}\mathcal{V}^{1,1}_{\bar{\phi},\phi}(\Gamma^{\Lambda}, \mathcal{G}^{0,\Lambda})\right) . \tag{2.15}$$

Here the matrix

$$\mathcal{V}_{\bar{\phi},\phi}(\Gamma^{\Lambda}, \mathcal{G}^{\Lambda}) = \begin{pmatrix} \frac{\delta^2\Gamma^{\Lambda}}{\delta\bar{\phi}\delta\phi} + \left[\mathcal{G}^{0,\Lambda}\right]^{-1} & \frac{\delta^2\Gamma^{\Lambda}}{\delta\phi\delta\phi} \\ \frac{\delta^2\Gamma^{\Lambda}}{\delta\bar{\phi}\delta\bar{\phi}} & \frac{\delta^2\Gamma^{\Lambda}}{\delta\phi\delta\bar{\phi}} - \left[\left[\mathcal{G}^{0,\Lambda}\right]^{-1}\right]^t \end{pmatrix}^{-1} \tag{2.16}$$

has been defined, where $\mathcal{V}^{1,1}_{\phi,\bar{\phi}}$ denotes the upper left block $\mathcal{V}_{\phi,\bar{\phi}}$ and t implies the use of the transposed matrix. To include self-energy corrections in the flow equations, $\mathcal{V}_{\phi,\bar{\phi}}$ is expressed in terms of $\mathcal{G}^{\Lambda}$ instead of $\mathcal{G}^{0,\Lambda}$. This can be done by defining

$$\mathcal{U}_{\bar{\phi},\phi} = \frac{\delta^2 \Gamma^{\Lambda}}{\delta \bar{\phi} \delta \phi} - \gamma_1^{\Lambda} . \tag{2.17}$$

Using

$$\mathcal{G}^{\Lambda} = \left[\left[\mathcal{G}^{0,\Lambda} \right]^{-1} + \gamma_1^{\Lambda} \right]^{-1} , \tag{2.18}$$

one can write the differential equation for Γ^{Λ} as

$$\frac{d}{d\Lambda} \Gamma^{\Lambda} = \text{Tr} \left(\mathcal{Q}^{\Lambda} \mathcal{G}^{0,\Lambda} \right) - \text{Tr} \left(\mathcal{G}^{\Lambda} \mathcal{Q}^{\Lambda} \tilde{\mathcal{V}}^{1,1}_{\bar{\phi},\phi} (\Gamma^{\Lambda}, \mathcal{G}^{\Lambda}) \right) \tag{2.19}$$

with

$$\tilde{\mathcal{V}}_{\bar{\phi},\phi} \left(\Gamma^{\Lambda}, \mathcal{G}^{\Lambda} \right) = \left[\mathbf{1} - \begin{pmatrix} -\mathcal{G}^{\Lambda} & 0 \\ 0 & \left[\mathcal{G}^{\Lambda} \right]^t \end{pmatrix} \begin{pmatrix} \mathcal{U}_{\bar{\phi},\phi} & \frac{\delta^2 \Gamma^{\Lambda}}{\delta \phi \delta \phi} \\ \frac{\delta^2 \Gamma^{\Lambda}}{\delta \bar{\phi} \delta \bar{\phi}} & -\mathcal{U}^t_{\bar{\phi},\phi} \end{pmatrix} \right]^{-1} . \tag{2.20}$$

The easiest way to determine the correct initial condition for Γ^{Λ} is to turn to the perturbative expansion for the γ_m. For $\Lambda = \Lambda_0$ the free propagator vanishes: $\mathcal{G}^{0,\Lambda_0} = 0$. This means that all perturbative expressions except for the bare interaction are equal to 0. Consequently only the two-particle vertex has a non vanishing initial condition and one finds

$$\Gamma^{\Lambda_0} \left(\{ \bar{\phi} \}, \{ \phi \} \right) = S_{\text{int}} \left(\{ \bar{\phi} \}, \{ \phi \} \right) . \tag{2.21}$$

A lengthy algebraic calculation gives the same result.

2.3 Expansion of Γ^Λ

Since the goal is a set of flow equations for the γ_m^Λ, Γ^Λ is expanded in the external sources. This gives:

$$\Gamma^\Lambda\left(\{\bar\phi\},\{\phi\}\right) = \sum_{m=0}^\infty \frac{(-1)^m}{(m!)^2} \sum_{k'_1,\ldots,k'_m} \sum_{k_1,\ldots,k_m} \gamma_m^\Lambda\left(k'_1,\ldots,k'_m;k_1,\ldots,k_m\right)$$

$$\times \bar\phi_{k'_1}\ldots\bar\phi_{k'_m}\phi_{k_m}\ldots\phi_{k_1} \qquad (2.22)$$

and eq.(2.20) is expanded using a geometric series. $\mathcal{U}_{\phi,\bar\phi}$ as well as the second functional derivatives of Γ^Λ are at least quadratic in the external sources. Comparing powers of fields on both sides, one finally deduces the flow equations for the γ_m^Λ. For γ^{Λ_0} the equation reads

$$\frac{d}{d\Lambda}\gamma_0^\Lambda = \mathrm{Tr}\left(\mathcal{Q}^\Lambda\mathcal{G}^{0,\Lambda}\right) - \mathrm{Tr}\left(\mathcal{Q}^\Lambda\mathcal{G}^\Lambda\right). \qquad (2.23)$$

γ_0 is coupled to the self-energy via $\mathcal{G}$. The flow of the self-energy itself is determined by

$$\frac{d}{d\Lambda}\gamma_1^\Lambda(k';k) = -\frac{d}{d\Lambda}\Sigma_{k',k}^\Lambda = \mathrm{Tr}\left(\mathcal{S}^\Lambda\gamma_2^\Lambda(k',\ldots;k,\ldots)\right) \qquad (2.24)$$

with

$$\mathcal{S}^\Lambda = \mathcal{G}^\Lambda\mathcal{Q}^\Lambda\mathcal{G}^\Lambda \qquad (2.25)$$

being the so-called single-scale propagator. Apart from the self-energy, γ_2 enters the flow equation for Σ. The flow equation for γ_2^Λ is

$$\begin{aligned}
\frac{d}{d\Lambda}\gamma_2^\Lambda(k'_1,k'_2;k_1,k_2) &= \mathrm{Tr}\left(\mathcal{S}^\Lambda\gamma_3^\Lambda(k'_1,k'_2,\ldots;k_1,k_2,\ldots)\right)\\
&\quad - \mathrm{Tr}\left(\mathcal{S}^\Lambda\gamma_2^\Lambda(\ldots,\ldots;k_1,k_2)\left[\mathcal{G}^\Lambda\right]^t\gamma_2^\Lambda(k'_1,k'_2;\ldots,\ldots)\right)\\
&\quad - \mathrm{Tr}\left(\mathcal{S}^\Lambda\gamma_2^\Lambda(k'_1,\ldots;k_1,\ldots)\mathcal{G}^\Lambda\gamma_2^\Lambda(k'_2,\ldots;k_2,\ldots)\right.\\
&\quad \left. - [k'_1 \leftrightarrow k'_2] - [k_1 \leftrightarrow k_2] + [k'_1 \leftrightarrow k'_2, k_1 \leftrightarrow k_2]\right). \qquad (2.26)
\end{aligned}$$

A flow equation for γ_3^Λ, that would be necessary to exactly calculate γ_2^Λ, is not presented here. Generally γ_{m+1}^Λ enters the flow equation for γ_m^Λ. Only by truncating this hierarchy

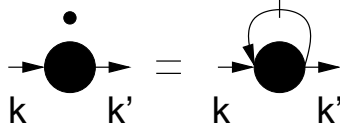Figure 2.1: Diagrammatic form of the flow equation for $\gamma_1^\Lambda = -\Sigma^\Lambda$. The slashed line stands for the single scale propagator $\mathcal{S}^\Lambda$.

a finite set of flow equations can be obtained. In this work the hierarchy is truncated by setting $\gamma_3^\Lambda = \gamma_3^{\Lambda_0} = 0$. This leaves two coupled differential equations for Σ and γ_2, which can be integrated from $\Lambda = \Lambda_0$ to $\Lambda = 0$, giving an approximate result for Σ^Λ and γ_2^Λ. A diagrammatic representation of the flow equation for Σ^Λ is shown in fig.(2.1) and of the flow equation for γ_2^Λ in fig.(2.2).

Looking at the systematics of the flow equations hierarchy this truncation scheme emerges quite naturally. For $m_c \geq 2$, $\gamma_{m_c+1}^\Lambda$ always enters the rhs of the flow equation for $\gamma_{m_c}^\Lambda$. By setting $\gamma_{m_c+1}^\Lambda$ to its initial value, which is 0 for $m_c \geq 2$ if only two-particle interactions are present in the Hamiltonian, a closed set of equations for γ_m^Λ, $m \leq m_c$, follows. Solving this closed system of equations, an approximate solution for the original problem is produced. Comparing this approximate result to conventional perturbation theory by expanding the vertex functions in terms of the bare interaction strength, it can be shown that the approximate solution is at least correct up to order m_c in the bare interaction. Depending on the application one has in mind, it can be sensible to make further approximations to the flow equations. In some cases this might even be necessary to obtain a set of equations, that is numerically manageable. In some cases such approximations allow an analytical treatment of the flow. This has been done in the past very successfully when
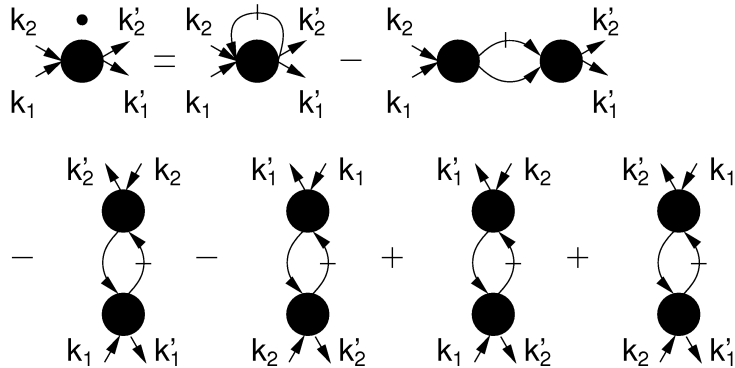

Figure 2.2: Diagrammatic form of the flow equation for γ_2^Λ. The slashed line stands for the single scale propagator $\mathcal{S}^\Lambda$, the unslashed line for $\mathcal{G}^\Lambda$.

17

treating one- and two-dimensional quantum many-body systems.

In this work only truncation of order $m_c = 2$ without any further approximations will be considered, unless explicitly stated differently. This is possible since only locally interacting (zero-dimensional) many-particle systems will be treated.

A modification to the flow equations that will be included in this work was suggested in [18]. Since only $m_c = 2$ is considered here, only the necessary changes up to this order will be stated here. Motivated by the fulfillment of a certain Ward identity, the single scale propagator $\mathcal{S}^\Lambda$ in the flow equation for γ_2 is replaced by $-d\mathcal{G}^\Lambda/d\Lambda$. Since

$$\frac{d\mathcal{G}^\Lambda}{d\Lambda} = -\mathcal{S}^\Lambda + \mathcal{G}^\Lambda \frac{d\Sigma^\Lambda}{d\Lambda}\mathcal{G}^\Lambda \; , \tag{2.27}$$

the contributions of the modification are obviously at least of third order in the bare interaction strength. In fRG treatment of order $m_c = 2$ of some models this modification leads to exact results for γ_1 and γ_2. Therefore an improvement of results for the models, treated here is possibly to be expected. It will be shown that this is indeed true.

2.4   Observables

The most convenient way to calculate observables from fRG is to calculate them indirectly using the resulting vertex functions like the self-energy or the spectral function obtained by analytic continuation if possible. For some observables however, it is possible to directly derive a flow equation so that they can be determined directly from the RG flow. If one would solve the complete hierarchy of flow equations to obtain the exact solution of the problem under consideration, the results from both approaches would be identical. Since this is not possible and since the flow equations are only solved in a truncated scheme, calculating observables from vertex functions or directly from the flow only gives approximate results. In some cases the direct calculation can produce more accurate results. In this work, flow equations for the ground state energy and for the density profile will be presented. The ground state energy could be computed from the full propagator on the real axis [32]. To obtain this propagator, an analytic continuation from imaginary to real frequencies is necessary. Since this process itself is a serious numerical problem, it is preferable to obtain the ground state energy directly from the RG flow. In the case of the local density it is possible to calculate this quantity directly from the one-particle Green

function on the imaginary axis. In [14] it was shown that applying fRG with a truncation scheme, that leads to a frequency independent self-energy, on a Luttinger liquid system, it is necessary to calculate the density from a separate flow equation to obtain convincing results. Whether this is also true for the frequency dependent version used here will be investigated in chapter 3.

The ground state energy can be calculated from the 0-particle vertex γ_0, for which a flow equation has already been presented (eq.(2.23)) [28]. $T\gamma_0$ is the interaction caused contribution to the grand canonical potential (eq.(2.7)). For $\mu = 0$ and at $T = 0$ the ground state energy is given by Ω. With these preliminaries the ground state energy E_0 is given by

$$E_0 = E_0^0 + \lim_{T \to 0} T\gamma_0, \tag{2.28}$$

where E_0^0 is the ground state energy in the non-interacting case. Using eq.(2.23) and the cut-off dependent propagator defined in eq.(2.10) and after expanding the product $\mathcal{Q}^\Lambda \mathcal{G}^\Lambda$ in terms of $\mathcal{G}_0^\Lambda \Sigma^\Lambda$ and summing up again, the result reads

$$\frac{d}{d\Lambda} \lim_{T \to 0} T\gamma_0^\Lambda = \frac{d}{d\Lambda} e_0^\Lambda = -\frac{1}{2\pi} \mathrm{Tr} \ln \left[1 - \mathcal{G}^0 \, \Sigma^\Lambda \right] \; . \tag{2.29}$$

To derive a flow equation for the density n_k the method presented in [14] is used. A term $\phi_k n_k$ with a small field ϕ_k is added to the Hamiltonian. The local density can then be calculated by simple derivation:

$$n_k = \left. \frac{\partial \Omega(\phi_k)}{\partial \phi_k} \right|_{\phi_k = 0} \; . \tag{2.30}$$

The additional term is considered to belonging to the interacting part of the Hamiltonian. It results in a frequency independent contribution to the self-energy. A flow equation for the grand canonical potential (with an additional factor T) is already given by eq.(2.29). To obtain a flow equation for the density, the derivative of eq.(2.30) can be performed directly in the flow equation. This results in

$$\frac{\partial}{\partial \Lambda} n_k^\Lambda = -\frac{1}{2\pi} \mathrm{Tr} \mathcal{G}^\Lambda R_k^\Lambda, \tag{2.31}$$

where the density response vertex

$$R_k^\Lambda = \left. \frac{\partial \Sigma^\Lambda}{\partial \phi_k} \right|_{\phi_k=0} \tag{2.32}$$

has been defined. The propagators $\mathcal{G}^\Lambda$ have to be determined in the absence of ϕ_k. A flow equation for R_k^Λ can be derived from eq.(2.24):

$$\frac{\partial}{\partial \Lambda} R_{k;j',j}^\Lambda = \ \text{Tr}\left(\mathcal{G}^\Lambda R_k^\Lambda \mathcal{G}^\Lambda \gamma_2^\Lambda(j',\ldots;j,\ldots) \right) \ . \tag{2.33}$$

2.5 Padé Approximation

Although $k_i^{(\prime)}$ is a multi-index representing an arbitrary set of quantum numbers and a Matsubara frequency, it was mentioned that in this work it will usually consist of a Matsubara frequency $i\omega$, a spin index σ and, in the case of more than one impurity, an impurity index m. Consequently all results of the fRG calculations will be vertex functions given at imaginary frequencies, like $\Sigma(i\omega)$. To determine a spectral function for a given problem, it will be necessary to perform an analytic continuation to the real axis. Since it will usually not be possible to solve the flow equations analytically, only numerical data of the vertex functions will be available. The analytic continuation from numerical data is known to be an ill posed problem. To be able to present spectral functions despite of this problem, a technique called Padé approximation will be employed. It is based on the idea to approximate a rational function to the given data and perform the analytic continuation on this function. In contrast to fitting a polynomial and doing the continuation, this method is capable of capturing features like poles in the complex plane and the approximant does not necessarily grow to infinity for large arguments. It will be shown that Padé approximation gives very good results although one has to be careful, since it is very difficult to control the error made. The best way to ensure the reliability of the results is to perform repeated calculations with different frequency meshes on the imaginary axis. In this work the scheme from [30] is used. More detailed information on this topic is presented in appendix A.

Chapter 3

The Single Impurity Anderson Model

The first application of the fRG will be the Single Impurity Anderson Model (SIAM). This model has been investigated very closely and its equilibrium properties are understood very well. For a good overview see e.g. [22]. With Wilson's NRG a method is at hand that can be used to calculate the single-particle properties of the SIAM very accurately [23]. These results will be compared to those obtained from fRG . Therefore this model can serve as a benchmark to get an idea of how successfully fRG can be used to calculate dynamics of Anderson impurity models. In the previous chapter it was pointed out that the fRG result is correct at least up to order m_c in the interaction strength. For this reason the fRG results will also be compared to second-order perturbation theory in the interaction strength (2PTh). Some results presented in this chapter, especially those for the particle-hole symmetric case, have been published in [29].

3.1   The Model

The Single Impurity Anderson Model, originally suggested by P.W. Anderson in 1961 [19], is a generic model to describe a single strongly localized energy level being coupled to an electronic bath. Experimentally the localized energy level can be the d- or f-orbital of a transition metal atom or some kind of quantum dot structure allowing for two electrons

to occupy it (one with spin up and one with spin down). The electronic host can be any kind of conduction band.

The Anderson Hamiltonian consists of three parts. First, there is the conduction electron part describing an electron band with an energy dispersion ϵ_k. The second term represents the impurity level, which has an energy ϵ_d relative to the chemical potential μ of the conduction band electrons ($\mu = 0$). If the impurity level is doubly occupied, the electrons are subject to a Coulomb repulsion $U > 0$. The last part is the coupling between the band and the impurity. The band electrons hybridize with the impurity level with an amplitude V. It is assumed here that the hybridization amplitude is independent of k. Collecting all these parts, in second quantization the Hamiltonian looks like this:

$$H = \sum_{\vec{k}\sigma} \epsilon_{\vec{k}} c_{\vec{k}\sigma}^\dagger c_{\vec{k}\sigma} + \epsilon_d \sum_\sigma d_\sigma^\dagger d_\sigma + U d_\uparrow^\dagger d_\uparrow d_\downarrow^\dagger d_\downarrow + \sum_{\vec{k}\sigma} V_k \left(c_{\vec{k}\sigma}^\dagger d_\sigma + \text{h.c.} \right). \qquad (3.1)$$

As one can clearly see, the interaction takes place only locally on the impurity site, which makes the model a zero-dimensional interacting system. Later this model will be extended to more than one impurity site.

As simple as it looks, this model is a quite complicated many-body problem, which displays a rich variety of physical behaviour, depending on the interplay of the four bare energy scales, namely the Coulomb repulsion U, the position of the impurity level ϵ_d, the conduction electron bandwidth W and $\Delta_0 = \pi V^2 \rho_c(0)$, which is the width of the bare level generated by the hybridization. $\rho_c(\epsilon)$ is the density of states of the conduction band electrons, which is assumed to be slowly varying around $\omega = 0$.

In this chapter the electronic host is a flat electron band of infinite bandwidth and the hybridization will be assumed to have no k-dependence ($V_k = V$). The so-called hybridization function is then given by

$$\Delta(z) := V^2 \int d\epsilon \rho_c(\epsilon)/(z - \epsilon) = -i \, \Delta_0 \text{sign}(\text{Im}(z)). \qquad (3.2)$$

The non-interacting Green function for this problem is given by

$$\mathcal{G}_d^0(z) = \frac{1}{i\omega - \epsilon_d + i \, \text{sign}(\text{Im}(z))\Delta_0} \,. \qquad (3.3)$$

The dynamics for $U \neq 0$ are determined by first calculating the self-energy $\Sigma(z)$. The impurity Green function is then given by

$$\mathcal{G}_d(z) = \frac{1}{[\mathcal{G}_d^0(z)]^{-1} - \Sigma(z)} \quad . \tag{3.4}$$

The impurity spectral function can be calculated directly from the Green function:

$$\rho_d^0(\omega) = -\frac{1}{\pi} \mathrm{Im}\ \mathcal{G}_d(\omega + i0). \tag{3.5}$$

In the noninteracting case ($U = 0$), the spectral function is a Lorentzian centered around ϵ_d:

$$\rho_d^0(\omega) = \frac{1}{\pi} \frac{\Delta_0}{(\omega - \epsilon_d)^2 + \Delta_0^2}. \tag{3.6}$$

The one-particle dynamics consist of a single resonance at ϵ_d. For $V = 0$ the resonance would be a $\delta-$peak. Due to the hybridization, an added electron ($\epsilon_d > 0$) or a hole ($\epsilon_d < 0$) can only remain on the localized level for a finite time. This leads to a broadening of the resonance to a width of Δ_0. In the weak coupling regime $U/\Delta_0 \ll 1$ this behaviour does not change very much. For larger U the one-particle dynamics change considerably. Due to the Coulomb repulsion, there is now one resonance at $\omega = \epsilon_d$ and one resonance at $\omega = \epsilon_d + U$. The width of these atomic peaks is $2\Delta_0$. These two resonances are caused by charge excitations. Additionally a new resonance has formed near the chemical potential ($\omega = 0$), the Kondo or Abrikosov-Suhl resonance. For the particle-hole symmetric case ($\epsilon_d = -U/2$) spectral functions for the non-interacting and the interacting case are shown
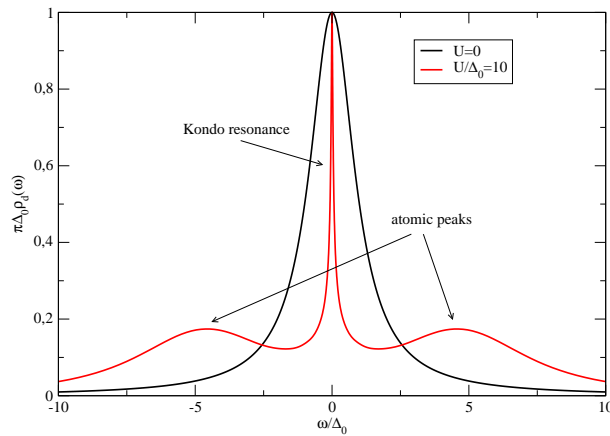

Figure 3.1: Spectral functions for the symmetric SIAM.

23

in fig.(3.1). For $U, -\epsilon_d \gg \Delta_0$ charge fluctuation from the average value 1 are negligible. In this parameter regime the Anderson model can be mapped to a Kondo model using a Schrieffer-Wolff transformation [20],[21]. The Kondo model describes a local moment instead of an energy level being coupled to an electronic host. In contrast to the Anderson model it cannot include charge fluctuations on the impurity site. The above conditions for U and ϵ_d assure that the impurity level in the Anderson model is occupied by one electron and that charge fluctuations are irrelevant for the physics of the system. Consequently, in this limit the Anderson model displays Kondo physics. The spin of the singly occupied impurity level is coupled antiferromagnetically to the conduction electrons. This results in a screening of the local spin with a characteristic energy scale $\ln(T_K) \propto -1/\Delta_0$, with T_K being the so-called Kondo temperature. This exponentially small energy scale is a severe problem for any computational method.

For $\omega \ll T_K$ the system locally behaves like a Fermi liquid [33],[34]. In this region the system can be described by a non-interacting Anderson Hamiltonian with renormalized parameters that are $U \to U^* = 0$, $\epsilon_d \to \epsilon_d^* = 0$ and $\Delta_0 \to \Delta_0^* \propto T_K$ [22]. Therefore the low-energy dynamics can universally be described by the Kondo temperature T_K.
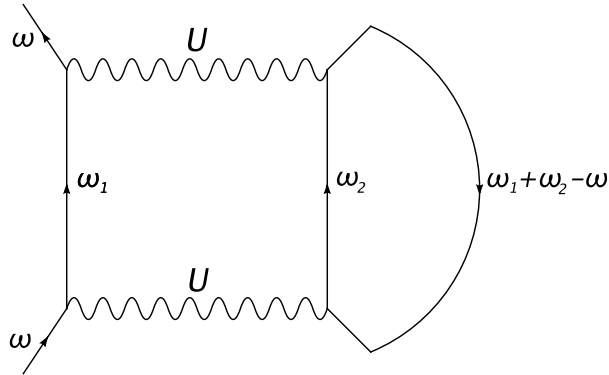
3.2   Second Order Perturbation Theory

Figure 3.2: Diagrammatic contribution to the self-energy in second order in U.

Maybe the simplest way to calculate the self-energy is to use perturbation theory. In the case of the SIAM generally two perturbative expansions are possible and have been carried out in the past. One possibility is perturbation theory in the hybridization, i.e. around the atomic limit. This perturbation theory in Δ_0/U naturally works very well for large U,

i.e. when Δ_0/U is small [22], [24]. The other method, that is used here, is perturbation theory in U, i.e. the perturbative expansion is made around the non-interacting case. The lowest order, in which non-trivial behaviour of dynamical properties can be found, is U^2. The calculations in this order are particularly easy when using the Hartree-Fock propagator $\mathcal{G}^{HF}$ instead of the free propagator. Only one diagram has to be taken into account in this case. It is shown in fig.(3.2). The self-energy in second order perturbation theory is then calculated to be

$$\Sigma^{2PTh}(i\omega) = -\frac{U^2}{4\pi^2} \int \, d\omega_1 \, d\omega_2 \ \mathcal{G}^{HF}(i\omega_1)\mathcal{G}^{HF}(i\omega_2)\mathcal{G}^{HF}(i\omega_1 + i\omega_2 - i\omega) \ .$$

Using a spectral representation of the free propagator and a contour integral technique, the analytic continuation of this expression can be obtained. This allows for the calculation of spectral functions without the help of Padé approximation. In the particle-hole symmetric case $(2\epsilon_d + U = 0)$ this approach works particularly well. It already captures the qualitative features of the spectral function for fairly large U/Δ_0. The spectral function includes the two atomic peaks. By comparison to a local moment approach, it has been shown that 2PTh gives accurate results here [26]. The Kondo resonance at the chemical potential is described qualitatively correct as well. Using 2PTh the width of this resonance shows an algebraic behaviour with growing U. In the strong coupling regime the quantitative description of the Kondo resonance is therefore rather poor. 2PTh is not capable of describing the exponential behaviour in this regime. In the non-symmetric case second order perturbation theory cannot produce convincing results. Already for rather small U/Δ_0 the discrepancy between results from 2PTh and the ones from Wilson's NRG becomes apparent. 2PTh cannot reproduce the suppression of the effective level shift by the interaction sufficiently. The impact of a shift of the impurity level away from the symmetric value is therefore overestimated. The reason why 2PTh works so extraordinarily well in the symmetric case can be traced to two causes. First, perturbation theory correctly describes the atomic limit as well as the non-interacting case. For finite U the result can be seen as an interpolation between these two cases. Since the exact result continuously changes from one case to the other, it is not surprising that an interpolation captures the main features of the exact result. Second, one can easily see that in the symmetric case, only diagrams of even order contribute to the self-energy. In particular there are no diagrams of third order. Additionally it was shown by Yamada that the contribution in fourth order stay small for rather large U [35]. This is the reason why 2PTh

gives surprisingly good results for rather large U/Δ_0 in the symmetric case. The results from 2PTh can also be obtained from the fRG flow equations. This will be discussed later.

3.3   The Numerical Renormalization Group

The Numerical Renormalization Group (NRG) developed by Wilson in 1975 is capable of accurately describing the properties of the SIAM for arbitrary interaction strength [1], [23]. With this method it is especially possible to correctly calculate the Kondo resonance. The key to solving this problem is to treat all energy scales alike and in a non-perturbative way.

The main idea in the NRG calculation is to perform an iterative diagonalization of the Hamiltonian. The energy states of the conduction band are discretized using a logarithmic discretization. In each step of the NRG procedure the Hamiltonian is diagonalized on a certain energy interval. The energy levels of the diagonalized Hamiltonian are rescaled and truncated. Only a certain number of the most relevant energy levels is kept in every step. In this way the whole energy axis is included in the calculation step after step. If one could keep all energy levels and if no truncation were necessary, the calculation would give the exact result. Especially the low-energy physics can be described with high accuracy using this method. In the the high-energy region broadening effects occur. Although NRG is a very useful tool in the treatment of the Single Impurity Anderson Model, it has a major drawback when turning to models with more degrees of freedom. The numerical effort rises exponentially. Therefore more than two impurities are generally not treatable. In two impurity systems the results for dynamical properties at small and intermediate interaction strengths are not as convincing as in the single impurity case as well.

3.4   The Flow equations

To derive flow equations for the self-energy Σ^Λ and the two-particle vertex γ_2^Λ, the starting point are eq.(2.24) and eq.(2.26). Since $m_c = 2, \gamma_3^\Lambda = \gamma_3^{\Lambda_0} = 0$ are used here, no flow equations for higher order vertex functions are required. In this chapter the ground state energy will not be calculated, so no equation for γ_0 is needed as well. The cut-off will be

a sharp frequency cut-off:

$$G_\sigma^{(0),\Lambda}(i\omega)\Theta(|\omega| - \Lambda)G_\sigma^\Lambda(i\omega) \; .$$

Since in this chapter only one impurity is considered, the multi-index k is replaced by a spin index σ and a Matsubara frequency $i\omega$. With this the two particle vertex can be written in the form

$$
\begin{aligned}
\bar{\gamma}_2^\Lambda(\xi_1', \xi_2'; \xi_1, \xi_2) \;=\; & \delta(\omega_1 + \omega_2 - \omega_1' - \omega_2')\Big\{ \, \delta_{\sigma_1,\sigma_1'}\delta_{\sigma_2,\sigma_2'} \, \gamma_{2,freq}^\Lambda(i\omega_1', i\omega_2'; i\omega_1, i\omega_2) \\
& -\delta_{\sigma_1,\sigma_2'}\delta_{\sigma_2,\sigma_1'} \, \gamma_{2,freq}^\Lambda(i\omega_2', i\omega_1'; i\omega_1, i\omega_2) \\
& -\delta_{\sigma_2,\sigma_1'}\delta_{\sigma_1,\sigma_2'} \, \gamma_{2,freq}^\Lambda(i\omega_1', i\omega_2'; i\omega_2, i\omega_1) \\
& +\delta_{\sigma_2,\sigma_2'}\delta_{\sigma_1,\sigma_1'} \, \gamma_{2,freq}^\Lambda(i\omega_2', i\omega_1'; i\omega_2, i\omega_1)\Big\} \\
\;=\; & \delta(\omega_1 + \omega_2 - \omega_1' - \omega_2')\Big\{ \, \delta_{\sigma_1,\sigma_1'}\delta_{\sigma_2,\sigma_2'} \, \mathcal{U}^\Lambda(i\omega_1', i\omega_2'; i\omega_1, i\omega_2) \qquad (3.7) \\
& -\delta_{\sigma_1,\sigma_2'}\delta_{\sigma_2,\sigma_1'} \, \mathcal{U}^\Lambda(i\omega_2', i\omega_1'; i\omega_1, i\omega_2)\Big\},
\end{aligned}
$$

with

$$\mathcal{U}^\Lambda(i\omega_1', i\omega_2'; i\omega_1, i\omega_2) = \gamma_{2,freq}^\Lambda(i\omega_1', i\omega_2'; i\omega_1, i\omega_2) + \gamma_{2,freq}^\Lambda(i\omega_2', i\omega_1'; i\omega_2, i\omega_1) \; . \qquad (3.8)$$

Note, that other parametrizations of the two-particle vertex are possible, as long as the vertex-function is totally antisymmetric. Later a parametrization distinguishing different spin channels will be used to calculate the static spin susceptibility. These different parametrizations give identical results for the self-energy. When aiming only at $\Sigma(i\omega)$, the parametrization with only one frequency dependent function is the most convenient one. After parametrizing the two-particle vertex, the sum over the spins in eq.(2.24) can be performed, giving for the self energy

$$
\frac{d}{d\Lambda}\Sigma_\sigma^\Lambda(i\omega) = -\frac{1}{2\pi}\sum_{\alpha=\pm 1}\frac{1}{G_\sigma^{(0)}(i\alpha\Lambda)^{-1} - \Sigma_\sigma^\Lambda(i\alpha\Lambda)}\Big[2\,\mathcal{U}^\Lambda(i\omega, i\alpha\Lambda; i\omega, i\alpha\Lambda)- \qquad (3.9)
$$
$$
\mathcal{U}^\Lambda(i\alpha\Lambda, i\omega; i\omega, i\alpha\Lambda)\Big].
$$

Now a flow-equation for $\mathcal{U}^\Lambda(i\omega_1', \omega_2'; \omega_1, \omega_2)$, $\omega_1' + \omega_2' = \omega_1 + \omega_2$ is needed. This is accomplished by performing the spin sum in eq.(2.26) and setting the external spins to $\sigma_1' = \sigma_1 \neq \sigma_2' = \sigma_2$. The result is

$$\frac{d}{d\Lambda}\mathcal{U}^\Lambda(i\omega_1', i\omega_2'; i\omega_1, i\omega_2) = -\frac{1}{2\pi}\int_{-\infty}^{\infty} d\omega \left[\mathcal{P}^\Lambda(i\omega, i\omega_1 + i\omega_2 - i\omega)\right. \tag{3.10}$$

$$\left(-\mathcal{U}^\Lambda(i\omega, i\omega_1 + i\omega_2 - i\omega; i\omega_1, i\omega_2)\mathcal{U}^\Lambda(i\omega_2', i\omega_1'; i\omega_1 + i\omega_2 - i\omega, i\omega)\right.$$

$$\left.-\mathcal{U}^\Lambda(i\omega_1 + i\omega_2 - i\omega, i\omega; i\omega_1, i\omega_2)\mathcal{U}^\Lambda(i\omega_1', i\omega_2'; i\omega_1 + i\omega_2 - i\omega, i\omega)\right)$$

$$+\left\{\mathcal{P}^\Lambda(i\omega, -i\omega_1 + i\omega_1' + i\omega)\right.$$

$$\left(2\mathcal{U}^\Lambda(i\omega_1', i\omega; i\omega_1, -i\omega_1 + i\omega_1' + i\omega)\mathcal{U}^\Lambda(i\omega_2', -i\omega_1 + i\omega_1' + i\omega; i\omega_2, i\omega)\right.$$

$$-\mathcal{U}^\Lambda(i\omega_1', i\omega; i\omega_1, -i\omega_1 + i\omega_1' + i\omega)\mathcal{U}^\Lambda(-i\omega_1 + i\omega_1' + i\omega, i\omega_2'; i\omega_2, i\omega)$$

$$\left.-\mathcal{U}^\Lambda(i\omega, i\omega_1'; i\omega_1, -i\omega_1 + i\omega_1' + i\omega)\mathcal{U}^\Lambda(i\omega_2', -i\omega_1 + i\omega_1' + i\omega; i\omega_2, i\omega)\right)$$

$$\left.+(1' \leftrightarrow 2'; 1 \leftrightarrow 2)\right\}$$

$$-\left\{\mathcal{P}^\Lambda(i\omega, -i\omega_1 + i\omega_2' + i\omega)\right.$$

$$\mathcal{U}^\Lambda(i\omega, i\omega_2'; i\omega_1, -i\omega_1 + i\omega_2' + i\omega)\mathcal{U}^\Lambda(-i\omega_1 + i\omega_2' + i\omega, i\omega_1'; i\omega_2, i\omega)$$

$$\left.\left.+(1' \leftrightarrow 2'; 1 \leftrightarrow 2)\right\}\right] .$$

$\mathcal{P}$ can either be $\mathcal{P}_{con}$ for the conventional version of the fRG or $\mathcal{P}_{mod}$ for the modified version (mfRG) proposed by Katanin and introduced in chapter 2. The initial conditions for Σ^Λ and U^Λ are given by $\Sigma^{\Lambda=\infty} = 0$, $\mathcal{U}^{\Lambda=\infty} = U$. Numerically, the integration of the flow equations can only start at a $\Lambda_0 \gg \max(U, \Delta_0)$. The flow from $\Lambda = \infty$ to Λ_0 gives a contribution of $U/2$ to Σ^Λ, which leads to new initial conditions:

$$\Sigma_\sigma^{\Lambda_0} = \frac{U}{2} \; ; \quad \gamma_{2,\omega}^{\Lambda_0} = U \; . \tag{3.11}$$

What is left now, is the calculation of $\mathcal{S}^\Lambda(i\omega) = \mathcal{G}^\Lambda(i\omega)\mathcal{Q}^\Lambda(i\omega)\mathcal{G}^\Lambda(i\omega)$ for eq.(3.9) and the combined propagator $\mathcal{P}^\Lambda_{con}(i\omega, i\omega') = \mathcal{S}^\Lambda(i\omega)\mathcal{G}^\Lambda(i\omega')$ and $\mathcal{P}^\Lambda_{mod} = -d\mathcal{G}^\Lambda/d\Lambda\ \mathcal{G}^\Lambda$ for eq.(3.10). In any case, combinations of distributions $\delta(\Lambda - \omega)$ and $\Theta(\Lambda - \omega)$ appear. It is not immediately clear how these expressions should be treated. Introducing a broadening ϵ into the step function Θ_ϵ and using $\delta_\epsilon = d\Theta_\epsilon/d\epsilon$, it can be shown that for $\epsilon \to 0$ these expressions are well defined and can be calculated to be

$$\delta(a)f(\Theta(a)) \to \delta(a) \int_0^1 f(x)dx . \tag{3.12}$$

Using this result for the combined propagators, they are given by

$$S_\sigma^\Lambda(i\omega) = \frac{1}{\left[1 - G_\sigma^{(0),\Lambda}(i\omega)\Sigma_\sigma^\Lambda(i\omega)\right]^2}G_\sigma^{(0)}(i\omega)\delta(|\omega| - \Lambda) \tag{3.13}$$

$$\to \delta(|\omega| - \Lambda)G_\sigma^{(0)}(i\omega) \int_0^1 \frac{1}{\left[1 - x \cdot G_\sigma^{(0)}(i\omega)\Sigma_\sigma^\Lambda(i\omega)\right]^2}dx$$

$$= \delta(|\omega| - \Lambda)\frac{1}{G_\sigma^{(0)}(i\omega)^{-1} - \Sigma_\sigma^\Lambda(i\omega)}$$

and

$$S_\sigma^\Lambda(i\omega)G_\sigma^\Lambda(i\omega') \to \delta(|\omega| - \Lambda)\frac{1}{G_\sigma^{(0)}(i\omega)^{-1} - \Sigma_\sigma^\Lambda(i\omega)}\frac{1}{G_\sigma^{(0)}(i\omega')^{-1} - \Sigma_\sigma^\Lambda(i\omega')}\Theta(|\omega'| - \Lambda) \tag{3.14}$$

with $\Theta(0) = 1/2$. For the modified version proposed by Katanin, the combined propagator $\mathcal{P}^\Lambda_{mod} = -d\mathcal{G}^\Lambda/d\Lambda\ \mathcal{G}^\Lambda$ can be explicitly calculated as well and it is found to be

$$-\frac{d}{d\Lambda}G_\sigma^\Lambda(i\omega) \cdot G_\sigma^\Lambda(i\omega') \to \delta(|\omega| - \Lambda)\frac{1}{G_\sigma^{(0)}(i\omega)^{-1} - \Sigma_\sigma^\Lambda(i\omega)}\frac{\Theta(|\omega'| - \Lambda)}{G_\sigma^{(0)}(i\omega')^{-1} - \Sigma_\sigma^\Lambda(i\omega')}$$

$$-\frac{d}{d\Lambda}\Sigma_\sigma^\Lambda(i\omega) \cdot \frac{\Theta(|\omega| - \Lambda)}{[G_\sigma^{(0)}(i\omega)^{-1} - \Sigma_\sigma^\Lambda(i\omega)]^2}\frac{\Theta(|\omega'| - \Lambda)}{G_\sigma^{(0)}(i\omega')^{-1} - \Sigma_\sigma^\Lambda(i\omega')} . \tag{3.15}$$

One can see that the modification does not change the flow equations drastically, but adds another term, that is at least of third order in the bare interaction, since $\dot{\Sigma}^\Lambda$ is at

least of order U. Note, that the additional term in the second line of eq.(3.15) does not contain a factor $\delta(|\nu| - \Lambda)$. This leads to a considerably higher numerical effort in solving the modified version of the flow equations.

To integrate the flow equations, the continuous frequencies have to be discretized. Due to the different energy scales of the problem, it is not possible to use simple linear mesh. To have a sufficiently good resolution at small and intermediate frequencies and still capture the high frequency features, a mesh with increasing stepsize is needed. This can either be achieved by a logarithmic mesh, behaving like $\omega_n = \omega_0 a^n$, or by a geometric mesh, obeying $\omega_n = \omega_0(a^n - 1)/(a - 1)$. In both cases ω_0 is the smallest frequency and a determines how fast the frequencies are growing. It turns out that both approaches give good results, although the second one seems to be slightly better. It needs less frequencies to resolve both, the very small and the intermediate regime, sufficiently well and produces a smoother frequency mesh. A comparison of both approaches is shown in fig.(3.3).
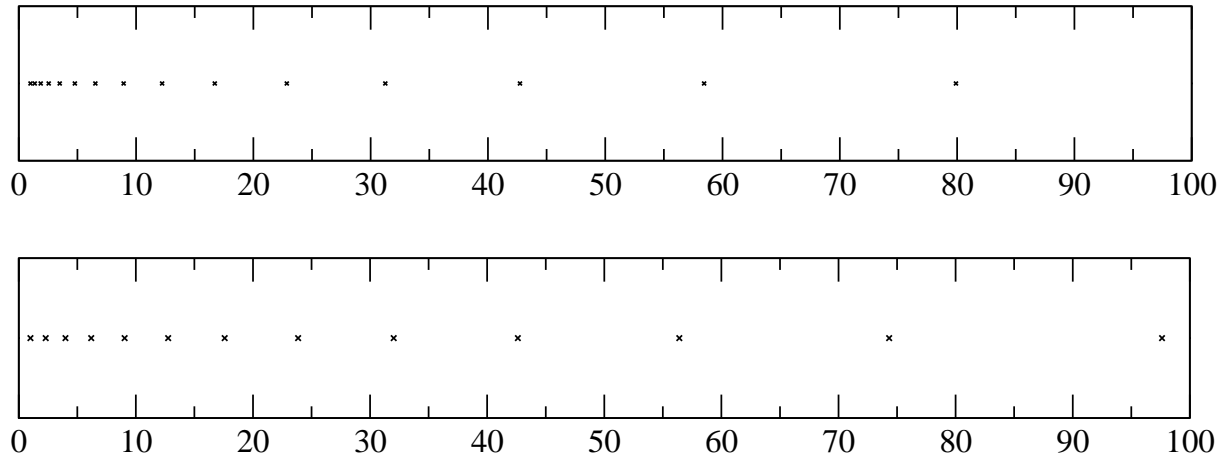
Figure 3.3: Comparison of a exponential (top) and a geometric (bottom) mesh.

The numerical effort rises with the third power of the number of frequencies in the conventional formulation and with the fourth power in the modified version of the fRG. Despite this highly increased numerical effort in the modified version, it will be shown that it is necessary to use this version to obtain good results for $U/\Delta_0 \gtrsim 3$. Especially in the symmetric case, it is surprising that, while 2PTh still shows good agreement with NRG, there is a severe deviation of the fRG results calculated with the unmodified version. For $U/\Delta_0 \gtrsim 7$ it is necessary to use the modified version to obtain any results at all, since the flow of the conventional fRG is divergent for larger U.

The results of second order perturbation theory can be recovered from the flow equations

given above in a relatively simple way, just by replacing Σ^Λ on the rhs of eq.(3.9) and eq.(3.10) and U^Λ on the rhs of eq.(3.10) by their initial values. The new flow equation for the self-energy is then

$$\frac{d}{d\Lambda}\Sigma_\sigma^\Lambda(i\omega) = -\frac{1}{2\pi}\sum_{\alpha=\pm 1}\frac{1}{G_\sigma^{(0)}(i\alpha\Lambda)^{-1}}\Big[2\mathcal{U}^\Lambda(i\omega, i\alpha\Lambda; i\omega, i\alpha\Lambda)- \tag{3.16}$$
$$\mathcal{U}^\Lambda(i\alpha\Lambda, i\omega; i\omega, i\alpha\Lambda)\Big].$$

It is convenient to treat the two terms on the rhs of eq.(3.9) as one function. This is possible, since $\mathcal{U}^\Lambda$ does not enter its own flow equation when reproducing 2PTh. With

$$\mathcal{U}^{\Lambda,2PTh}(i\omega_1', i\omega_2'; i\omega_1, i\omega_2) = 2\mathcal{U}^\Lambda(i\omega_1', i\omega_2'; i\omega_1, i\omega_2) - \mathcal{U}^\Lambda(i\omega_2', i\omega_1'; i\omega_1, i\omega_2)$$

the flow equation for $\mathcal{U}^{\Lambda,2PTh}$ is

$$\frac{d}{d\Lambda}\mathcal{U}^{\Lambda,2PTh}(i\omega_1', i\omega_2'; i\omega_1, i\omega_2) = -\frac{U^2}{2\pi}\sum_{\alpha=\pm 1}\frac{1}{G_\sigma^{(0)}(i\alpha\Lambda)^{-1}}\times \tag{3.17}$$

$$\Bigg[\frac{\Theta(|\omega_1+\omega_2-\alpha\Lambda|-\Lambda)}{G_\sigma^{(0)}(i\omega_1+i\omega_2-i\alpha\Lambda)^{-1}}$$

$$+\Bigg\{\frac{\Theta(|-\omega_1+\omega_1'+\alpha\Lambda|-\Lambda)}{G_\sigma^{(0)}(-i\omega_1+i\omega_1'+i\alpha\Lambda)^{-1}-\Sigma_\sigma^\Lambda(-i\omega_1+i\omega_1'+i\alpha\Lambda)}$$

$$+(1'\leftrightarrow 2'; 1\leftrightarrow 2)\Bigg\}$$

$$-2\Bigg\{\frac{\Theta(|-\omega_1+\omega_2'+\alpha\Lambda|-\Lambda)}{G_\sigma^{(0)}(-i\omega_1+i\omega_2'+i\alpha\Lambda)^{-1}-\Sigma_\sigma^\Lambda(-i\omega_1+i\omega_2'+i\alpha\Lambda)}$$

$$+(1'\leftrightarrow 2'; 1\leftrightarrow 2)\Bigg\}\Bigg]$$

for the frequency dependent part of the two-particle vertex. Especially the last equation is simplified compared to eq.(3.10).

These equations can be used to numerically calculate results for 2PTh relatively easily. In the special case of particle-hole-symmetry it is even possible to solve the flow-equations analytically. Since the self-energy does not couple to the equation of the two-particle
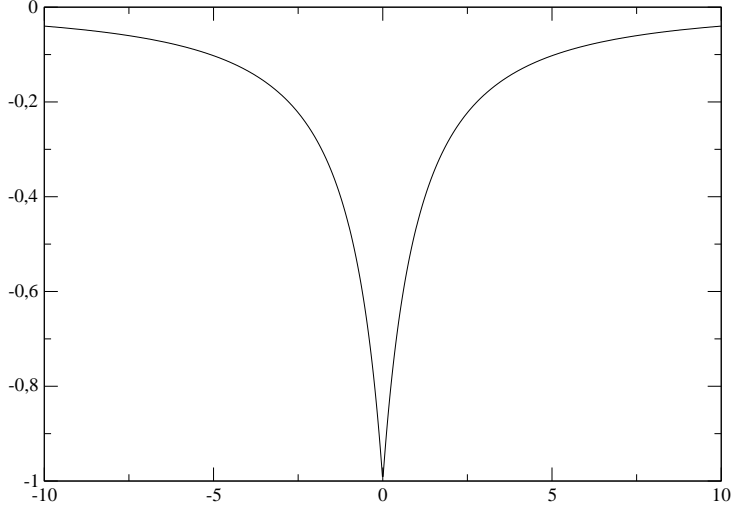
Figure 3.4: The frequency dependence of each term in eq.(3.19).

vertex any more, the two-particle vertex can be calculated, solving elementary integrals of the form

$$\int \frac{1}{\omega + \Delta_0} \frac{1}{\tilde{\omega} + \omega + \Delta_0}.$$

(3.18)

The result for the frequency dependent part of the two-particle vertex is

$$
\begin{aligned}
\mathcal{U}^{2PTh}(i\omega_1', i\omega_2'; i\omega_1, i\omega_2) &= U \\
&+ \frac{U^2}{\pi} \left[\ln \frac{\Delta_0}{\Delta_0 + |\omega_1' + \omega_2'|} \left(\frac{1}{|\omega_1' + \omega_2'|} - \frac{1}{|\omega_1' + \omega_2'| + 2\Delta_0} \right) \right. \\
&+ \ln \frac{\Delta_0}{\Delta_0 + |\omega_1' - \omega_1|} \left(\frac{1}{|\omega_1' - \omega_1|} - \frac{1}{|\omega_1' - \omega_1| + 2\Delta_0} \right) \\
&- \left. 2 \ln \frac{\Delta_0}{\Delta_0 + |\omega_2' - \omega_1|} \left(\frac{1}{|\omega_2' - \omega_1|} - \frac{1}{|\omega_2' - \omega_1| + 2\Delta_0} \right) \right].
\end{aligned}
$$

(3.19)

To calculate the self-energy, one has to calculate U^Λ for finite Λ. Inserting this result into the equation for the self-energy, one is left with another integration. The result for the self-energy cannot be expressed by elementary functions. But using the dilogarithmic function

$$\mathrm{dilog}(x) = \int_1^x \frac{\ln t}{1 - t} \, dt,$$

(3.20)

32

it is found to be

$$
\begin{aligned}
\mathrm{Im}\Sigma^{PTh}(i\omega) = \quad & \frac{3iU^2}{2\pi^2}\Bigg[\mathrm{dilog}\left(\frac{\Delta_0}{\Delta_0+\omega}\right)\left(\frac{1}{\omega-\Delta_0}-\frac{1}{\omega+\Delta_0}\right) \\
& +\mathrm{dilog}\left(1+\frac{\Delta_0}{\Delta_0+\omega}\right)\left(\frac{1}{\omega+\Delta_0}-\frac{1}{\omega+3\Delta_0}\right) \\
& +\ln\left(\frac{\Delta_0}{\Delta_0+\omega}\right)\ln\left(1+\frac{\Delta_0}{\Delta_0+\omega}\right)\left(\frac{1}{\omega+\Delta_0}-\frac{1}{\omega+3\Delta_0}\right) \\
& +\frac{1}{2}\ln\left(\frac{\Delta_0}{\Delta_0+\omega}\right)^2\left(\frac{1}{\omega-\Delta_0}-\frac{2}{\omega+\Delta_0}+\frac{1}{3\Delta_0+\omega}\right) \\
& -\frac{\pi^2}{12}\left(\frac{1}{\omega-\Delta_0}+13\Delta_0+\omega\right)\Bigg] .
\end{aligned}
\tag{3.21}
$$

An analytic result for the self-energy from 2PTh for real frequencies has been calculated in [31]. A closer look to the frequency dependent part of the two-particle vertex shows that it consists of three parts. Each part has basically the same structure and each part depends on a combination of frequencies namely $\nu_1 = \omega_1 + \omega_2$, $\nu_2 = \omega_1' - \omega_1$ and $\nu_3 = \omega_2' - \omega_1$. A fourth frequency is not needed because of frequency conservation. While for large ν_i the frequency dependence tends to zero, the interesting structures appear for small ν_i. The form of the frequency dependence of each single part is shown in fig.(3.4). An analysis of $\mathcal{U}$ resulting from integrating the full fRG equations shows the same global behaviour. There are peaked structures around $\nu_i = 0$, and for large ν_i $\mathcal{U}$ is constant. This can be seen quite well in a contour plot of $\mathcal{U}$ shown in fig.(3.5). The single peaks result from the discrete frequency mesh. The quantitative behaviour is of course different from the one found in 2PTh. One might now argue, that using these new frequencies for the frequency mesh of $\mathcal{U}$ would be better, since the structures for small frequencies would be resolved more precisely. This is indeed possible, but numerically it turns out that using the new frequencies ν_i instead of the old ones gives the same result for a sufficiently smooth mesh. Even more, using the new frequencies the dependence on the number of used frequencies and the smoothness of the mesh are increased compared to the old ω_i. This might be due to the fact that even though the structure of the frequency dependence is better resolved with the ν_i, the number of evaluations of $\mathcal{U}$ at interpolated frequencies rises significantly. This already becomes apparent in the equation for the self-energy. In eq.(3.9) each $\mathcal{U}^\Lambda(i\nu_1', i\nu_2'; i\nu_1, i\nu_2)$ has one entry that is not an exact frequency from the discretized mesh and therefore has to be interpolated somehow. The equation for the
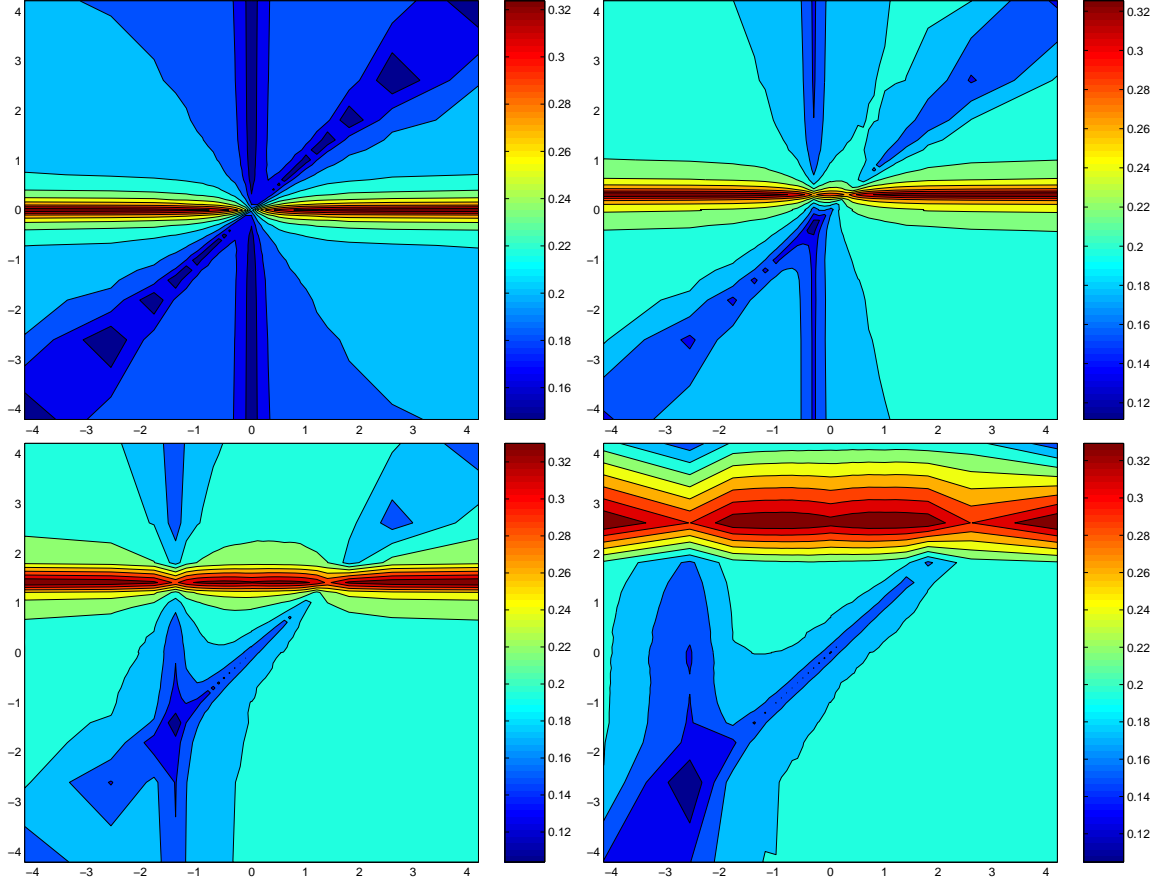
Figure 3.5: Contour plot of the frequency dependent part of the two-particle vertex from fRG for $U/\Delta_0 = 1$. ω_1' and ω_1 are varied in $x-$ and $y-$directions. The four panels show the contour for various values of ω_2'. The structure that can analytically be found in 2PTh is clearly visible. There are peaked structures for $\omega_1' = -\omega_2'$, $\omega_1' = \omega_1$ and for $\omega_2' = \omega_1$.

self-energy using the ν_i reads

$$\frac{d}{d\Lambda}\Sigma_\sigma^\Lambda(i\omega) = -\frac{1}{2\pi}\sum_{\alpha=\pm 1}\frac{1}{G_\sigma^{(0)}(i\alpha\Lambda)^{-1} - \Sigma_\sigma^\Lambda(i\alpha\Lambda)}\Big[2\mathcal{U}^\Lambda(i\omega + i\alpha\Lambda, 0.0; i\alpha\Lambda - i\omega) - \quad (3.22)$$
$$\mathcal{U}^\Lambda(i\alpha\Lambda + i\omega, i\alpha\Lambda - i\omega; 0.0)\Big].$$

It can be seen very clearly that here $\Lambda + \nu$ and $\Lambda - \nu$ will both not be contained in the frequency mesh for most values of Λ. The number of entries, at which one has to interpolate instead of using the exact known value, has risen by a factor of two. One can easily convince oneself that the same happens in the equation for $\mathcal{U}^\Lambda$. The gain from the better resolution for small frequencies can obviously not compensate for a higher number

of necessary interpolations.

In chapter 2 it was mentioned that for applications of the fRG to other, especially one- and two-dimensional problems, further approximations to the flow equations were made while still obtaining surprisingly good results, e.g. [12]-[16]. Looking at the complicated structure of the flow equations, in particular the one for $\mathcal{U}^\Lambda$, the question arises whether further approximations can be made in this context without losing too much of the quality of the fRG result. This question will be addressed later in this chapter. The flow equations that recover 2PTh for example are a lot easier to treat because knowledge of $\mathcal{U}^\Lambda$ is only needed on a two-dimensional frequency mesh, since it does not enter the rhs of eq.(3.17) anymore. This reduces the numerical effort considerably. It should be noted, that as long as an approximation is made somewhere between eq.(3.9) and eq.(3.10) on one side and eq.(3.16) and eq.(3.17) on the other side, the approximate result is still exact up to second order in the bare interaction U. This will be discussed in some detail later on. For now, only the full flow equations up to order $m_c = 2$ will be considered.

3.5   Results

In this section, results for the self-energy calculated by integrating the fRG flow equations and the corresponding spectral function, obtained by performing an analytical continuation using Padé approximation, will be presented and compared to the results from 2PTh, which are known to be surprisingly good at least in the symmetric case, and to NRG, which is known to be in excellent agreement with the exact result. Selected observables will be calculated and compared as well. From the results of these comparisons it will be possible to analyze the quality and reliability of fRG. This can be used to make a statement on the question in which parameter regimes fRG can be used to describe the dynamics of more complex Anderson impurity systems treated in the following chapters.

3.5.1   Particle-hole-symmetric case

From the fRG one naturally obtains vertex functions for imaginary frequencies, so the first thing to look at is the self-energy $\Sigma(i\omega)$ on the imaginary axis. In the particle-hole-symmetric case, $\epsilon_d = -U/2$, on the imaginary axis the real part of the self-energy
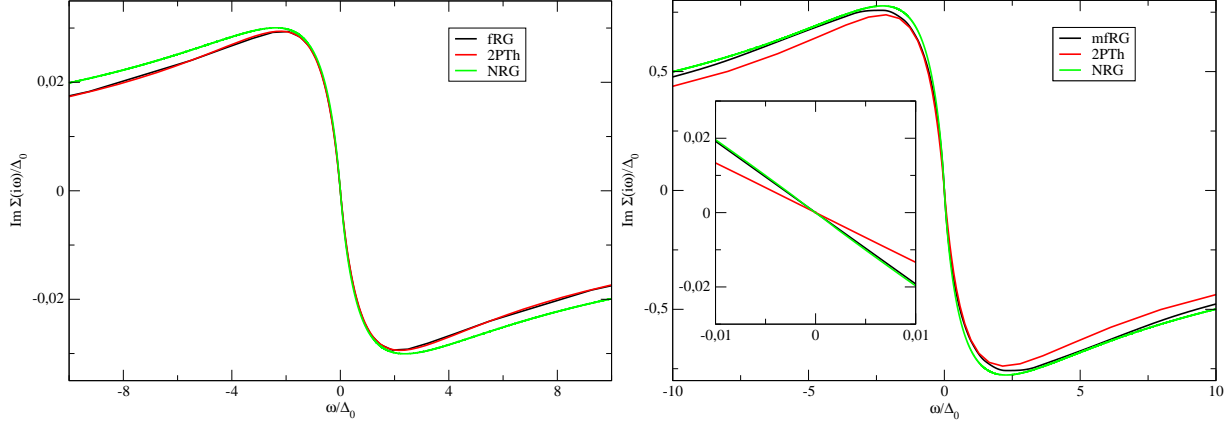
Figure 3.6: Imaginary part of the self-energy for $U/\Delta_0 = 1$ (left) and $U/\Delta_0 = 5$ (right) from mfRG, 2PTh and NRG.

is exactly $U/2$ while the frequency dependence is completely contained in the imaginary part of the self-energy. This imaginary part Im $\Sigma(i\omega)$ is shown in the left panel of fig.(3.6) for $U/\Delta_0 = 1$, which is a rather small value. No discrepancy between perturbation theory and fRG can be found. The discrepancies for large ω compared to the NRG-curve are due to broadening effects in the NRG. When the interaction strength U is increased to intermediate values up to $U/\Delta_0 = 5$, the overall picture does not change too much as long as the modified version of the fRG is used. This can be seen in fig.(3.6) (right panel) quite clearly. All three curves are in good agreement. A closer look to the low energy regime (inset) reveals a change. While the slope of the 2PTh curve is too small, mfRG and NRG are hardly distinguishable. Fig.(3.7) shows a comparison between the conventional fRG and mfRG for $U/\Delta_0 = 5$. It is obvious that the curve obtained from the unmodified scheme is not describing the problem very well. For larger interaction strength the situation gets even worse and roughly from $U/\Delta_0 = 7$ on, the conventional scheme is not usable at all, since the integration of the flow equations fails. Of course the question arises, whether this might be due to the discretization of the frequency mesh or whether this is a genuine problem of the truncated flow equations. Since it is not possible to analytically find a reason for this divergency, a rigorous answer is not possible. But for a given U the value of the flow-parameter Λ, where the flow diverges, is almost independent of the choice of the frequency mesh. This is a strong indication that the problem is not caused by the discretization but is caused by the flow equations themselves. However, using the modified scheme, divergences are no problem and curves for larger values of
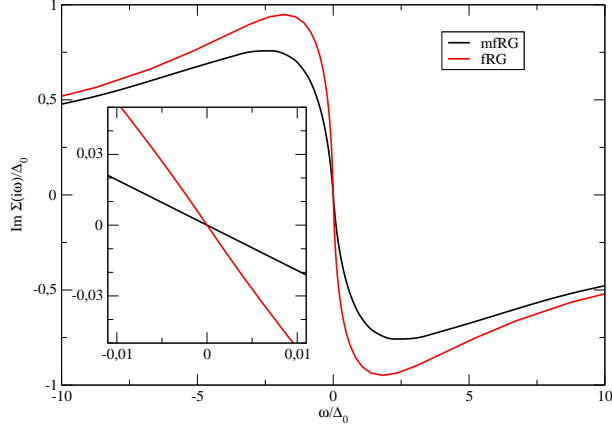
Figure 3.7: Imaginary part of the self-energy calculated with the conventional and the modified fRG scheme; $U/\Delta_0 = 5$.

U/Δ_0 can be calculated. It is known that with perturbatively motivated truncations of the flow equations, fRG fails to correctly describe the behaviour of strong coupling systems. This becomes apparent here as well. The self-energy curves for $U/\Delta_0 = 7.5$ (fig.(3.8), left panel) and $U/\Delta_0 = 10$ (right panel) show a growing discrepancy between mfRG and NRG. The overall shape is still correct but the quantitative agreement is getting poorer. It is surprising to some extend that for those values of U/Δ_0 2PTh shows a better general agreement with NRG than mfRG does. Later on it will be shown that this is a specific feature of the particle-hole-symmetric case, in which 2PTh is known to work much better than in the more general asymmetric case. It was shown for $U/\Delta_0 = 5$
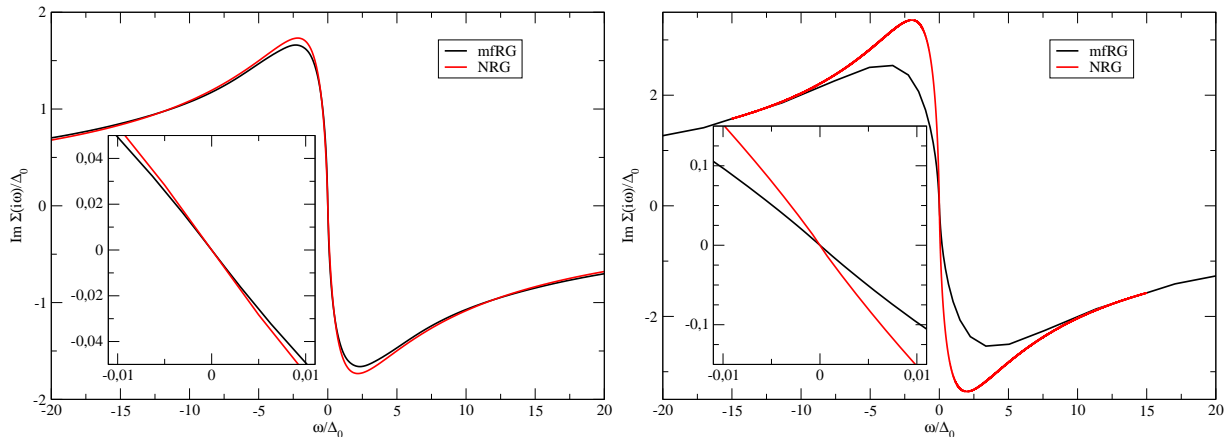
Figure 3.8: Imaginary part of the self-energy; left: $U/\Delta_0 = 7.5$, right: $U/\Delta_0 = 10$, insets show the low-energy region.

37
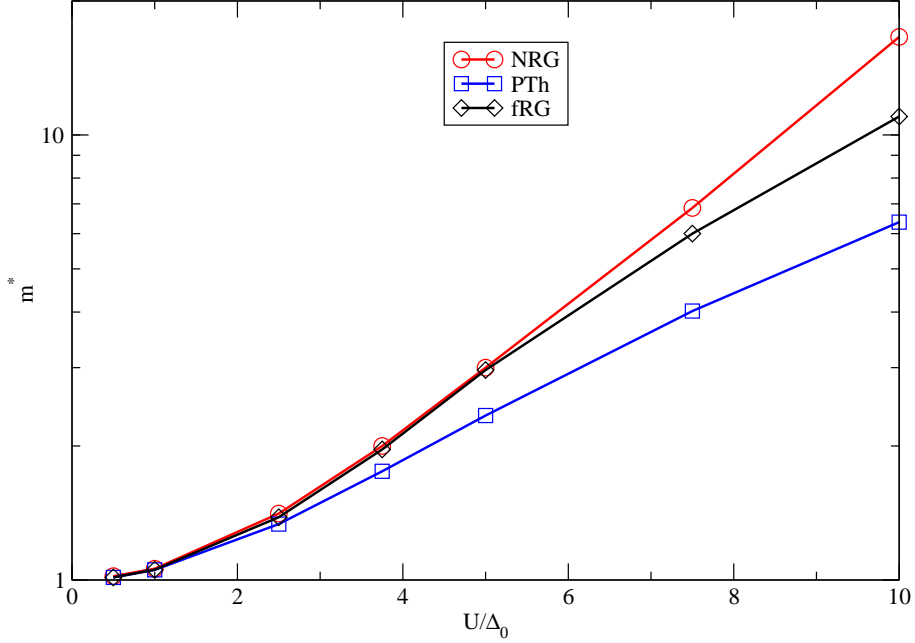
Figure 3.9: The effective mass from mfRG, 2PTh and NRG

that mfRG shows a low energy behaviour which is superior to the one of 2PTh even in the symmetric case. This can be extended to larger U/Δ_0 as fig.(3.8) clearly shows. For a further analysis of this low-energy behaviour, a look at the effective mass is useful. This quantity is closely connected to the Kondo temperature [22]. Basically, the Kondo temperature is given by the inverse effective mass. The exact value, as obtained from NRG, will show an exponential behaviour in U/Δ_0 in the strong coupling regime. It can be obtained from the self-energy by

$$m^* = 1 + \lim_{\omega \searrow 0} \frac{\Im m \Sigma(i\omega)}{\omega}.$$

In fig.(3.9) the effective mass determined from mfRG, 2PTh and NRG are displayed. It is obvious that mfRG cannot reproduce the effective mass obtained from NRG and does not show an exponential behaviour. Nevertheless, it is a clear improvement compared to 2PTh. Via the Kondo temperature the effective mass is directly connected to the width of the Kondo resonance in the spectral function, which is therefore described much better with mfRG than with 2PTh.

The point where the results from mfRG start to lose accuracy coincides with the value of U where the slope of the curve in fig.(3.9) is decreasing. Furthermore, the analysis
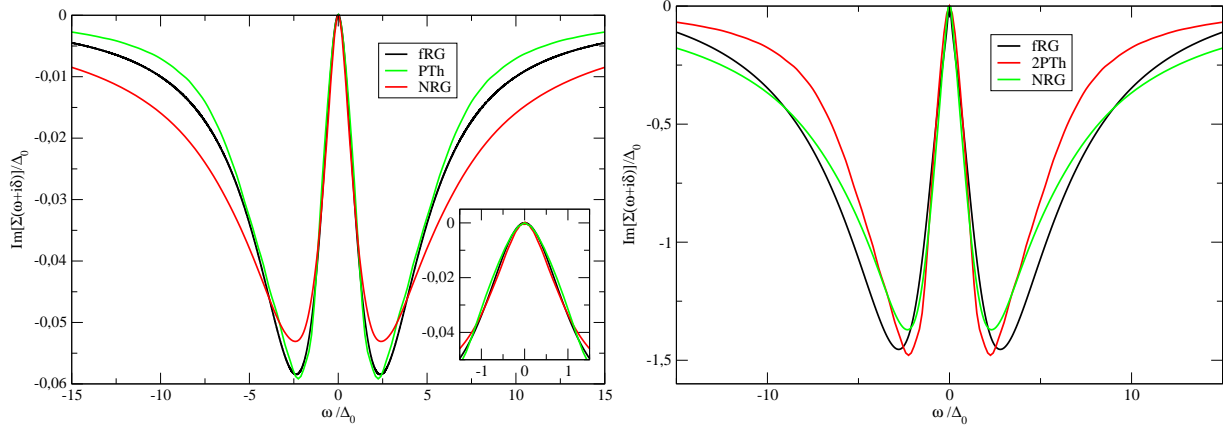
Figure 3.10: Analytical continuation of curves shown in fig.(3.6); left: $U/\Delta_0 = 1$, right: $U/\Delta_0 = 5$.

of the effective mass allows to connect the quality of the mfRG results to the Kondo temperature. This criterion allows to make an estimate for the value of U/Δ_0 up to which fRG results can be trusted in systems where no data from other reliable methods is available for comparison.

Using Padé approximation, it is possible to determine an analytic continuation to the real axis from the self-energy calculated on the imaginary axis. Even though both, real and imaginary part, show a non-trivial frequency dependence already in the symmetric case, it is sufficient to study the imaginary part of the self-energy on the real axis Im $\Sigma(\omega + i0)$ since the real part can be calculated from the imaginary part by Hilbert transformation:

$$Re\Sigma(\omega + i0) = -\frac{1}{\pi} \int \frac{Im\Sigma(\epsilon + i0)}{\omega - \epsilon} \ . \tag{3.23}$$

On the real axis the symmetries of the real and the imaginary part are inverted. While the imaginary part is symmetric ($Im\Sigma(\omega + i0) = Im\Sigma(-\omega + i0)$), the real part is point symmetric. In a neighbourhood around $\omega = 0$ the imaginary part of the self-energy displays a parabolic behaviour. The width of the corresponding parabola is given by the effective mass of the electrons. This is the region in which the Fermi liquid description of the low energy physics is valid.

 For the curves shown in fig.(3.6) the imaginary part of the self-energy for real frequencies can be seen in fig.(3.10). The excellent agreement between mfRG and NRG is still clearly visible. Having determined the self-energy on the real axis, the spectral function is given
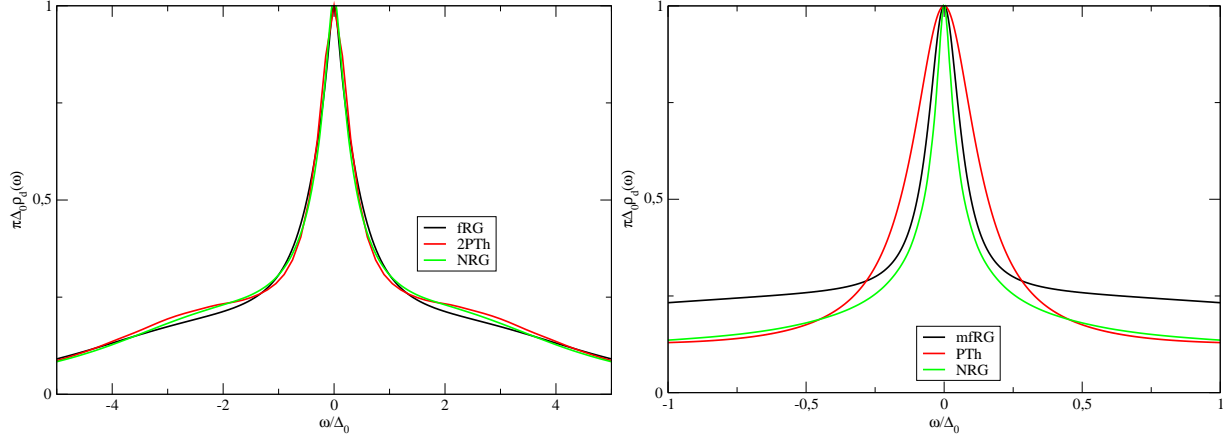
Figure 3.11: Spectral functions or $U/\Delta_0 = 5$ (left) and $U/\Delta_0 = 10$ (right); in the panel only the low-energy region is shown.

as the imaginary part of the impurity Green function

$$\rho_d(\omega) = -\frac{1}{\pi}\text{Im}\mathcal{G}_d(\omega + i0) \ . \tag{3.24}$$

The different spectral functions for $U/\Delta_0 = 5$ and $U/\Delta_0 = 10$ are shown in fig.(3.11). In the first case the agreement between all three curves is very good. In the low energy region the mfRG provides a clear improvement to the 2PTh curve. This can in particular be seen for $U/\Delta_0 = 10$ in the right panel. Furthermore the lineshape of the mfRG Kondo resonance does obviously not follow a simple Lorentzian but rather a more complex form like NRG and as predicted in [27]. The development of the spectral functions from mfRG alone is displayed in fig.(3.12). The formation of the resonance at the chemical potential is clearly visible, while at the same time spectral weight is shifted towards the forming atomic peaks. Comparing the spectral functions one should keep in mind that, while the low energy behaviour can be described very reliable with Padé approximation, the details of the atomic peaks are a lot more difficult to obtain from Padé approximation. For a quantitative analysis one should either concentrate on the low-energy behaviour or on data that can be directly obtained using imaginary frequencies.

To summarize the above, the mfRG results are in excellent agreement with the exact data for small and intermediate interaction strength. For larger U the quality of the results is reduced. In the special case of particle-hole-symmetry an improvement compared to 2PTh can only be made in the low-energy region.
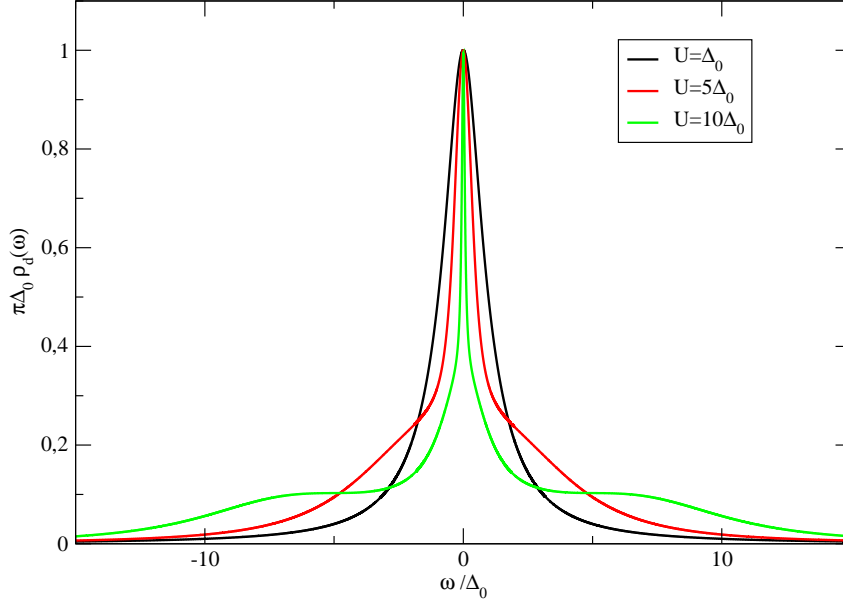
Figure 3.12: Spectral functions from fRG for different U/Δ_0.

3.5.2 The asymmetric case

In the asymmetric case both, the imaginary part of the self-energy and the real part, contain relevant information. On one side the constant value of the real part for large frequencies is important, especially for calculating the occupation of the impurity level. On the other side it develops a frequency dependence that is important for the dynamics of the system. For this reason, in this section both, imaginary and real part of the self-energy, will be investigated.

The curves in fig.(3.13) show the real and imaginary part of $\Sigma(i\omega)$ for $U/\Delta_0 = 1$ and

$\epsilon_d + U/2 = U/4$ for NRG, fRG and 2PTh. Already for this rather small interaction strength a difference between the perturbative result and the other two curves, which are hardly distinguishable, is visible. With growing interaction strength this is getting even more visible. For $U/\Delta_0 = 2.5$ and again $\epsilon_d + U/2 = U/4$ the situation is depicted in fig.(3.14). While in the symmetric case for this value of the bare interaction still excellent agreement between all three curves can be observed, here only fRG reproduces the NRG curve. 2PTh is quantitatively wrong already for rather small U. It becomes obvious that 2PTh does not only get the frequency dependence wrong, but also the constant
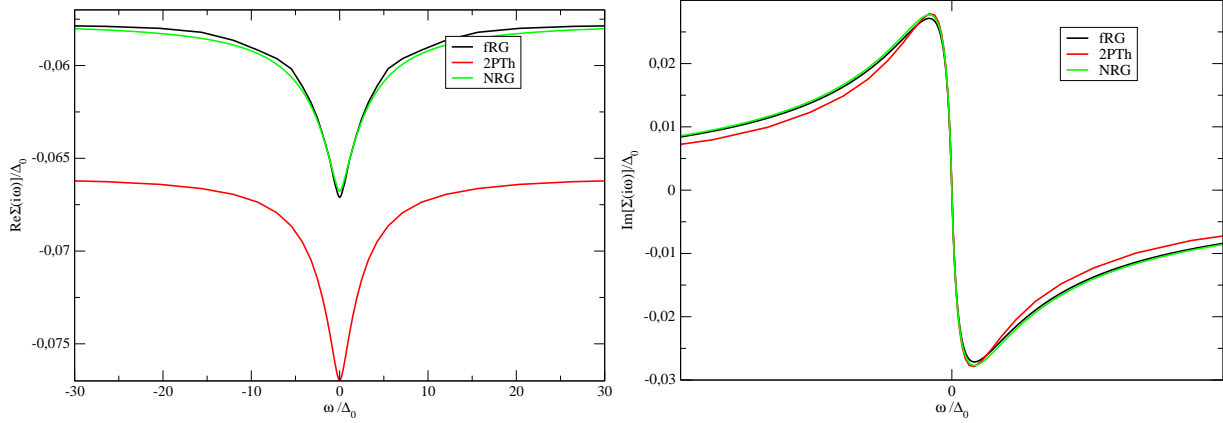
Figure 3.13: Self-energy from fRG, 2PTh and NRG for $U/\Delta_0 = 1$ and $\epsilon_d = -U/4$.
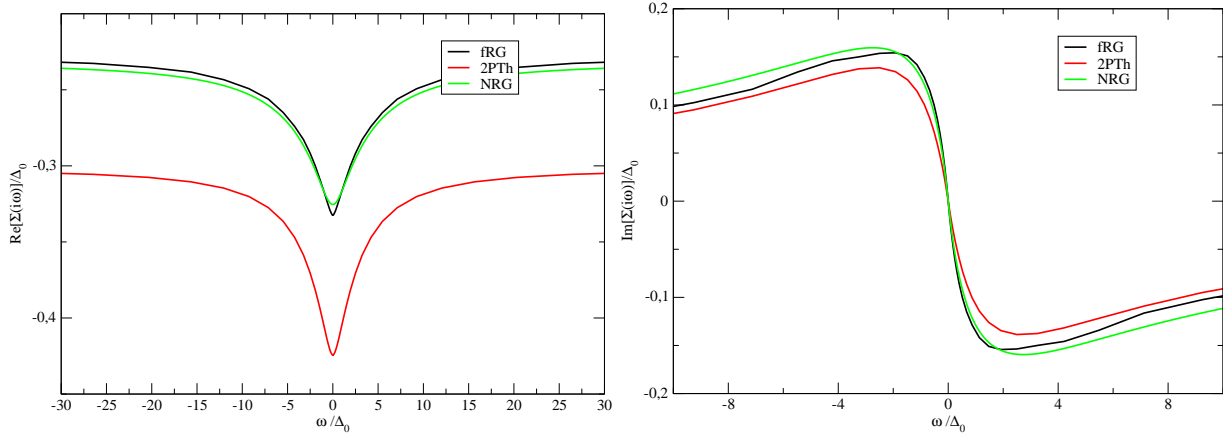

Figure 3.14: Self-energy from fRG, 2PTh and NRG for $U/\Delta_0 = 2.5$ and $\epsilon_d = -U/4$.

value of the real part for large frequencies differs from the NRG result, while fRG is still correct. For larger U/Δ_0 it becomes even more apparent how 2PTh results get worse for increasing asymmetry, while fRG still gives accurate curves compared to NRG data. For $U/\Delta_0 = 2\pi$ and various ϵ_d this is shown in fig.(3.15). Looking at the right panel it becomes obvious, that the real part acquires a constant contribution that counteracts the shift of the impurity level. The stronger the interaction is, the smaller is the effective shifting of the impurity level. As a consequence of this behaviour, the shift of the Kondo resonance is suppressed. Additionally the occupancy is kept close to one. This will be discussed further down.
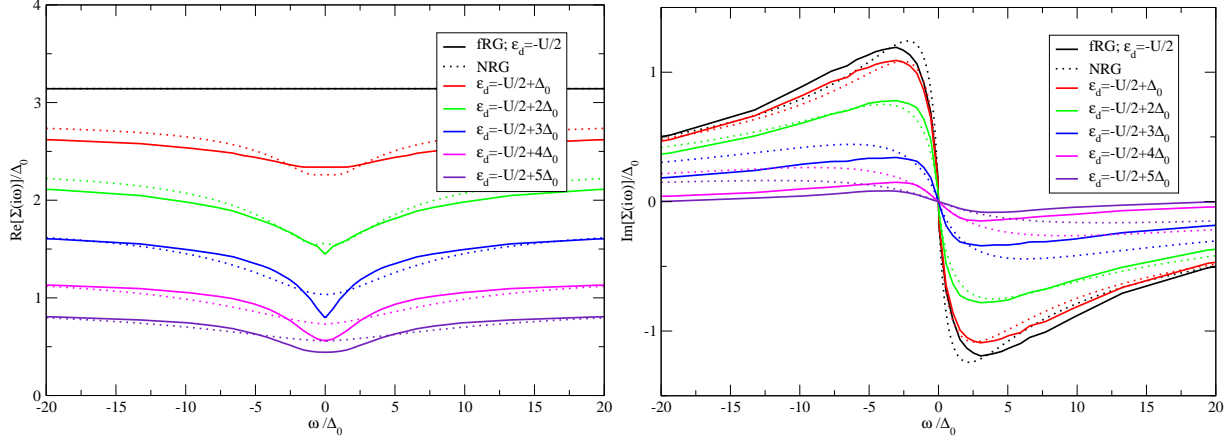
Figure 3.15: Self-energy for $U/\Delta_0 = 2\pi$ and various ϵ_d; fRG curves are shown as solid lines, NRG curves are dotted.

The spectral functions shown in fig.(3.16) for mfRG and NRG for various interaction strength and $\epsilon_d + U/2 = U/4$ show exactly this behaviour. The Kondo resonance is pinned to the chemical potential. The stronger the interaction is, the stronger is the pinning effect. Especially the Kondo resonance is described very well by mfRG. For $U/\Delta_0 = 2\pi$ the spectral functions calculated with mfRG are presented in fig.(3.17). It is clearly visible, that the Kondo resonance shifts slightly to the right, but the shift is much
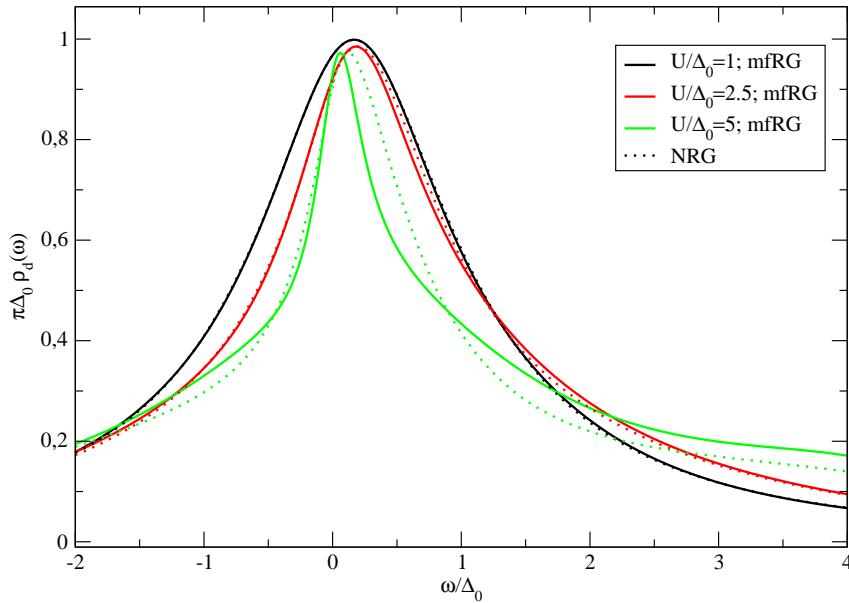

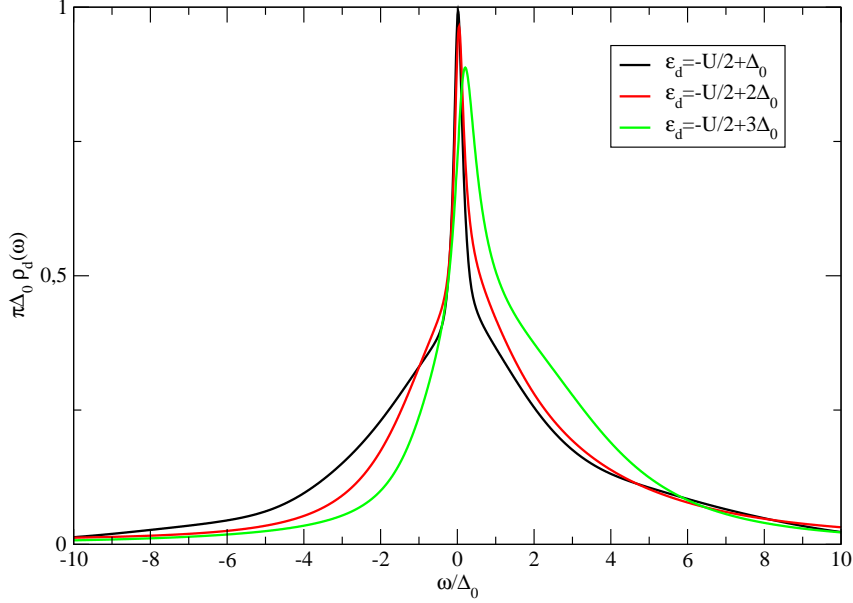Figure 3.16: Spectral functions from fRG for different U/Δ_0 and $\epsilon_d = -U/4$.

Figure 3.17: Spectral functions from fRG for $U/\Delta_0 = 2\pi$ and different ϵ_d.

smaller than the absolute value of the impurity level shift. Additionally the frequency dependence of the real part of the self-energy causes the spectral function to lose its symmetry. For 2PTh no spectral functions are presented. From the discrepancy in the self-energy curves it is already clear that they are not appropriate to correctly describe the dynamics away from the Lorentzian behaviour around $U = 0$.

One observable of interest in the asymmetric case is the filling of the impurity level. This occupancy can be calculated relatively easily. Starting from $\Sigma(i\omega)$ this can be basically done in three ways. The simplest one is to use the generalized Friedel sum rule [22], which relates the occupancy of the impurity level to the real part of the self energy at the Fermi level, i.e. at $\omega = 0$,

$$\langle n \rangle_{Fr} = 1 - \frac{2}{\pi} \arctan \frac{\epsilon_d + \mathrm{Re}\Sigma(0)}{\Delta} \ . \tag{3.25}$$

This especially allows to calculate the occupancy of the impurity level without including frequency dependence. For some applications this can be quite useful, e.g. for the calculation of the static spin susceptibility that is presented later on. Another way is to calculate $\langle n_d \rangle$ from the Green function on the imaginary axis according to

$$\langle n \rangle_{Gr} = \lim_{\delta \to 0} \int_{-\infty}^{\infty} \frac{d\omega}{2\pi} G(i\omega) e^{i\omega\delta} \ . \tag{3.26}$$

44

The third method is to directly calculate the occupation number from its flow equation using eq.(2.31) and eq.(2.33). Of course the occupation number could also be calculated from the spectral function using

$$\langle n \rangle = \int_{-\infty}^{0} d\omega \rho_d(\omega) \tag{3.27}$$

as well. But since the process of Padé approximation was necessary to obtain the spectral function, it seems favourable to choose a method depending on the imaginary axis data only, since the quantitative accuracy of the analytic continuation is hard to determine especially away from the Kondo resonance. The results are shown in the table further down for various levels of asymmetry and for $U/\Delta_0 = 2\pi$ and for fRG and NRG. 2PTh results are not shown since it has already been made clear that the perturbative result shows strong deviations from the correct result.

$(\varepsilon_d + \frac{U}{2})/\Delta_0$	$\langle n \rangle_{Fr}$; NRG	$\langle n \rangle_{Gr}$; NRG	$\langle n \rangle_{Fr}$; fRG	$\langle n \rangle_{Gr}$; fRG	$\langle n \rangle_{flow}$; fRG
0	1.00	1.00	1.00	1.00	1.00
1	0.92	0.91	0.90	0.91	0.86
2	0.76	0.76	0.79	0.79	0.71
3	0.53	0.55	0.62	0.56	0.53
4	0.36	0.38	0.39	0.36	0.35

Comparing the three ways of calculating $\langle n_d \rangle$, it becomes apparent that $\langle n \rangle_{Fr}$ and $\langle n \rangle_{Gr}$ agree more or less. This means that mfRG does fulfill the Friedel sum rule. For larger asymmetries minor deviations show up. In these cases eq.(3.26) gives the better result. Looking at the numbers, it is immediately obvious that the impressions from comparing the self-energy curves are confirmed by these numbers. The occupancy calculated from mfRG agrees extremely well with the one from NRG. The influence of the impurity level shift on the occupancy calculated from 2PTh is too strong. fRG and NRG show a stronger tendency of the interacting system to keep the occupancy near 1. The conclusion is that mfRG is capable of reliably describing the properties for small and intermediate interaction strength regardless of the other parameters. 2PTh only works well in the specific situation of particle-hole-symmetry. The results from the flow-equations for the density are not very convincing in this case.

Another observable that can be quite easily calculated is the static impurity spin suscep-

tibility defined as

$$\chi = \frac{d}{dh}(n_\uparrow - n_\downarrow)\Big|_{h=0} , \tag{3.28}$$

where h is an external magnetic field. This is introduced in the model by just shifting the impurity level positions for electrons with up and down spin by $\pm h/2$, which leads to different free propagators for spin up and down electrons. Consequently the vertex functions develop a dependence on the spin direction as well. This has to be taken into account when parametrizing the two-particle vertex. Now there is a channel for the interaction between two spin up electrons, two spin down electrons and between a spin up and a spin down electron. The new parametrization of the two-particle vertex is given by

$$\bar\gamma_2^\Lambda(\xi_1', \xi_2'; \xi_1, \xi_2) \quad = \quad \delta(\omega_1 + \omega_2 - \omega_1' - \omega_2') \qquad\qquad . \tag{3.29}$$

$$\Big\{ \delta_{\sigma_1,\sigma_2}\delta_{\sigma_1',\sigma_2'}\delta_{\sigma_1,\sigma_1'}\ \mathcal{U}_\uparrow^\Lambda(i\omega_1', i\omega_2'; i\omega_1, i\omega_2)$$

$$+\delta_{\sigma_1,\sigma_2}\delta_{\sigma_1',\sigma_2'}\delta_{\sigma_1,\sigma_1'}\ \mathcal{U}_\downarrow^\Lambda(i\omega_1', i\omega_2'; i\omega_1, i\omega_2)$$

$$+\delta_{\sigma_1,-\sigma_2}\delta_{\sigma_1',-\sigma_2'}\Big(\delta_{\sigma_1,\sigma_1'}\mathcal{U}_{\uparrow\downarrow}^\Lambda(i\omega_1', i\omega_2'; i\omega_1, i\omega_2)$$

$$-\delta_{\sigma_1,-\sigma_1'}\mathcal{U}_{\uparrow\downarrow}^\Lambda(i\omega_2', i\omega_1'; i\omega_1, i\omega_2)\Big)\Big\}$$

In complete analogy to the procedure described above, flow equations for $\mathcal{U}_\uparrow^\Lambda$, $\mathcal{U}_\downarrow^\Lambda$, $\mathcal{U}_{\uparrow\downarrow}^\Lambda$, $\Sigma_\uparrow^\Lambda$ and $\Sigma_\downarrow^\Lambda$ are derived.

The results for approximations neglecting the frequency dependence can be found in [15]. In the simplest case, i.e. particle-hole symmetry, the $\mathcal{U}_i^\Lambda$ in the flow equations for the self-energy are replaced by their initial value. The static spin susceptibility can then be analytically calculated to be

$$\chi^{approx} \propto \exp\frac{U}{\pi} . \tag{3.30}$$

In the symmetric case the inclusion of the flow of $\mathcal{U}_i^\Lambda$ (without frequency dependence) does not change the exponential behaviour and the exponent is unchanged. Only the prefactor and consequently the absolute value of the susceptibility is improved. In fig.(3.18) the static spin susceptibility is shown depending on the interaction strength U calculated with fRG neglecting the frequency dependence of $\mathcal{U}_i^\Lambda$ and Σ^Λ, with NRG and with fRG
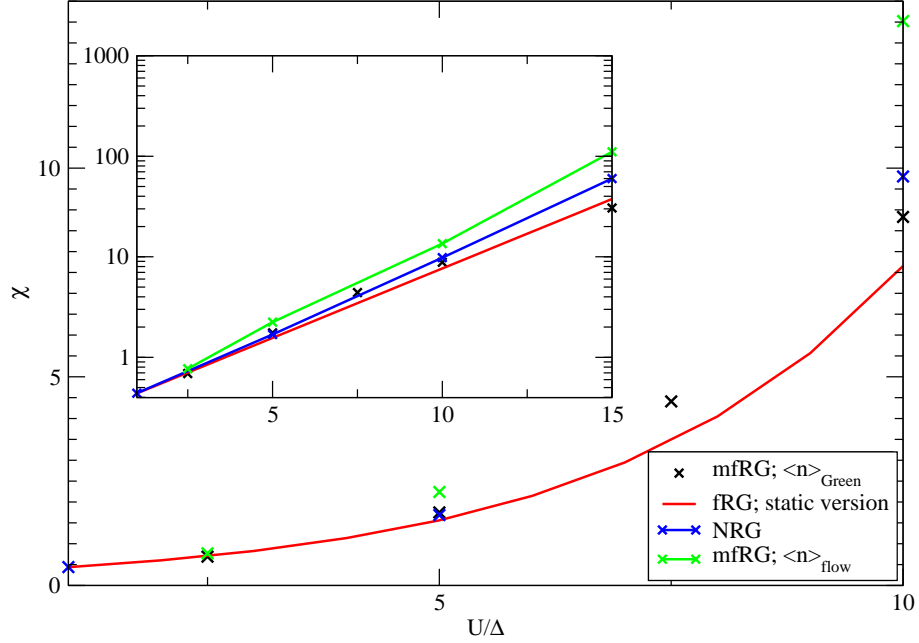
Figure 3.18: Static spin susceptibility calculated with fRG and different levels of approximation; NRG curve for comparison.

including frequency dependence. The exponential behaviour of data from NRG and the static version of fRG is clearly visible. One should expect these results to improve when including the frequency dependence. This is however only partially the case. Like for the effective mass, where NRG predicts exponential behaviour in the strong coupling regime as well, the frequency dependent fRG cannot deliver an exponential behaviour. For small to intermediate U the absolute value of the susceptibility improves and gets very close to the exact NRG value. But on the same scale as for the effective mass, around $U/\Delta_0 = 10$, the result gets worse before really reaching the strong coupling regime. The conclusion of this is that the fRG, including frequency dependence of the self-energy, can be used to very accurately calculate dynamic and static properties for not too large interaction strengths. The exponential behaviour in the strong coupling regime cannot be reproduced in contrast to the case when frequency dependence is neglected. When calculating the susceptibility from $\langle n \rangle_{flow}$, like for the occupancy the results are quantitatively not convincing in the region where fRG gives accurate results. However, they are more suitable than the other methods to describe the behaviour for large interaction strength, as the inset with the logarithmic scale shows. The flow equation for the density seems to include terms that are important at large U, while the prefactors at smaller U are described less accurately.

It should be noted that the approximations neglecting frequency dependence are less accurate concerning absolute values. This is due to prefactors that play an important role before the spin susceptibility is described by the exponential behaviour in the strong coupling regime.

3.6   Further Approximations

It has been indicated already that it is possible to make further approximations to simplify the integration of the flow equations. Since the frequency dependence of the self-energy is only generated by the frequency dependence of the two-particle vertex, any approximation replacing $\mathcal{U}^{\Lambda}(i\omega_1', i\omega_2'; i\omega_1, i\omega_2)$ by a constant, i.e. not frequency dependent, value, like it has been done in other cases, e.g [15], is not sensible here. The most basic way to calculate a frequency dependent two-particle vertex using flow equations is reproducing 2PTh as it has been presented above. There are a few possible intermediate approximations between 2PTh and using the full flow equations for $m_c = 2$. A short discussion of the quality of these approximations shall be given here.

Starting from 2PTh as calculated from eq.(3.16) and eq.(3.17), the first step towards the full fRG equations is to include the self-energy corrections on the rhs of eq.(3.16) again, while calculating $\mathcal{U}^{\Lambda}$ using 2PTh. In the following this scheme is referred to as approximation 1 (App1). Including the self-energy on the rhs of eq.(3.17) as well is the next approximation. Comparing it to the full fRG equations this is achieved by replacing $\mathcal{U}^{\Lambda}$ on the rhs of eq.(3.10) by its initial value (App2). In both approximations the numerical effort is reduced considerably, since $\mathcal{U}^{\Lambda}$ has to be calculated on a two dimensional frequency mesh only. It will turn out that both approximations schemes are not capable of producing very accurate data. Therefore another scheme shall be introduced here. The starting point are the full fRG flow equations. Studying eq.(3.19), it is obvious that in 2PTh $\mathcal{U}^{\Lambda}$ can be written as a sum of three parts namely

$$\mathcal{U}^{\Lambda}(i\omega_1', i\omega_2'; i\omega_1, i\omega_2) = \mathcal{U}_1^{\Lambda}(i\omega_1' + i\omega_2') + \mathcal{U}_2^{\Lambda}(i\omega_1' - i\omega_1) + \mathcal{U}_3^{\Lambda}(i\omega_2' + i\omega_1).$$

Using this representation on the rhs of eq.(3.10) and determining $\mathcal{U}_1^{\Lambda}$ only from the first term on the rhs of eq.(3.10), $\mathcal{U}_2^{\Lambda}$ only from the second and $\mathcal{U}_3^{\Lambda}$ only from the third term, one arrives at an approximation scheme that conserves most features of fRG (App3). It
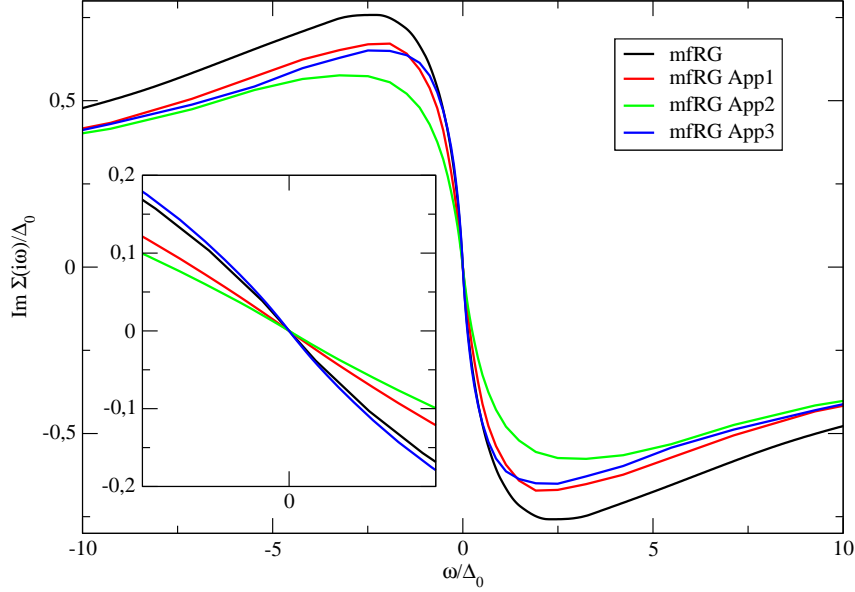
Figure 3.19: The imaginary part of the self-energy calculated with different approximation schemes for $U/\Delta_0 = 5$. The inset shows the low-energy region.

is important to use only one term from the rhs of eq.(3.10) for each $\mathcal{U}_i$ since constant contributions will otherwise lead to divergences. A more detailed description of the technical details, that lead to this approximation, is given in appendix B. In the schemes App2 and App3 it is possible to use the modified propagator $\mathcal{P}_{mod}^\Lambda$. Like in the full fRG scheme this leads to an improvement of the results. In this section all results presented have been calculated using the modified propagator.

To analyze these three schemes, the symmetric case will be considered first. Fig.(3.19) shows the results for $U/\Delta_0 = 5$. A surprising thing is that the three approximation schemes do not lead to results between 2PTh and fRG as on could expect from their construction. All three schemes show a qualitative agreement with full fRG. Quantitatively App2 is the worst one while App1 and App3 are comparably close to the full fRG curve. The picture changes when the low energy part is examined. Here App1 and App2 completely fail to reproduce the result from full fRG while App3 is in excellent agreement with it. For $U/\Delta_0 = 10$ these impressions are validated. Especially the fact that App2 produces the worst curve is confirmed. In the low energy region only App3 can be used to obtain good results.

One question that arises when looking at the self-energy in fig.(3.20) is, what consequences the difference between the full fRG and the approximate version has on the real
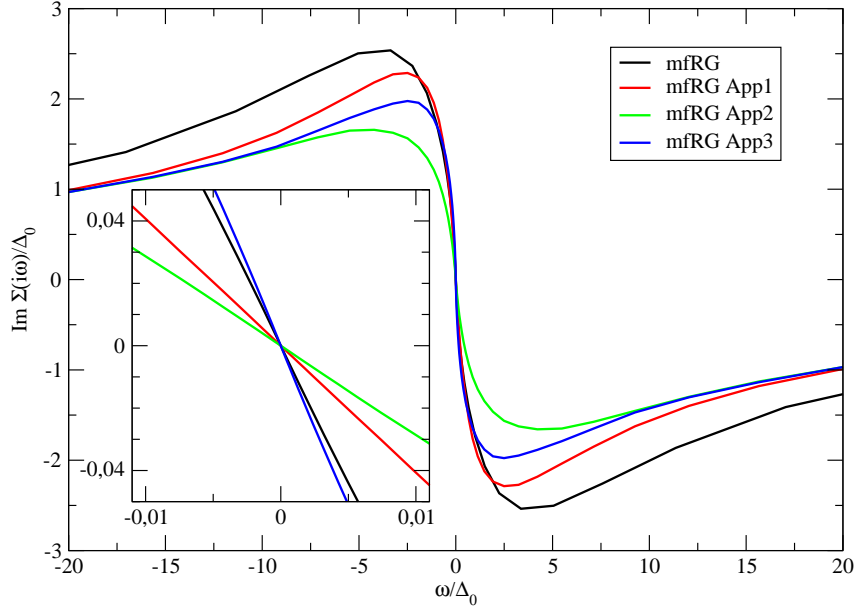
Figure 3.20: The imaginary part of the self-energy calculated with different approximation schemes for $U/\Delta_0 = 10$. The inset shows the low-energy region.

axis. It is to be expected that the Kondo resonance remains more or less unchanged, since this feature is strongly coupled to the low energy behaviour on the imaginary axis. Fig.(3.21) shows spectral functions for $U/\Delta_0 = 5$ and $U/\Delta_0 = 10$ obtained from full fRG, from App3 and from NRG. For $U/\Delta_0 = 5$ all three curves are very similar. For this interaction strength the approximate scheme can be used as well as the full fRG.
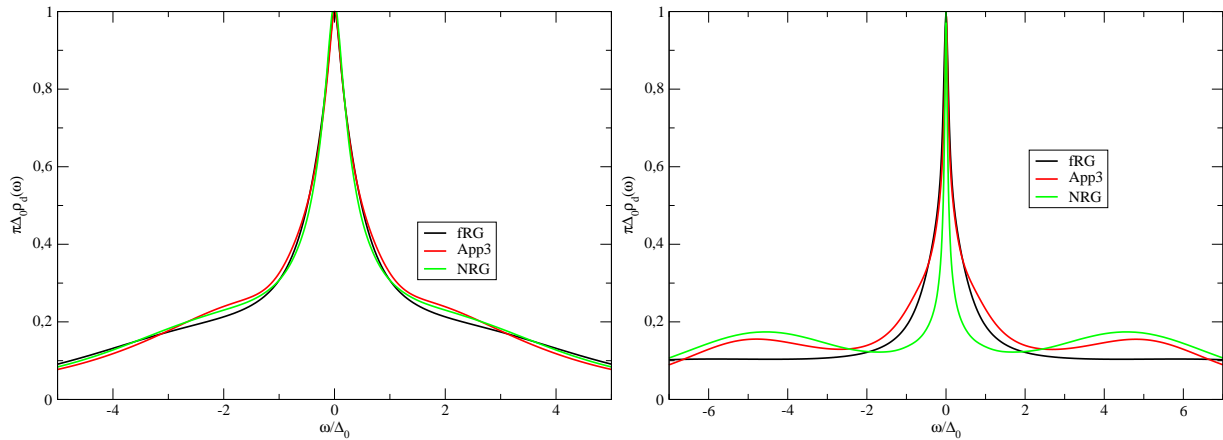

Figure 3.21: Spectral functions for $U/\Delta_0 = 5$ (left) and $U/\Delta_0 = 10$ (right) calculated with full mfRG and App3.
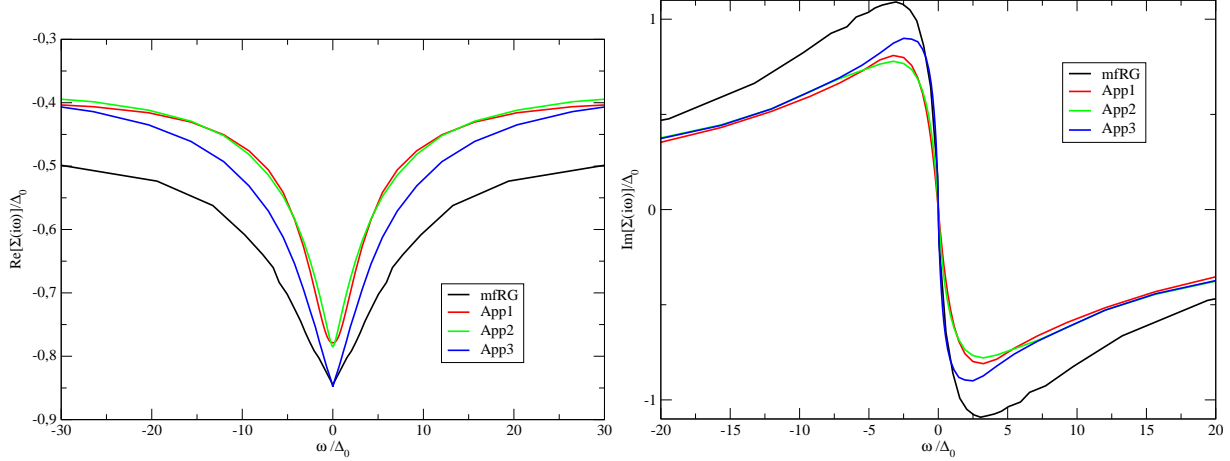
Figure 3.22: Self-energy from fRG, NRG and the different approximation schemes for $U/\Delta_0 = 2\pi$, $\epsilon_d = -U/2 + \Delta_0$.

For $U/\Delta_0 = 10$ there is an observable difference between the curves. The discrepancy between fRG and NRG has already been discussed earlier. Like one could expect from the low energy behaviour of the self-energy, the Kondo resonances from full fRG and from App3 are very similar, while at higher energies discrepancies become apparent. App3 shows a quicker broadening at the basis of the resonance and the atomic peaks are closer to the ones from NRG. One can trace the broader basis to the scheme itself. The atomic peaks in the spectral function of App3 are only visible if the frequency mesh used for the integration of the flow equation is interpolated with very much effort. Since the overall numerical effort for App3 is much lower than for the full fRG, this can easily be done here. For this reason it is not clear whether the difference in the atomic peaks is due to the scheme. For values of U/Δ_0, where the atomic peaks are not yet well separated from the resonance in the center, this does not have a major impact. For larger U it should be kept in mind that the self-energy determined from the approximate scheme is less reliable than the one obtained with the full fRG, although this might not have a major impact on the spectral functions.

When examining the asymmetric case, one has to differentiate between the frequency dependence in both, imaginary and real part, and the constant shift of the real part. As fig.(3.22) shows for $U/\Delta_0 = 2\pi$ and $\epsilon_d = -U/2 + \Delta_0$, all three approximations are quite close to the full fRG, i.e. they are capable of describing the constant shift much better than 2PTh. The accuracy of the frequency dependence of App2 and App3 is as good as in the symmetric case while App1 is worse than in the symmetric case. As the asymmetry
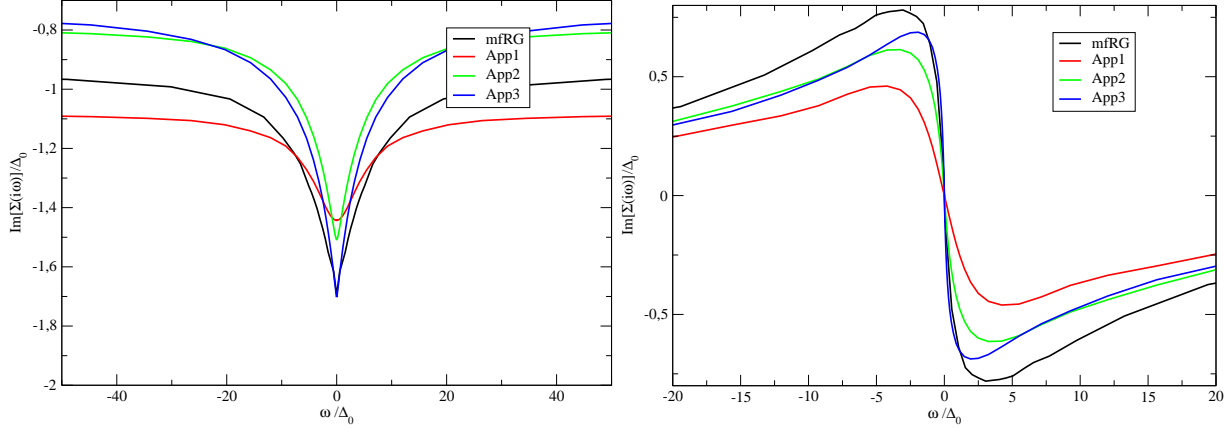
Figure 3.23: Self-energy from fRG, NRG and the different approximation schemes for $U/\Delta_0 = 2\pi$, $\epsilon_d = -U/2 + 2\Delta_0$

rises, these observations are confirmed. Fig.(3.23) shows the results for $U/\Delta_0 = 2\pi$ and $\epsilon_d = -U/2+2\Delta_0$. App3 is still very well describing the constant shift in the real part. The frequency dependence is as good as before. The accuracy of App2 and App1 is getting worse. App2 is describing the frequency dependence more accurately than App1 and the shift of the real part as calculated with App1 differs significantly from the others.

Over all these results are not very surprising. While App1 is quite close to 2PTh and gains from the knowingly good results of 2PTh in the symmetric case, it fails rather quickly in the asymmetric case. App2 takes into account all self-energy corrections and it therefore shows the same stability towards a shift in ϵ_d as the full fRG, but replacing the $\mathcal{U}^\Lambda$ by a constant on the rhs of eq.(3.10) is not suitable to give an accurate description of the frequency dependence. Only App3 is an approximation scheme that is worth using. While being not as accurate as full fRG on the imaginary axis, it reproduces the low energy behaviour excellently and like full fRG it is usable in the symmetric as well as in the asymmetric case. Additionally the reduced overall numerical effort allows to spend much effort on the interpolation of the frequency mesh and on the integration of the flow equations. For this reason it can be preferable to use this scheme, especially in more complex systems.

3.7 Summary

In this chapter the results from fRG calculations for the self-energy, the spectral functions, the occupancy of the impurity level and the static spin susceptibility have been compared to NRG, which is known to produce very accurate results for the Single Impurity Anderson Model, and to 2PTh, which is contained in fRG in the sense, that fRG with $m_c = 2$ is exact up to second order in the bare interaction. The fRG has been found to lead to reliable results for not too large interaction strengths. While 2PTh only works well in the special case of particle-hole symmetry, fRG does not suffer from such a drawback. Especially in the non-symmetric case it provides a clear improvement compared to 2PTh. The fact that in the symmetric case improvements can only be observed in the low-energy region is not due to a problem of fRG but to the fact that 2PTh works particularly well in this case, even for larger U. The fRG is simply not gaining anything from turning to particle-hole symmetry. Two versions of fRG results were presented, the conventional scheme and a modified scheme. For small U both schemes give practically identical results. If the interaction strength grows to regions of $U/\Delta_0 > 3$, the modified scheme has to be used to obtain accurate results. From $U/\Delta_0 \approx 7$ on the conventional scheme cannot be used to produce any results anymore due to divergences in the integration flow. This is the same parameter region where the results from the modified scheme start to differ from the exact ones. The comparison of results from the conventional scheme and from the modified scheme could give a hint for the quality of the results when treating systems where an exact solution is not at hand for comparison. It was pointed out that fRG can be used to calculate dynamical properties like the self-energy and the Green function as well as static observables like the impurity occupancy number and the static spin susceptibility. Including frequency dependence was confirmed to be important to get accurate results for small and intermediate bare interactions, while other schemes are preferable when aiming at exponential behaviour in the strong coupling regime.

Finally different approximations to the full fRG scheme were discussed. It was pointed out that for sensible frequency dependent results for the self-energy, the frequency dependency of the two-particle vertex has to be taken seriously and cannot even be neglected in the flow equation for $\mathcal{U}^\Lambda$. One approximation was presented, that reproduces the full fRG to a large degree and that is especially capable of describing the low-energy behaviour rather well.

Chapter 4

Two Impurities Anderson Model

The two impurities Anderson model describes two impurities, coupled to the same metallic host. If the position of the impurity α is given by $\vec{R}_\alpha$, $\alpha = 1, 2$ the Hamiltonian of this system is

$$H = \sum_{\vec{k},\sigma} \epsilon_{\vec{k}} c^\dagger_{\vec{k}\sigma} c_{\vec{k}\sigma} + V \sum_{\alpha,\vec{k},\sigma} e^{i\vec{k}\vec{R}_\alpha} \left(c^\dagger_{\vec{k}\sigma} d_{\alpha,\sigma} + \text{h.c.} \right)$$

$$+ \epsilon_d \sum_{\alpha,\sigma} d^\dagger_{\alpha,\sigma} d_{\alpha,\sigma} + U \sum_\alpha d^\dagger_{\alpha,\uparrow} d_{\alpha,\uparrow} d^\dagger_{\alpha,\downarrow} d_{\alpha,\downarrow} \ . \tag{4.1}$$

Compared to the SIAM (eq.(3.7)) the Hamiltonian has changed only in so far that the impurity operators have obtained an additional index α that can take the values $\alpha = 1, 2$ representing the two impurities. Although the Coulomb interaction is restricted locally and a direct exchange between the two impurities is not present, an indirect coupling via the conduction band electrons leads to new interesting physics compared to the single impurity case. Heuristically there is a competition between two effects. On one side
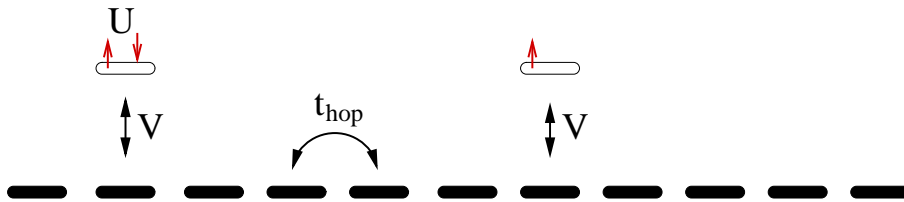

Figure 4.1: Two impurity sites coupled to a 1d chain.

the two impurities are screened individually by the band electrons so that each impurity behaves like a single impurity as described in the previous chapter. On the other side the interaction mediated by the conduction band electrons, the so-called Rudermann-Kittel-Kasuya-Yosida (RKKY) interaction, leads to a coupling of the two impurity spins. In general both, a ferromagnetic and an antiferromagnetic coupling, are possible. Which of the two is present in the system under investigation depends on details of the coupling, i.e. the electronic host and the position of the impurities. It seems obvious that for small inter-impurity distances the RKKY interaction should be dominant. With a growing distance between the impurities the coupling should get weaker and at large distances the individual screening of each impurity should be dominant. What distance is small or large in this context is of course depending on the other parameters of the system especially the bare interaction U and the single impurity Kondo temperature T_K. Due to the spatial extension of the screening cloud it is not clear whether a complete individual screening can take place at a finite distance at all. It will turn out that the behaviour of the system is largely dependent on the choice of the electronic host. In this chapter two different hosts will be studied. The first host will be a linear tight-binding chain, which is a typical 1d system. Free electrons in three dimensions will be the second electronic host. The impurity level will be set to $\epsilon_d = -U/2$ throughout this chapter.

The problem of two magnetic impurities coupled to a metallic host has been studied in various publications in the past. Refs. [36]-[53] have closely investigated the TIAM using various methods. Using the fRG, it is possible to reliably calculate the single particle dynamics of different variants of the TIAM within the same framework. It is possible to use a microscopic model like the linear chain as electronic host as well as a free electron gas. Additionally the two impurities Kondo model (TIKM) has been studied in numerous publications as well [55]-[61].

If the interaction strength U is much larger than the bandwidth of the electronic host, the behaviour of a system with two Anderson impurities can accurately be described by a TIKM [55], like in the one impurity case. A generalized Schrieffer-Wolff transformation that connects the TIAM to the Kondo model was presented in 2006 [54]. Like the TIAM in eq.(4.1), the TIKM does not contain any terms directly coupling the two impurities. A perturbative treatment in the coupling J between the impurity spins and the electronic host gives rise to a term

$$J_{RKKY} \vec{S}_1 \cdot \vec{S}_2 \tag{4.2}$$

in second order in J. The behaviour of the TIKM is determined by two parameters: the single impurity Kondo temperature T_K and the effective RKKY coupling J_{RKKY}. The RKKY coupling can be both ferromagnetic or antiferromagnetic. For large antiferromagnetic J_{RKKY}, the system is in a spin singlet state. If J_{RKKY}/T_k is small, the system displays a normal Kondo effect that becomes a correlated Kondo effect when a growing ferromagnetic J_{RKKY} leads to a spin triplet state. In [59] Jones and Varma find a critical point between the Kondo and the spin singlet phase. The existence of this critical point has been discussed controversially, because others like Fye and Hirsch did not find this critical point in their finite temperature Monte Carlo calculations [55]. NRG calculations on the related Anderson model by Sakai et al. did not display this critical point either [41]. In [61] Affleck et al. solved this discrepancy by field theoretical methods. They conclude that two different kinds of particle hole symmetry can be found in models with two magnetic impurities. Either the even and odd parity orbitals (explained further down) are both particle-hole symmetric ($\rho_{even/odd}(\omega) = \rho_{even/odd}(-\omega)$) or only obey $\rho_{even}(\omega) = \rho_{odd}(-\omega)$ resulting in a particle-hole symmetric total spectral function as well. A critical point only exists in the first case. Both, the TIKM studied by Fye and Hirsch and the TIAM, will usually not have the kind of particle hole symmetry that is necessary for the existence of such a critical point. These systems show a cross-over from the spin-singlet to the Kondo phase.

The dynamics of the TIAM, namely the spectral density, has been calculated with perturbative methods [46],[49], with NRG [41] and recently with the dynamical Density Matrix Renormalization Group (DDMRG) [53]. Still all these methods have their problems. Perturbation theory can be used to obtain an accurate picture of the dynamics in certain limiting cases but is not universally applicable. In the previous chapter these limitations have been discussed for the single impurity case. NRG provides very accurate low energy results but is less precise at larger energies. Furthermore the standard implementation loses precision at small interaction strengths. DDMRG results have been only presented in the limit of vanishing inter-impurity distance. In this chapter the single particle dynamics of the TIAM obtained from fRG will be studied. In particular their dependence on the inter-impurity distance and the consequences of the competition between Kondo effect and RKKY interaction for the spectral function will be studied.

Throughout this chapter the two impurities will be equivalent (ϵ_d, U and V in eq.(4.1) do not depend on the impurity index α). All quantities, like the free propagator $\mathcal{G}^0$, the full propagator $\mathcal{G}$, the self-energy Σ and the hybridization matrix Γ, now have a diagonal

part and an off-diagonal part. Using a matrix representation, the free propagator is now given by

$$\mathcal{G}^0(i\omega) = \begin{pmatrix} i\omega - \epsilon_d - \Gamma_{1,1} & -\Gamma_{1,2} \\ -\Gamma_{1,2} & i\omega - \epsilon_d - \Gamma_{1,1} \end{pmatrix}^{-1}, \tag{4.3}$$

with the hybridization matrix Γ being given by the conduction band's Green function

$$\Gamma_{\alpha,\beta} = V^2 \mathcal{G}_c^0(i\omega, |\vec{R}_\alpha - \vec{R}_\beta|) = V^2 \mathcal{G}_c^0(i\omega, R) . \tag{4.4}$$

The full propagator is obtained from the free propagator by replacing $\Gamma_{i,j}$ with $\Gamma_{i,j} + \Sigma_{i,j}$. In the case of two impurities it is helpful to switch from a description using diagonal and off-diagonal quantities to one, using states of even and odd parity with respect to the exchange of impurity numbers. The creation/annihilation operators of these states are given by

$$d^{(\dagger)}_{even/odd} = \frac{1}{\sqrt{2}}(d_1^{(\dagger)} \pm d_2^{(\dagger)}). \tag{4.5}$$

The corresponding hybridization matrix reads

$$\Gamma_{even/odd} = \Gamma_{1,1} \pm \Gamma_{1,2} \tag{4.6}$$

and the Green function for even/odd states is given by

$$\mathcal{G}_{even/odd}(z) = \frac{1}{z - \epsilon_d - \Gamma_{even/odd}} \tag{4.7}$$

or expressed by the matrix elements of the original Green function

$$\mathcal{G}_{even/odd}(z) = \frac{1}{2}\left(\mathcal{G}_{1,1}(z) \pm \mathcal{G}_{1,2}(z)\right). \tag{4.8}$$

The spectral function for the even and odd states can be calculated in the same way, since it is given by the imaginary part of the propagator. The details of the dynamics depend largely on the details of the hybridization matrix. In particular the influence of the inter-impurity distance depends rather strongly on the off-diagonal part of the hybridization matrix and thereby on the specific electronic host [41],[40]. Some general things about the spectral function at $U = 0$ of the TIAM can be said however. At $R = 0$ one obviously finds $\Gamma_{1,1} = \Gamma_{1,2} =: \Gamma$ which directly leads to $\Gamma_{even} = 2\Gamma$ and $\Gamma_{odd} = 0$. This results in a Lorentzian of width 2Γ in the even case and in a δ-peak in the odd case. The odd
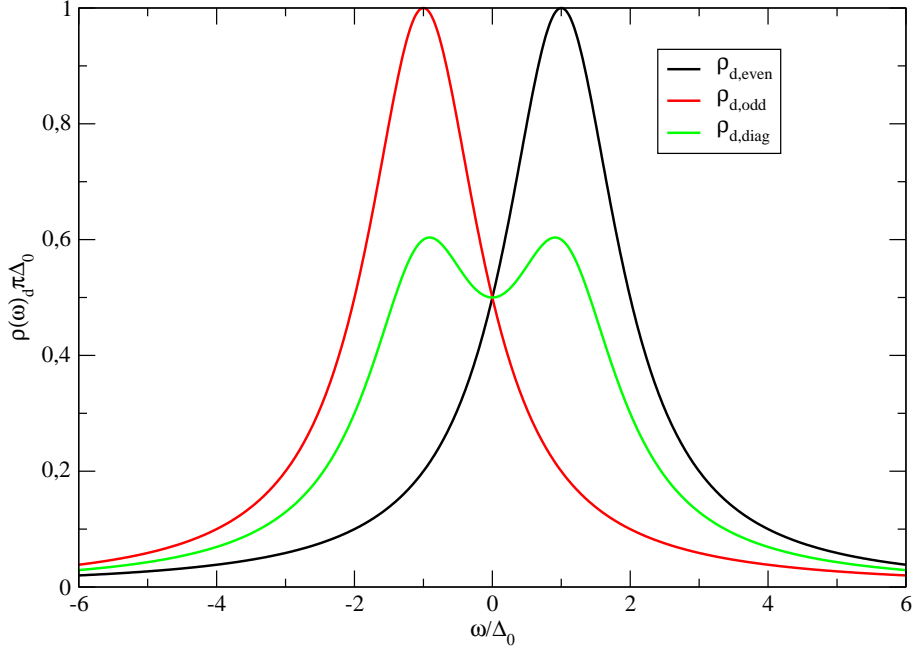
Figure 4.2: Typical spectral functions at $U = 0$ in a system with a finite $\text{Re}(\Gamma_{1,2})$.

parity states are decoupled from the rest of the system in this case and form a bound state. They are coupled to the system by the interaction which leads to a broadening of the sharp resonance. In the limit $R \to \infty$ it is expected that the hybridization between the impurities tends to 0. This results in $\Gamma_{even} = \Gamma_{odd} = \Gamma$. Both channels now behave like single Anderson impurities. These limits will be discussed in detail for the different electronic hosts. In general the off-diagonal part of the hybridization can be a complex function. In [40] Jones et al. point out that in particular the real part of this function is crucial for the dynamics of a two impurities system because it leads to a splitting of the central resonance in the diagonal part of the spectral function. This real part is added/subtracted to $\Gamma_{even/odd}$. This causes a shift of the impurity level in different directions. The peak of the even/odd spectral function is shifted in different directions, too. The diagonal part of the spectral function is the sum of the even/odd spectral function. A sufficiently large shift in the even/odd channel leads to a splitting of the central resonance. This situation is shown in fig.(4.2). A smaller shift will only result in a suppression of the resonance, while there is still one maximum at $\omega = 0$. The imaginary part of $\Gamma_{1,2}$ determines the difference of the widths of the even and the odd resonance. The interaction can influence both, the shift of the resonance in the even and odd spectral

function and the width of both resonances. From the above analysis it follows that even if $\epsilon_d = -U/2$, the system will only be particle-hole symmetric if $\Gamma_{1,2}$ is either purely imaginary or purely real. If it is real, the even and the odd resonance are identical but shifted in opposite directions, so that the sum is symmetric again. If it is imaginary, both resonances are symmetric around $\omega = 0$ and therefore the sum is also symmetric.

4.1 Flow equations

The main difference between the SIAM and the TIAM with respect to the flow equations is that the multi-index k now contains an additional index $m = 1, 2$ to denote the two impurities. In the parametrization of the two particle vertex one has to take into account the indirect interaction between the different impurities. There are basically two different forms of indirect interaction. First, there is the interaction of one electron on one impurity and one on the other impurity. This is described by $\mathcal{M}_2^\Lambda$ and $\mathcal{M}_3^\Lambda$. Second, there is an indirect hopping starting with two electrons on one impurity and ending with both electrons on the other impurity, described by $\mathcal{M}_4^\Lambda$. The easiest way to parametrize a vertex with these interactions would be

$$
\begin{aligned}
\bar{\gamma}_2^\Lambda(\xi_1', \xi_2'; \xi_1, \xi_2) \\
= \delta_{m_1,m_1'} \delta_{m_2,m_2'} \delta_{m_1,m_2} \underbrace{\left(\delta_{\sigma_1,\sigma_1'} \delta_{\sigma_2,\sigma_2'}\, \mathcal{U}_1^\Lambda - \delta_{\sigma_1,\sigma_2'} \delta_{\sigma_2,\sigma_1'}\, \tilde{\mathcal{U}}_1^{\,\Lambda}\right)}_{\mathcal{M}_1^\Lambda} \\[2mm]
+ \delta_{m_1,m_1'} \delta_{m_2,m_2'} \delta_{m_1,\bar{m}_2} \underbrace{\delta_{\sigma_1,\sigma_1'} \delta_{\sigma_2,\sigma_2'}\, \mathcal{U}_2^\Lambda}_{\mathcal{M}_2^\Lambda} - \delta_{m_1,m_1'} \delta_{m_2,m_2'} \delta_{m_1,\bar{m}_2} \underbrace{\delta_{\sigma_1,\sigma_2'} \delta_{\sigma_2,\sigma_1'} \tilde{\mathcal{U}}_2^{\,\Lambda}}_{\mathcal{M}_3^\Lambda} \\[2mm]
+ \delta_{m_1,m_2} \delta_{m_1',m_2'} \delta_{m_1,\bar{m}_1'} \underbrace{\left(\delta_{\sigma_1,\sigma_1'} \delta_{\sigma_2,\sigma_2'}\, \mathcal{U}_4^\Lambda - \delta_{\sigma_1,\sigma_2'} \delta_{\sigma_2,\sigma_1'}\, \tilde{\mathcal{U}}_4^{\,\Lambda}\right)}_{\mathcal{M}_4^\Lambda} \; .
\end{aligned}
$$

This is not sufficient to be exact up to second order in the interaction strength. The interaction of electrons carrying opposite spin on different impurities has to be separated into a channel where each electron stays on its original impurity and one in which the electrons exchange their positions. If both electrons are on the same impurity, these two channels are indistinguishable in an antisymmetrized vertex. The two-particle vertex

taking this into account reads

$$\bar{\gamma}_2^\Lambda(\xi_1', \xi_2'; \xi_1, \xi_2)$$

$$= \delta_{m_1,m_1'}\delta_{m_2,m_2'}\delta_{m_1,m_2} \underbrace{(\delta_{\sigma_1,\sigma_1'}\delta_{\sigma_2,\sigma_2'}\,\mathcal{U}_1^\Lambda - \delta_{\sigma_1,\sigma_2'}\delta_{\sigma_2,\sigma_1'}\,\tilde{\mathcal{U}}_1^\Lambda)}_{\mathcal{M}_1^\Lambda}$$

$$+ \delta_{m_1,m_1'}\delta_{m_2,m_2'}\delta_{m_1,\bar{m}_2} \underbrace{(\delta_{\sigma_1,\sigma_1'}\delta_{\sigma_2,\sigma_2'}\,\mathcal{U}_2^\Lambda + \delta_{\sigma_1,\sigma_2'}\delta_{\sigma_2,\sigma_1'}\,\mathcal{U}_3^\Lambda)}_{\mathcal{M}_2^\Lambda}$$

$$- \delta_{m_1,m_1'}\delta_{m_2,m_2'}\delta_{m_1,\bar{m}_2} \underbrace{(\delta_{\sigma_1,\sigma_2'}\delta_{\sigma_2,\sigma_1'}\tilde{\mathcal{U}}_2^\Lambda + \delta_{\sigma_1,\sigma_1'}\delta_{\sigma_2,\sigma_2'}\tilde{\mathcal{U}}_3^\Lambda)}_{\mathcal{M}_3^\Lambda}$$

$$+ \delta_{m_1,m_2}\delta_{m_1',m_2'}\delta_{m_1,\bar{m}_1'} \underbrace{(\delta_{\sigma_1,\sigma_1'}\delta_{\sigma_2,\sigma_2'}\,\mathcal{U}_4^\Lambda - \delta_{\sigma_1,\sigma_2'}\delta_{\sigma_2,\sigma_1'}\,\tilde{\mathcal{U}}_4^\Lambda)}_{\mathcal{M}_4^\Lambda} ,$$

where

$$\mathcal{U}_i^\Lambda = \mathcal{U}_i^\Lambda(i\omega_1', i\omega_2'; i\omega_1, i\omega_2), \quad \tilde{\mathcal{U}}_i^\Lambda = \mathcal{U}_i^\Lambda(i\omega_2', i\omega_1'; i\omega_1, i\omega_2) . \tag{4.9}$$

Using this parametrization and performing the sum over the impurity indices in eq.(2.26), the flow-equations for the two-particle vertex are

$$\frac{d}{d\Lambda}\mathcal{M}_1^\Lambda = -\frac{1}{2\pi}\sum_{\sigma,\sigma'}\int_{-\infty}^{\infty}d\nu \quad \times \tag{4.10}$$

$$\left[\mathcal{P}_1^\Lambda(i\nu, i\nu + i\nu_1 + i\nu_2)\left(\mathcal{M}_1^\Lambda\mathcal{M}_1^\Lambda + \mathcal{M}_4^\Lambda\mathcal{M}_4^\Lambda\right)\right.$$

$$+ \mathcal{P}_2^\Lambda(i\nu, i\nu + i\nu_1 + i\nu_2)\left(\mathcal{M}_1^\Lambda\mathcal{M}_4^\Lambda + \mathcal{M}_4^\Lambda\mathcal{M}_1^\Lambda\right)$$

$$+ \left\{\mathcal{P}_1^\Lambda(i\nu, -i\nu_1 + i\nu_1' + i\nu)\left(\mathcal{M}_1^\Lambda\mathcal{M}_1^\Lambda + \mathcal{M}_2^\Lambda\mathcal{M}_2^\Lambda\right)\right.$$

$$+ \mathcal{P}_2^\Lambda(i\nu, -i\nu_1 + i\nu_1' + i\nu)\left(\mathcal{M}_1^\Lambda\mathcal{M}_2^\Lambda + \mathcal{M}_2^\Lambda\mathcal{M}_1^\Lambda\right)$$

$$\left.+ (1' \leftrightarrow 2'; 1 \leftrightarrow 2) - (1' \leftrightarrow 2') - (1 \leftrightarrow 2)\right\}\bigg] ,$$

$$\frac{d}{d\Lambda}\mathcal{M}_2^\Lambda = -\frac{1}{2\pi}\sum_{\sigma,\sigma'}\int_{-\infty}^{\infty}d\nu \quad \times \tag{4.11}$$

$$\Bigg[-\mathcal{P}_1^\Lambda(i\nu, i\nu + i\nu_1 + i\nu_2)\Big(\mathcal{M}_2^\Lambda\mathcal{M}_3^\Lambda + \mathcal{M}_3^\Lambda\mathcal{M}_2^\Lambda\Big)$$

$$+\mathcal{P}_2^\Lambda(i\nu, i\nu + i\nu_1 + i\nu_2)\Big(\mathcal{M}_2^\Lambda\mathcal{M}_2^\Lambda + \mathcal{M}_3^\Lambda\mathcal{M}_3^\Lambda\Big)$$

$$+\Big\{\mathcal{P}_1^\Lambda(i\nu, -i\nu_1 + i\nu_1' + i\nu)\Big(\mathcal{M}_1^\Lambda\mathcal{M}_2^\Lambda + \mathcal{M}_2^\Lambda\mathcal{M}_1^\Lambda\Big)$$

$$+\mathcal{P}_2^\Lambda(i\nu, -i\nu_1 + i\nu_1' + i\nu)\Big(\mathcal{M}_2^\Lambda\mathcal{M}_2^\Lambda + \mathcal{M}_1^\Lambda\mathcal{M}_1^\Lambda\Big)$$

$$+(1' \leftrightarrow 2'; 1 \leftrightarrow 2)\Big\}$$

$$-\Big\{\mathcal{P}_1^\Lambda(i\nu, -i\nu_2 + i\nu_1' + i\nu)\Big(\mathcal{M}_3^\Lambda\mathcal{M}_3^\Lambda + \mathcal{M}_4^\Lambda\mathcal{M}_4^\Lambda\Big)$$

$$+\mathcal{P}_2^\Lambda(i\nu, -i\nu_2 + i\nu_1' + i\nu)\Big(\mathcal{M}_3^\Lambda\mathcal{M}_4^\Lambda + \mathcal{M}_4^\Lambda\mathcal{M}_3^\Lambda\Big)$$

$$+(1' \leftrightarrow 2'; 1 \leftrightarrow 2)\Big\}\Bigg]$$

and

$$\frac{d}{d\Lambda}\mathcal{M}_4^\Lambda = -\frac{1}{2\pi}\sum_{\sigma,\sigma'}\int_{-\infty}^{\infty}d\nu \quad \times \tag{4.12}$$

$$\Bigg[\mathcal{P}_1^\Lambda(i\nu, i\nu + i\nu_1 + i\nu_2)\Big(\mathcal{M}_1^\Lambda\mathcal{M}_4^\Lambda + \mathcal{M}_4^\Lambda\mathcal{M}_1^\Lambda\Big)$$

$$+\mathcal{P}_2^\Lambda(i\nu, i\nu + i\nu_1 + i\nu_2)\Big(\mathcal{M}_1^\Lambda\mathcal{M}_1^\Lambda + \mathcal{M}_4^\Lambda\mathcal{M}_4^\Lambda\Big)$$

$$+\Big\{-\mathcal{P}_1^\Lambda(i\nu, -i\nu_1 + i\nu_1' + i\nu)\Big(\mathcal{M}_3^\Lambda\mathcal{M}_4^\Lambda + \mathcal{M}_4^\Lambda\mathcal{M}_3^\Lambda\Big)$$

$$+\mathcal{P}_2^\Lambda(i\nu, -i\nu_1 + i\nu_1' + i\nu)\Big(\mathcal{M}_3^\Lambda\mathcal{M}_3^\Lambda + \mathcal{M}_4^\Lambda\mathcal{M}_4^\Lambda\Big)$$

$$+(1' \leftrightarrow 2'; 1 \leftrightarrow 2) - (1' \leftrightarrow 2') - (1 \leftrightarrow 2)\Big\}\Bigg] \,,$$

where $\mathcal{M}_i$ are frequency and spin dependent functions as defined in eq.(4.9). For $\mathcal{M}_3^\Lambda$ no flow equation is needed since the frequency dependent functions $\mathcal{U}_2^\Lambda$ and $\mathcal{U}_3^\Lambda$ can be determined from $\mathcal{M}_2^\Lambda$. The remaining sum over the spin indices is performed in complete

analogy to the procedure in the one impurity case and the result is not shown here. Appendix C gives a more detailed derivation of the flow equation for $\mathcal{U}_1^\Lambda$ as an example. For the self-energy there is one flow equation for the diagonal part

$$\frac{d}{d\Lambda}\Sigma_\sigma^\Lambda(i\omega)_{diag} = -\frac{1}{2\pi}\sum_\omega \mathcal{S}_{1,1}^\Lambda(i\omega) \quad \times$$

$$\left[2\mathcal{U}_1^\Lambda(i\omega, i\alpha\Lambda; i\omega, i\alpha\Lambda) - \mathcal{U}_1^\Lambda(i\alpha\Lambda, i\omega; i\omega, i\alpha\Lambda)\right. \tag{4.13}$$

$$\left.+2\mathcal{U}_2^\Lambda(i\omega, i\alpha\Lambda; i\omega, i\alpha\Lambda) + \mathcal{U}_3^\Lambda(i\alpha\Lambda, i\omega; i\omega, i\alpha\Lambda)\right]$$

and one for the off-diagonal part

$$\frac{d}{d\Lambda}\Sigma_\sigma^\Lambda(i\omega)_{off} = -\frac{1}{2\pi}\sum_\omega \mathcal{S}_{1,2}^\Lambda(i\omega) \quad \times$$

$$\left[-2\mathcal{U}_3^\Lambda(i\omega, i\alpha\Lambda; i\omega, i\alpha\Lambda) - \mathcal{U}_2^\Lambda(i\alpha\Lambda, i\omega; i\omega, i\alpha\Lambda)\right. \tag{4.14}$$

$$\left.+2\mathcal{U}_4^\Lambda(i\omega, i\alpha\Lambda; i\omega, i\alpha\Lambda) - \mathcal{U}_4^\Lambda(i\alpha\Lambda, i\omega; i\omega, i\alpha\Lambda)\right] .$$

Again, these equations have to be integrated numerically using a suitable mesh of frequencies. The initial conditions for Σ^{Λ_0} and the $\mathcal{U}_i^{\Lambda_0}$ are given by

$$\Sigma_{diag}^{\Lambda_0} = \frac{U}{2}; \quad \Sigma_{off}^{\Lambda_0} = 0 \tag{4.15}$$

$$\mathcal{U}_1^{\Lambda_0} = U; \quad \mathcal{U}_2^{\Lambda_0} = \mathcal{U}_3^{\Lambda_0} = \mathcal{U}_4^{\Lambda_0} = 0. \tag{4.16}$$

In eq.(4.10) to eq.(4.12) the combined propagator $\mathcal{P}_i^\Lambda$ appears with an additional index $i = 1, 2$. This is due to the matrix structure of the propagators $\mathcal{G}^{0,\Lambda}$, $\mathcal{G}^\Lambda$ and $\mathcal{S}^\Lambda$. The combined propagators are given by

$$\mathcal{P}_{k,con}^\Lambda(i\nu, i\nu') = \mathcal{S}_{1,k}^\Lambda(i\nu)\mathcal{G}_{1,k}^\Lambda(i\nu') \tag{4.17}$$

and

$$\mathcal{P}_{k,mod}^\Lambda(i\nu, i\nu') = -\frac{d}{d\Lambda}\mathcal{G}_{1,k}^\Lambda(i\nu)\mathcal{G}_{1,k}^\Lambda(i\nu') . \tag{4.18}$$

These can be calculated in the same way as in the one impurity case, using eq.(3.12). Without looking at the explicit result of these calculations, it is immediately obvious, that from $\Gamma_{1,2} = 0$ it follows $\mathcal{P}_2 = 0$. This and the initial conditions eq.(4.15) directly lead to $\Sigma_{1,2} = \mathcal{U}_2 = \mathcal{U}_3 = \mathcal{U}_4 = 0$ leaving the flow equations for the single impurity case as presented in chapter 3.

Compared to the one impurity case, the numerical effort for the integration of the flow equations is increased roughly by a factor 8. This is due to the four frequency dependent functions in the parametrization of γ_2^Λ on the one side and the increased number of terms on the rhs of eq.(4.10) to eq.(4.12) compared to eq.(3.10).

In the case of two impurities it is interesting to analyse the behaviour of the ground state energy as function of the distance between the impurities R. In chapter 2 the general flow equation for the zero-particle vertex was presented in eq.(2.29). Here it takes the form

$$
\frac{d}{d\Lambda} \lim_{T\to 0} T\gamma_0^\Lambda = \frac{d}{d\Lambda} e_0^\Lambda = -\frac{1}{2\pi} \sum_{\alpha,\beta} \sum_{\omega=\pm\Lambda} \ln\left[1 - \mathcal{G}_{\alpha,\beta}^0(i\omega)\, \Sigma_{\beta,\alpha}^\Lambda(i\omega)\right] . \tag{4.19}
$$

This is only the interaction dependent part of the ground state energy. The ground state energy for the non-interacting case can be easily calculated from

$$
\langle H \rangle = \sum_{k\le k_F,\sigma} \epsilon_{k,\sigma} - \frac{1}{\pi}\mathrm{Im} \int_{-\infty}^{0} d\omega \left[(\omega + \epsilon_d + \Gamma_1 - 2\omega\Gamma_1')\mathcal{G}_1 + (\Gamma_2 - 2\omega\Gamma_2')\mathcal{G}_2\right] , \tag{4.20}
$$

where Γ' is the derivative of Γ with respect to ω and $\mathcal{G} = \mathcal{G}^0$ [32]. Although this formula could be used in the interacting case as well, it is preferable to use the flow-equation for e_0^Λ. Since the truncation of the fRG flow equation hierarchy is a non-conserving approximation, the use of a separate flow equation is formally the correct way to determine the value of γ_0. Additionally one can expect the approximation made by truncating the hierarchy to be the better the lower the order of the calculated vertex is. Truncating the hierarchy after the two-particle vertex should therefore give a better approximation for the zero-particle vertex than for the self-energy. Another reason for the use of the flow equation is that otherwise it would be necessary to use the analytic continuation of $\mathcal{G}(i\omega)$, which is numerically less reliable than the direct result from eq.(4.19).

Another observable, that is of great interest in the two impurity case, is the spin-spin correlation function $\langle \vec{S}_1 \cdot \vec{S}_2 \rangle$. This value characterizes the correlation between the two magnetic moments. From this value one can see whether the coupling between the mag-

netic moments is ferromagnetic or antiferromagnetic and how strong it is. The standard way to calculate this property from fRG would be to derive a separate flow equation like it has been done in chapter 2 for the occupation number $\langle n_d \rangle$ (eq.(2.31)).The comparison of different methods to calculate $\langle n_d \rangle$ showed, that this does not necessarily give the most accurate result. Therefore a different method will be used here. Using the Pauli spin matrices $\sigma^{x,y,z}$, the spin operator $S_i^{x,y,z}$ can be written as

$$S_i^{x,y,z} = \frac{1}{2}\sum_{a,b} d_{i,a}^\dagger \sigma_{a,b}^{x,y,z} d_{i,b}, \tag{4.21}$$

where i is the impurity index and a, b can be $\uparrow$ and $\downarrow$. Using this, the spin-spin correlation function can be expressed in terms of the $d^{(\dagger)}_i$:

$$\langle \vec{S}_1 \cdot \vec{S}_2 \rangle = \frac{1}{2}\left(\langle d_{1,\uparrow}^\dagger d_{1,\downarrow} d_{2,\downarrow}^\dagger d_{2,\uparrow} \rangle + \langle d_{1,\downarrow}^\dagger d_{1,\uparrow} d_{2,\uparrow}^\dagger d_{2,\downarrow} \rangle \right) + \frac{1}{4}\langle (\hat{n}_{1,\uparrow} - \hat{n}_{1,\downarrow})(\hat{n}_{2,\uparrow} - \hat{n}_{2,\downarrow}) \rangle . \tag{4.22}$$

Using the two-particle vertex function, the two-particle Green function can be calculated according to [17]:

$$
\begin{aligned}
\mathcal{G}_2(k_1', k_2'; k_1, k_2) &= \mathcal{G}(k_1'; k_1)\mathcal{G}(k_2'; k_2) - \mathcal{G}(k_1'; k_2)\mathcal{G}(k_2'; k_1) \\
&+ \sum_{q_1', q_2', q_1, q_2} \mathcal{G}(k_1'; q_1')\mathcal{G}(k_2'; q_2')\gamma_2(q_1', q_2'; q_1, q_2)\mathcal{G}(q_1; k_1)\mathcal{G}(q_2; k_2), \tag{4.23}
\end{aligned}
$$

where $k_i^{(')} = (m_i^{(')}, \sigma_i^{(')}, i\omega_i^{(')})$. Now the expectation values in eq.(4.22) can be calculated from the two-particle Green function in analogy to eq.(3.26). In the non-interacting case the expression reduces to

$$\langle \vec{S}_1 \cdot \vec{S}_2 \rangle_0 = -\frac{3}{32}(\langle n_{even} \rangle_0 - \langle n_{odd} \rangle_0)^2. \tag{4.24}$$

4.2   Results

Before turning to the results from fRG calculations for specific systems, the quality and the reliability of these results should be discussed briefly. Comparing the results to 2PTh and comparing the results from conventional and modified fRG, it turns out that in situations with an antiferromagnetic RKKY coupling between the impurities fRG is at least as good as in the one impurity case, i.e. interaction strengths up to $U/\Delta_0 = 10$ are

reliably treatable. Unfortunately a comparison to NRG is not possible, since NRG is not capable of producing reliable results for dynamical properties at small and intermediate interaction strengths. If the coupling between the impurities leads to a weak ferromagnetic correlation, the quality of fRG results is still comparable to the one impurity case. For strong ferromagnetic couplings, the effective on-site interaction grows very large during the integration of the flow equations. In these situations fRG is not capable of producing convincing results. Therefore no quantitative results are presented for such systems. All results shown in this chapter are obtained from the modified fRG scheme.

4.2.1 1d Tight-Binding Chain

The first electronic host studied will be a one-dimensional tight-binding chain of infinite length. The impurities are coupled to chain sites that have a distance R measured in chain sites. The Green function of this host can be calculated analytically. If the hopping between the chain sites is t, it reads

$$\mathcal{G}_c^0(i\omega, R) = \frac{-i\,\mathrm{sign}(\omega)}{\sqrt{w^2 + 4t^2}} \left[\frac{i\omega}{2t} - i\,\mathrm{sign}(\omega)\sqrt{\frac{\omega^2}{4t^2} + 1} \right]^R . \tag{4.25}$$

The corresponding bandwidth is $W = 4t$. Unless explicitly stated differently, t is set to $t = 1/2$. Note, that for imaginary frequencies no band-edge singularities appear. The hybridization between chain and impurities is set to $V = 0.1$ throughout this chapter. This leads to

$$\Delta_0 := -\mathrm{Im}\Gamma_{1,1}(0 + i0) = 0.01 , \tag{4.26}$$

which is much smaller than the bandwidth.

For real frequencies, $\omega + i0$ within the bandwidth $\mathcal{G}_c^0$ can be transformed to

$$\mathcal{G}_c^0(\omega + i0, R) = \frac{-i}{\sqrt{4t^2 - \omega^2}} e^{-ik(\omega)R}, \quad k(\omega) = \arccos\left(\frac{\omega}{2t}\right) . \tag{4.27}$$

For large R this function is heavily oscillating for small frequencies. These oscillations will be visible in the spectral function at large distances R as well. Looking at $\mathcal{G}_c^0$ in eq.(4.25), it becomes apparent, that there will be a strong even-odd effect in this system. For even R the hybridization $\Gamma_{1,2}$ will be imaginary, while for odd R it is real. The consequence of this behaviour becomes more obvious when looking at the states with an even and odd parity.
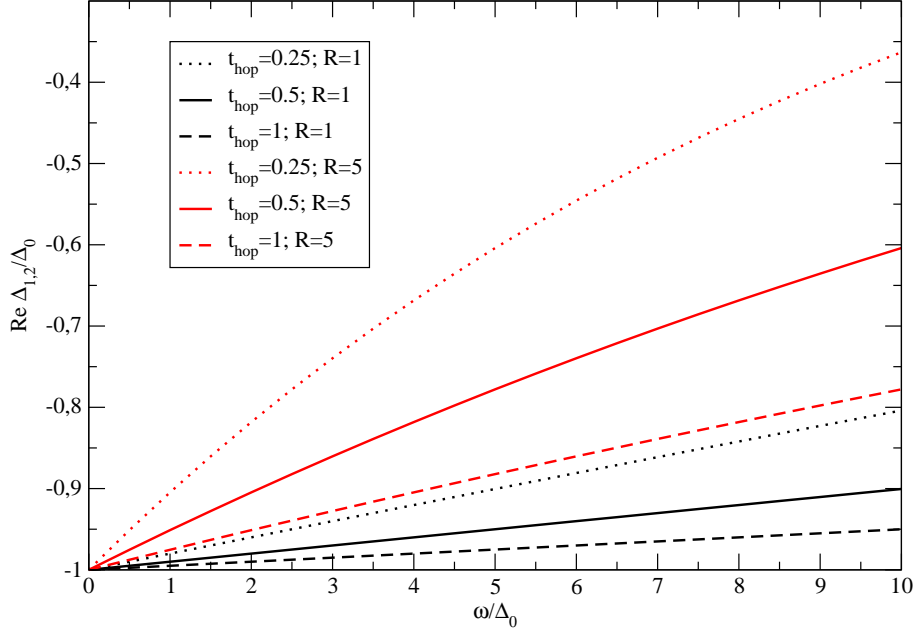
Figure 4.3: Off-diagonal part of the hybridization function for various t_{hop} and R.

An even R will result in $\Gamma_{odd}(0+i0) = 0$, which leads to a $\delta-$peak in the spectral function. Although this peak is broadened when turning on the interaction, a reminiscence of this peak remains for even R. Additionally the results from [55] suggest that for even R the impurities are coupled with a rather strong ferromagnetic RKKY interaction. For $R = 0$ this result is confirmed in [53]. As stated above, fRG is not capable of producing reliable results in this situation. Therefore the discussion here will be restricted to odd R. For odd R there is an oscillatory effect as well. The hybridization function changes its sign for neighbouring odd R. The impact of this effect is only a minor one. The change of sign in the off-diagonal part of the hybridization causes a change of sign in the off-diagonal part of the Green function. The result is that even and odd parity properties are exchanged. Especially the diagonal part of the spectral function remains unchanged.

The choice of $t_{hop} = 1/2$ might be considered a special case, but as long as the bandwidth $W = 4t$ of the linear chain is much larger than Δ_0, a changed t_{hop} only leads to a rescaling of the R-dependence of the results. The R-dependence is caused by the off-diagonal part of the hybridization function, which is shown in fig.(4.3). The diagonal part shows no relevant frequency dependence as long as $W \gg \Delta_0$. The reduction of t_{hop} for a given R has the same effect as the increase of R for a constant t_{hop}. The qualitative influence of the inter-impurity distance on the dynamics of the system does therefore not depend on
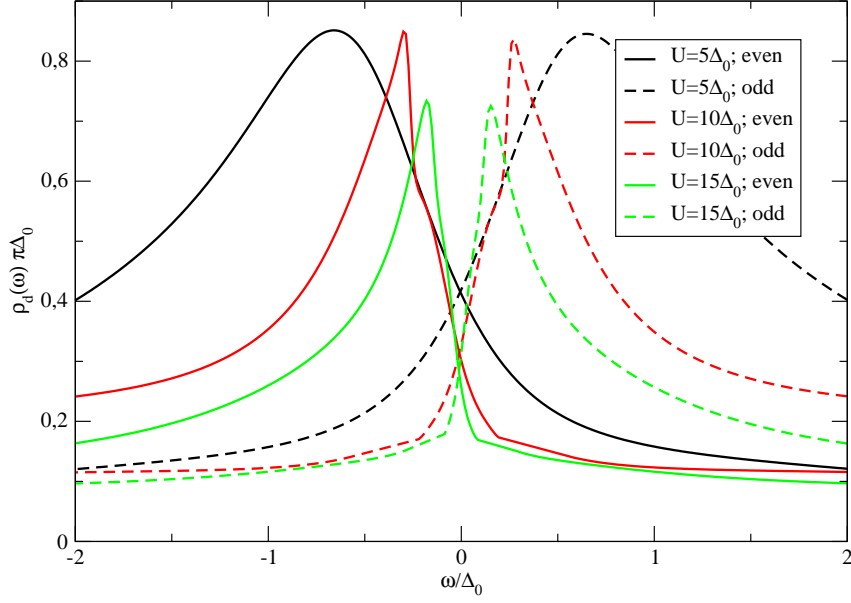
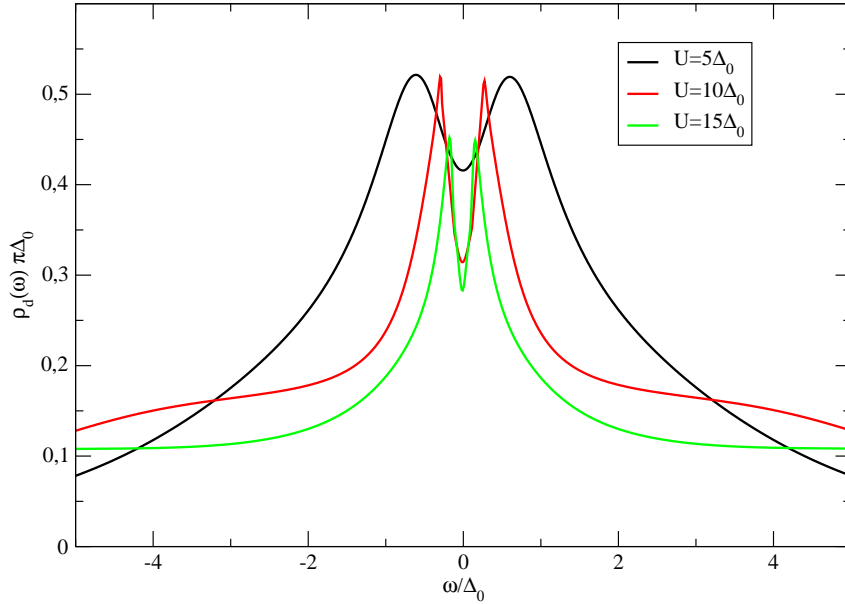Figure 4.4: Even and odd parity spectral functions for $R = 1$ and various U.

Figure 4.5: Diagonal part of the spectral function for $R = 1$ and various U.

the choice of t_{hop}. Only the quantitative dependence on the distance R is effected by a given t_{hop}. As in the one impurity case, the most basic question is how the one-particle dynamics depend on the interaction strength U/Δ_0. Fig.(4.4) shows the even and odd

parity spectral functions at $R = 1$ and for different interaction strengths. In the high energy region the behaviour is similar to the single impurity case. The dynamics are governed by the atomic peaks again. The peaks of the spectral functions are shifted away from the chemical potential resulting in a splitting of the central resonance in the total spectral function (fig.(4.5)). This behaviour is to be expected from NRG calculations by Sakai et al. on the same kind of system [41]. Obviously the position of the peaks depends strongly on the interaction strength. While for $U = 0$ the shift is exactly Δ_0 corresponding to the value of $\Gamma_{1,2}(0 + i0) = \Delta_0$, with growing interaction strength the shift of the even/odd parity peaks is getting smaller. The even and odd spectral functions show the same pinning effect that counteracts the shift of the Kondo resonance in the one impurity case if going away from $\epsilon_d = -U/2$. The reason for this behaviour is the competition between the inter-impurity coupling and the Kondo physics caused by the on-site interaction. Fig.(4.8) shows the spin-spin correlation function and the effective mass as a function of R. The values for $R = 1$ can be found there for different values of U. The correlation of the spins at $R = 1$ increases almost linearly with growing U. The plot for the effective mass only shows the effective mass relative to its single impurity value. Although this relative value is decreasing with growing U, the absolute value, which is relevant here, grows much faster than the spin correlations, since the single impurity value of the effective mass is increasing very fast with growing U. For this reason the level shift caused by the hybridization between the impurities is suppressed by the Kondo effect with growing interaction strength. Although an increase of the interaction strength causes a sharpening of the resonances in the even and odd channel as well as in the full spectral function, these resonances are much broader than in the single impurity case. The effective mass, that is inversely connected to the Kondo temperature and to the width of these resonances, is much smaller than the one from the corresponding SIAM. With growing U the relative effective mass is decreasing. This is caused by the growing spin-spin correlations (fig.(4.8)). Due to the RKKY interaction, $\langle \vec{S}_1 \cdot \vec{S}_2 \rangle$ is getting stronger with growing U and the effect on the two impurity system relative to the corresponding single impurity system is getting stronger, too.

For much larger interaction strengths, fRG data is getting less reliable. An accurate calculation of the shift in the even/odd spectral function for values $U/\Delta_0 > 20$ is not possible. To answer the question whether the splitting of the central resonance will vanish for any finite U, another observation is useful. With growing interaction strength the value of the spectral function is decreasing. The increasing spin-spin correlations cause a

growing suppression of the Kondo resonance. Although fRG is not capable of producing quantitatively accurate data for very large U, it is obvious that the spectral weight at the chemical potential is decreased. The conclusion is that with growing interaction strength the splitting of the central resonance is getting arbitrarily small while at the same time the spectral weight at the chemical potential is more and more suppressed. In ref.[52] the same result was found using perturbation theory. Only in the limit $U \to \infty$ the gap will close.

Summarizing, one can say that the antiferromagentic RKKY coupling has a grave impact on the low energy behaviour in this system. With an increased interaction strength the correlation of the spins is increased as well and the effect relative to a single impurity system is growing. This correlation suppresses the fluctuations that lead to the Kondo resonance in the one impurity case. The splitting of the Kondo resonance is existant for all finite interaction strengths. While the suppression of the Kondo resonance is increased with growing interaction strength, i.e. with growing correlation of the impurity spins, the shift in the even and odd spectral function leading to the splitting is decreased.

Besides the interaction strength U, the other parameter in this models that directly influences the multi-impurity character of the system is the distance between the impurities R. This influence will now be further investigated, especially aiming at the question, whether for a finite value of R the system shows a cross-over from a state with antiferromagnetically correlated spins to a state, where both impurities are individually screened like in the one impurity case. The even and odd spectral functions for $U/\Delta_0 = 5$ and
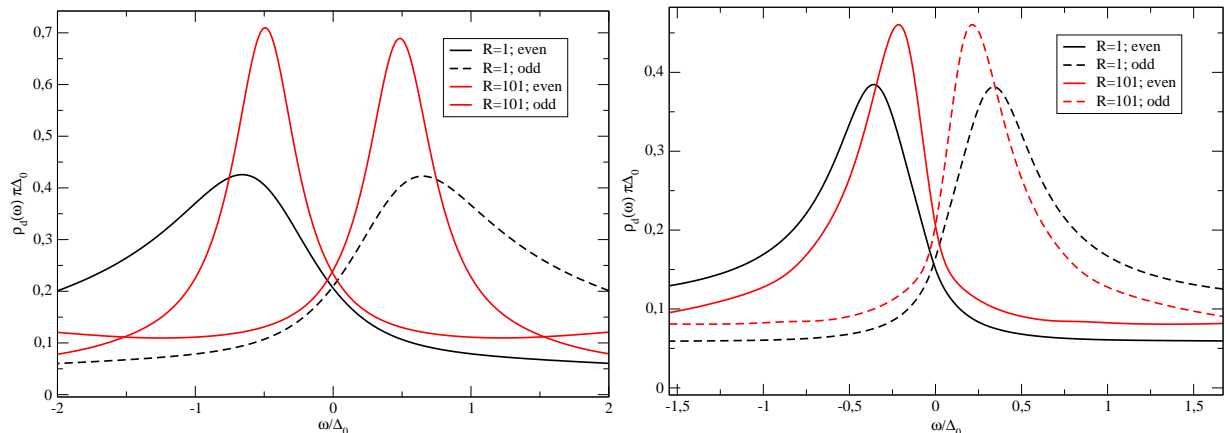

Figure 4.6: Even and odd parity spectral functions for different values of R; left: $U/\Delta_0 = 5$; right: $U/\Delta_0 = 10$.
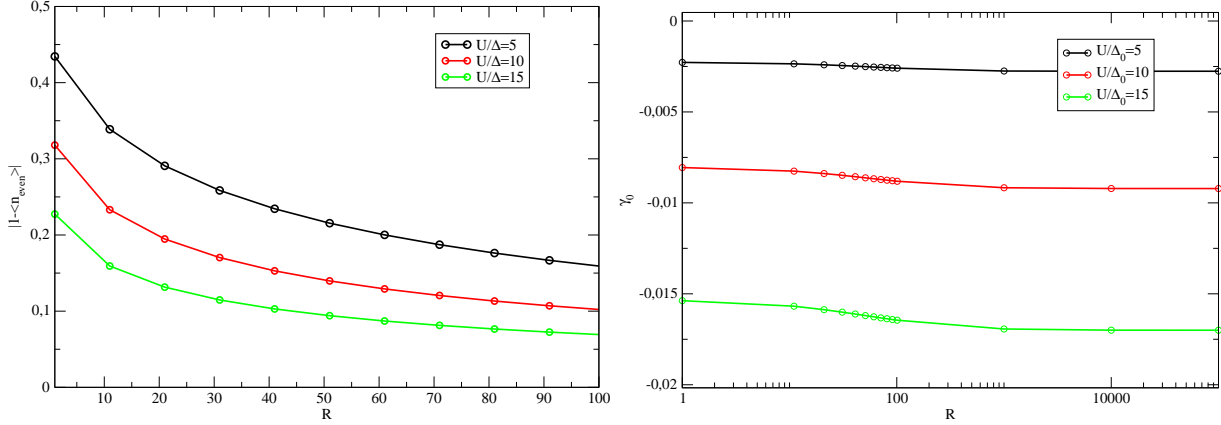
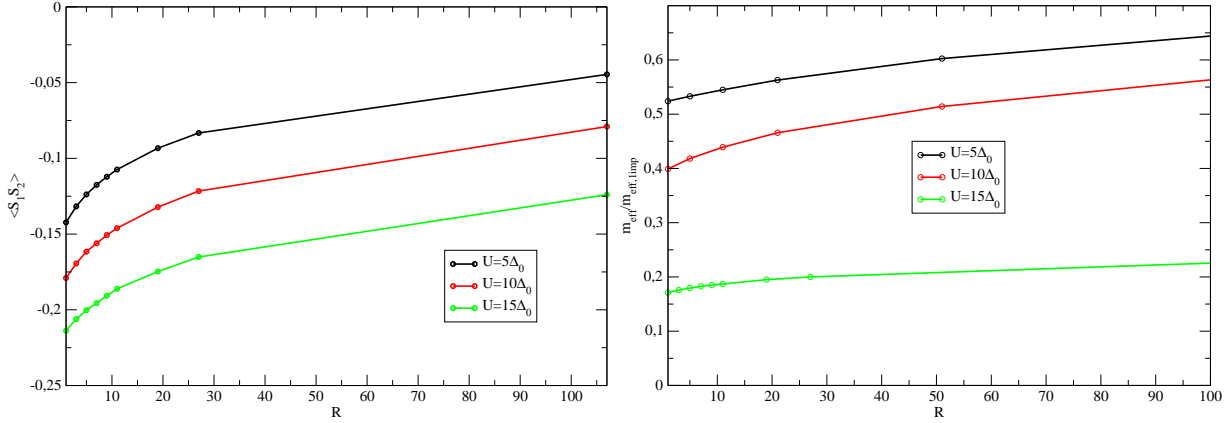Figure 4.7: Left: deviation of $\langle n_{even} \rangle$ from 1; right: ground state energy; both as a function of R.

Figure 4.8: Spin-spin correlation function (left) and effective mass relative to the single impurity value (right) as a function of R.

$U/\Delta_0 = 10$ are shown in fig.(4.6) for different values of R. Two things are to be observed for both interaction strengths. The resonances in the even and the odd channel are getting higher and slightly sharper and the shift of the resonances away from the chemical potential is decreasing with an increasing inter-impurity distance R. Although the resonance shift is getting smaller, its dependence on the inter-impurity distance is rather weak. This impression is confirmed by the occupation number of the states with even parity. Without a resonance shift, this quantity would be $\langle \hat{n}_{even} \rangle = 1$. The deviation from this value can be serve as a measurement for a resonance shift. The left panel of fig.(4.7) confirms this observation. The occupancy of the even states is approaching 1 but
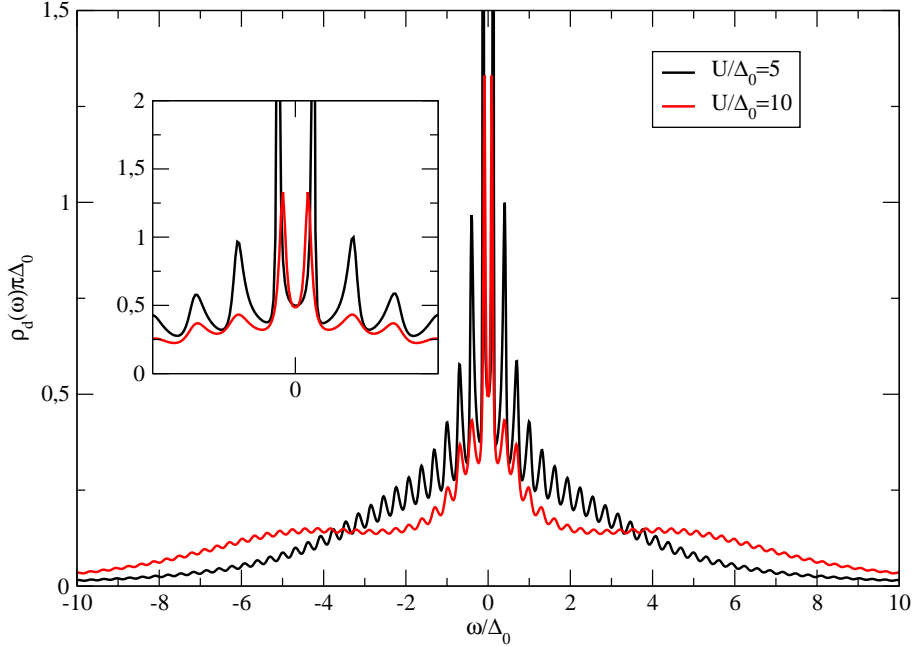
Figure 4.9: Spectral functions for $R = 1000$; $U/\Delta_0 = 5$ and $U/\Delta_0 = 10$.

the process is rather slow. The smaller deviation from 1 for larger interaction strength is caused by the smaller shift of the even and odd parity resonance as it was discussed above. Fig.(4.8) shows the spin-spin correlation function and the effective mass as a function of R for different interaction strengths. The correlation of the impurity spins is decaying slowly as the suppression of the central resonance is getting weaker. At the same time the effective mass is slowly approaching the single impurity value as the resonances are getting sharper. The interaction strength U has no great influence on the R-dependence of the dynamics.

For very large distances the quantities shown approach their single impurity value. The ground state energy shown in the right panel of fig.(4.7) clearly shows a saturation for $R > 1000$. The spectral functions for $R = 1000$ are shown in fig.(4.9). In addition to the interaction caused effects, the hybridization causes an oscillatory behaviour here. Near the chemical potential two peaks can be observed but their position, as well the position of all other extrema, does not depend on the interaction strength. Their distance corresponds to the frequency of the $e^{ik(w)R}$ term in eq.(4.27).

Overall, the dependence of the dynamics of two impurities coupled to a 1d tight-binding chain on the inter-impurity distance is rather weak. A clear cross-over from a state with an antiferromagnetic correlation between the impurity spins and a state with two individ-

ual Anderson impurities is not observable. The properties of the system approach their single impurity values as the inter-impurity correlations are decaying, but this process is extremely slow. This results from the specific form of the hybridization function. The R-dependence is only given by a faster decay at large frequencies. The strength of the hybridization at $\omega = 0$ is independent of R. This causes visible effects for all finite R since the inter-impurity hybridization will always be as strong as the on-site interaction around $\omega = 0$. The hybridization function in the next section will behave differently. This will result in a completely different R-dependence of the single particle dynamics.

4.2.2 Free Electron Gas

To show the dependence of the TIAM's properties on the electronic host, now a three-dimensional free electron gas is used. With such an electronic host, the TIAM can be used to describe magnetic atoms in a bulk metal. The hybridization matrix used here is the same as in [39] and [40]. It is an approximation to the exact hybridization matrix of the free electron gas that is good if $k_F R$ is not too small. The diagonal part is given by

$$\Gamma_{1,1}(i\omega) = -i \ \text{sign}(\omega)\Delta_0, \tag{4.28}$$

like in the one impurity case studied in chapter 3. The off-diagonal part is

$$\Gamma_{1,2}(i\omega) = -\frac{\Delta_0}{k_F R}(\cos k_F R + i \ \text{sign} \sin k_F R). \tag{4.29}$$

In contrast to the previous section, the hybridization matrix is frequency independent except for the sign of ω. Here the strength of the inter-impurity hybridization is reduced with growing $k_F R$. Furthermore the off-diagonal part of the hybridization matrix has a finite real and imaginary part at the same time. This leads to an interplay of the ferromagnetic and an antiferromagnetic coupling mediated by the imaginary and the real part, respectively. In addition a competition of the magnetic coupling and the Kondo effect is to be expected. Since the strength of the inter-impurity coupling is getting arbitrarily weak, the single impurity behaviour is expected to be restored at finite $k_F R$. For small $k_F R$ the two impurities are coupled ferromagnetically, see e.g. [39], [49]. Since the coupling is rather strong, the system shows a combined Kondo effect and the Kondo temperature is much smaller than in the single impurity case. In this regime fRG is

not capable of reliably calculating the single-particle dynamics, since the effective on-site interaction is growing very large, like for the 1d-chain at even distances R.

The left panel of fig.(4.10) shows the spin-spin correlation function as a function of $k_F R$. The result is consistent with the one from [39]. The correlation function is oscillating while the strength is decaying fast. In [40] Jones et al. have estimated the RKKY interaction for the TIKM to decay with the third power of the impurity distance. Here the strength of the spin-spin correlation decays a little slower but still faster than $1/(k_F R)^2$. The effective mass is shown in the right panel of fig.(4.10). It is approaching its single impurity value as quickly as the correlations are decaying. One can observe that for a ferromagnetic correlation the effective mass is increased, while it is decreased for an antiferromagnetic coupling. The consequences of this behaviour for the single particle dynamics can be observed in fig.(4.11) for $U/\Delta_0 = 10$ and various $k_F R$. In the strong ferromagnetic coupling regime at small $k_F R$, the odd parity channel shows a sharp resonance while the even channel shows a rather broad resonance. In the diagonal part of the spectral function, the low energy region is dominated by the resonance from the odd parity channel. As the correlation of the impurity spins is getting weaker, the resonances in the even and in the odd parity channel are both getting closer to the shape known from the single impurity case. For values of $k_F R > 4$ no significant change in the spectral function can be observed. The interaction strength has only for rather small values of $k_F R$ a significant influence on the inter-impurity coupling. Qualitatively the same behaviour was observed using perturbative methods in [49]. In the high energy region the system is governed by the single impurity physics for all distances $k_F R$. There is no region in which an
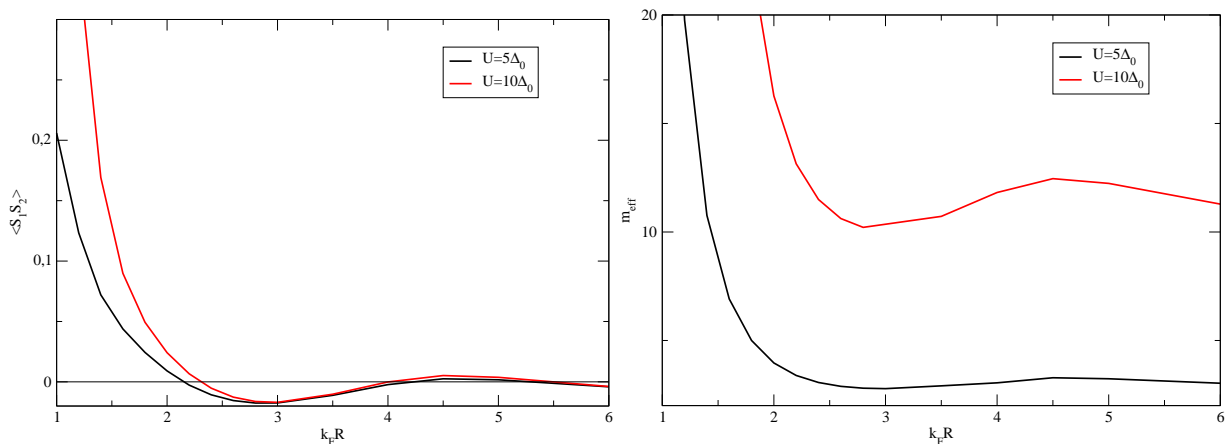

Figure 4.10: Spin-spin correlation (left) and effective mass (right) as a function of $k_F R$.
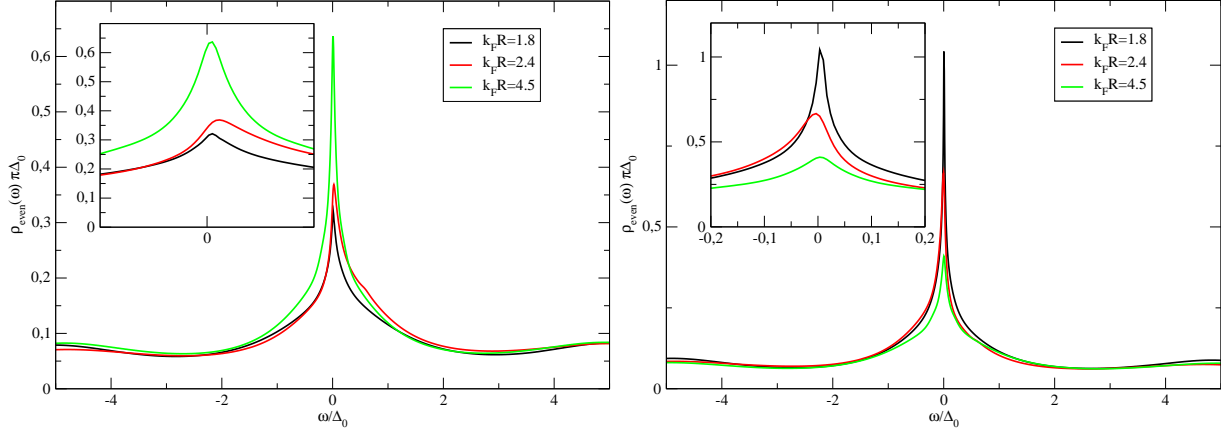
Figure 4.11: Even (right) and odd (left) parity spectral functions for $U/\Delta_0 = 10$ and different $k_F R$.

antiferromagnetically coupled system would show a splitting of the Kondo resonance like it was observed in the case of the 1d chain.

Summarizing, one can state, that the TIAM with a 3d free electron gas as electronic host behaves completely different compared to the TIAM with a 1d chain. While the system shows a correlated Kondo effect for small inter-impurity distances, it goes over to a system displaying single impurity behaviour for larger distances. Although there are phases in between where the impurity spins show a weak antiferromagnetic coupling, it is too weak to leave significant traces in the spectral function.

4.3   Summary

In this chapter the single particle dynamics of the TIAM were analysed with a 1d tight-binding chain and a 3d free electron gas as electronic hosts. It was made clear that the behaviour of the system largely depends on the electronic host and the corresponding hybridization matrix.

In the case of the 1d tight-binding chain the system showed a strong even/odd effect. For impurities coupled to sites with an even number of chain sites between them, the impurities are coupled ferromagnetically while for an odd number of chain sites in between the impurities are coupled antiferromagnetically. In this case fRG was used to calculate the one particle dynamics. At small inter-impurity distances the spectral function shows a splitting of the Kondo resonance. The antiferromagnetic coupling causes a suppression

at the chemical potential. This suppression gets stronger for larger interaction strengths, since the coupling of the impurity spins via RKKY interactions is also increased. With a growing inter-impurity distance the correlation effects are wearing off only slowly and remain visible for all finite R. The reason for this is the weak R-dependence of the hybridization matrix. The absolute value of the off-diagonal element at $\omega = 0$ shows no R-dependence at all. In this sense not the strength of the inter-impurity coupling is changed with R but only the frequency dependence.

If the host is a 3d electron gas, the behaviour is different. For small inter-impurity distances, the system displays a correlated Kondo effect with a much smaller Kondo temperature than in the single impurity case. With growing distance the correlations are decaying quickly and the spectral function is almost the same as in the single impurity case. The reason for this is that the off diagonal part of the hybridization function decays like $1/k_F R$. The strength of the inter-impurity coupling is getting weaker. Although there are distances at which the two impurity spins are antiferromagentically coupled, the coupling in these regimes is already too weak to cause something like a splitting of the Kondo resonance as in the 1d chain case.

Chapter 5

Quantum Dots

In the last few years the Anderson model has extensively been used to describe quantum dot (QD) systems [16],[65]-[71]. Although an artificial nanoscopic structure like a QD seems to be something entirely different than one or more impurity atoms in a metal, it turns out that both systems are very similar. A typical QD is a structure in which electrons are locally confined and subject to a Coulomb interaction. The mesoscopic size of the QD causes discrete energy levels that are well separated. For a theoretical description of the relevant physics only a few, or even only one, energy level near the Fermi surface is sufficient. The QD is connected to one or more electronic leads so that electrons can tunnel in and out of the dot. The Hamiltonian for such a QD system is given by

$$
\begin{aligned}
H &= \sum_{\vec{k},\sigma,\beta} \epsilon_{\beta,\vec{k}} c^{\dagger}_{\beta,\vec{k}\sigma} c_{\beta,\vec{k}\sigma} \\
&+ \sum_{\alpha,\sigma} \epsilon_{\alpha} d^{\dagger}_{\alpha,\sigma} d_{\alpha,\sigma} + U \sum_{\alpha} d^{\dagger}_{\alpha,\uparrow} d_{\alpha,\uparrow} d^{\dagger}_{\alpha,\downarrow} d_{\alpha,\downarrow} + \sum_{\alpha,\beta,\vec{k},\sigma} V_{\alpha,\beta} \left(c^{\dagger}_{\alpha,\vec{k}\sigma} d_{\alpha,\sigma} + \text{h.c.} \right) \\
&+ \sum_{\alpha \neq \alpha',\sigma} \frac{t_{\alpha,\alpha'}}{2} \left(d^{\dagger}_{\alpha,\sigma} d_{\alpha',\sigma} + \text{h.c.} \right) + \sum_{\alpha \neq \alpha',\sigma,\sigma'} \frac{U'_{\alpha,\alpha'}}{2} d^{\dagger}_{\alpha,\sigma} d_{\alpha,\sigma} d^{\dagger}_{\alpha',\sigma'} d_{\alpha',\sigma'} \, .
\end{aligned}
\tag{5.1}
$$

The model consists of N QDs described by the second and the third term coupled to M electronic leads described by the first term. The $N \times M$-matrix $V_{\alpha,\beta}$ describes the connection of the QDs to the different leads. The level position ϵ_{α} of a QD can be
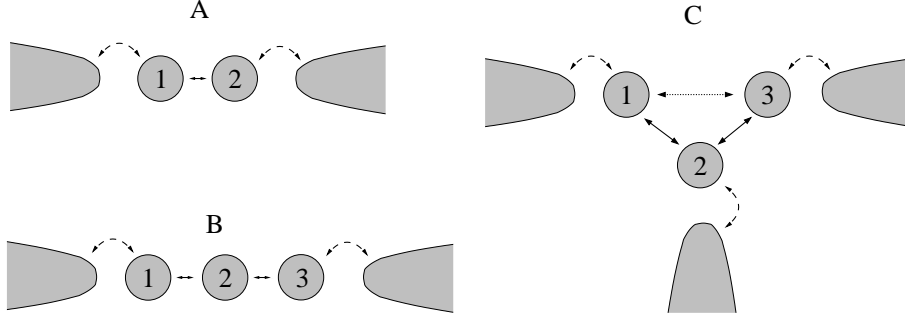
Figure 5.1: Geometries of quantum dots studied in this chapter.

controlled by an external gate voltage V_g. The last two terms describe the direct coupling of the different QDs by a direct hopping t and a Coulomb repulsion U'. For $U'_{\alpha,\alpha'} = t_{\alpha,\alpha'} = 0$, $N = M$ and $V_{\alpha,\beta} = V\delta_{\alpha,\beta}$ the system reduces to N decoupled single impurity systems. In this chapter four different QD geometries will be studied. The first one is the $SU(N)$ symmetric SIAM. It can be obtained from eq.(5.1) by setting $N = M$, $V_{\alpha,\beta} = V\delta_{\alpha,\beta}$, $t_{\alpha,\alpha'} = 0$ and $U'_{\alpha,\alpha'} = U$, i.e. N dots, every one coupled to its own host, without any hybridization between them, but with a Coulomb repulsion that does not differentiate between the different dots. This model can be used to describe degenerate levels with orthogonal wavefunctions like in rare earth impurity systems [22]. In this chapter it is also treated to analyse the ability of fRG to describe the effects of an inter-impurity Coulomb repulsion on the dynamics of a system.

The second geometry will be a linear chain of two QDs ((A) in fig.(5.1)). In this system the influence of the inter-dot hopping t, the level position ϵ_α and the inter-dot interaction U' will be investigated.

Additionally two different types of three dot systems will be studied. First a linear geometry with two leads as shown in (B) will be used. Finally a Y-shaped geometry as shown in (C) will be investigated. In this case the parameter $t_{1,3}$ is varied against $t_{1,2} = t_{2,3}$ and the influence of an inter-dot Coulomb interaction is analysed in the special case $t_{1,2} = t_{1,3} = t_{2,3}$.

In other publications, systems with parallel QD geometries have been studied [16],[65],[66]. In these geometries two or more dots are coupled to a left and a right lead in a parallel way. In these systems the indirect coupling between the dots leads to a ferromagnetic coupling of the spins on the dots as like in the $R = 0$ case of the TIAM. As for the TIAM, fRG is not capable of producing reliable results for these systems without a strong direct

hopping between the impurities. For this reason such systems will not be studied in this work.

5.1   Flow Equations

Very similar to the proceeding in the previous chapter, the first step towards flow equations for the QD model is the calculation of the free propagator. It has to be determined by an inversion of a $N \times N$-matrix. For the cases studied in this chapter, this can be done analytically and the result for each case will be given in the corresponding section. Like the electronic host in chapter 3, the leads in this chapter will be flat electronic bands of infinite bandwidth. Consequently the hybridization matrix $\Gamma_{\alpha,\alpha'}(i\omega)$ is frequency independent except for a dependence on the sign of ω in the imaginary part. The next step towards a set of flow equations is the parametrization of the two-particle vertex. When including an inter-dot interaction $U'_{\alpha,\alpha'}$, the parametrization of the vertex is more complicated than in the previous chapters:

$$
\bar{\gamma}_2^\Lambda(\xi_1', \xi_2'; \xi_1, \xi_2)
$$

$$
= \delta_{m_1,m_1'} \delta_{m_2,m_2'} \delta_{m_1,m_2} \sum_\alpha \delta_{m_1,\alpha} \, \mathcal{M}_\alpha^{1,\Lambda}(\tilde{\xi}_1', \tilde{\xi}_2'; \tilde{\xi}_1, \tilde{\xi}_2)
$$

$$
+ \delta_{m_1,m_1'} \delta_{m_2,m_2'} \delta_{m_1,\bar{m}_2} \sum_{\alpha\neq\beta} \delta_{m_1,\alpha} \delta_{m_2,\beta} \, \mathcal{M}_{\alpha,\beta}^{2,\Lambda}(\tilde{\xi}_1', \tilde{\xi}_2'; \tilde{\xi}_1, \tilde{\xi}_2)
$$

$$
- \delta_{m_1,m_2'} \delta_{m_2,m_1'} \delta_{m_1,\bar{m}_2} \sum_{\alpha\neq\beta} \delta_{m_1,\alpha} \delta_{m_2,\beta} \, \mathcal{M}_{\alpha,\beta}^{3,\Lambda}(\tilde{\xi}_1', \tilde{\xi}_2'; \tilde{\xi}_1, \tilde{\xi}_2)
$$

$$
+ \delta_{m_1,m_2} \delta_{m_1',m_2'} \delta_{m_1,\bar{m}_1'} \sum_{\alpha\neq\beta} \delta_{m_1,\alpha} \delta_{m_1',\beta} \, \mathcal{M}_{\alpha,\beta}^{4,\Lambda}(\tilde{\xi}_1', \tilde{\xi}_2'; \tilde{\xi}_1, \tilde{\xi}_2)
$$

$$
+ \delta_{m_1,m_2} \delta_{m_1',\bar{m}_2'} \delta_{m_1,m_1'} \sum_{\alpha\neq\beta} \delta_{m_1,\alpha} \delta_{m_2',\beta} \, \mathcal{M}_{\alpha,\beta}^{5,\Lambda}(\tilde{\xi}_1', \tilde{\xi}_2'; \tilde{\xi}_1, \tilde{\xi}_2)
$$

$$
- \delta_{m_1,m_2} \delta_{m_1',\bar{m}_2'} \delta_{m_1,m_2'} \sum_{\alpha\neq\beta} \delta_{m_1,\alpha} \delta_{m_1',\beta} \, \mathcal{M}_{\alpha,\beta}^{6,\Lambda}(\tilde{\xi}_1', \tilde{\xi}_2'; \tilde{\xi}_1, \tilde{\xi}_2)
$$

$$
+ \delta_{m_1,\bar{m}_2} \delta_{m_1',m_2'} \delta_{m_1,m_1'} \sum_{\alpha\neq\beta} \delta_{m_1,\alpha} \delta_{m_2,\beta} \, \mathcal{M}_{\alpha,\beta}^{7,\Lambda}(\tilde{\xi}_1', \tilde{\xi}_2'; \tilde{\xi}_1, \tilde{\xi}_2)
$$

$$
- \delta_{m_1,\bar{m}_2} \delta_{m_1',m_2'} \delta_{m_1,m_2'} \sum_{\alpha\neq\beta} \delta_{m_1,\alpha} \delta_{m_1',\beta} \, \mathcal{M}_{\alpha,\beta}^{8,\Lambda}(\tilde{\xi}_1', \tilde{\xi}_2'; \tilde{\xi}_1, \tilde{\xi}_2) \, ,
$$

with $\tilde{\xi}_i^{(')} = (\sigma_i^{(')}, i\omega_i^{(')})$ and $\alpha, \beta = 1, ..., N$ being impurity indices. In all cases $\mathcal{M}_{\alpha,\beta}^{i,\Lambda} = \mathcal{M}_{\beta,\alpha}^{i,\Lambda}$, but the number of terms needed is increasing with the number of impurities N. Due to special symmetries, the number of different functions, which are necessary to parametrize the vertex, can be considerably reduced. The last four terms $\mathcal{M}_{\alpha,\beta}^{i,\Lambda}$, $i = 5, ..., 8$, are only needed in systems with an inter-impurity interaction U'. For two identical impurities and with $U' = 0$, the same parametrization as in the previous chapter remains. In systems with four or more impurities and an inter-impurity interaction, additional terms are necessary but since such systems are not studied in this work, these terms are not given here. Like in the previous chapter the $\mathcal{M}_{\alpha,\beta}^{i,\Lambda}$ consist of spin conserving $\delta-$ functions and frequency-dependent functions $\mathcal{U}_{\alpha,\beta}^{i,\Lambda}(i\omega_1', i\omega_2'; i\omega_1, i\omega_2)$. It is easy to convince oneself of the necessity of the last four terms due to the inter-impurity interaction by drawing all possible diagrams for the two-particle vertex in second order perturbation theory. The flow equations for the $\mathcal{U}_{\alpha,\beta}^{i,\Lambda}$ and the components of the self-energy $\Sigma_{i,j}^{\Lambda}$ are calculated in the same way as for the TIAM.

5.2   Results

The results presented in this chapter are obtained from the modified fRG scheme (mfRG) and the approximative scheme App3, that was introduced in chapter 3 and that is explained in detail in appendix B. The reason for the use of the approximative scheme is that the discrepancies between full fRG and the modified scheme App3 are very small for the multi-dot systems studied here. Due to these small discrepancies the approximative scheme is preferable for the calculation of spectral functions, because the reduced numerical effort allows the use of a finer frequency mesh, leading to better results from the analytic continuation.

5.2.1   The SU(N) Anderson Model

From the Hamiltonian given in eq.(5.1) this model is obtained for $U'_{\alpha,\alpha'} = U$, $t_{\alpha,\alpha'} = 0$, $N = M$ and $V_{\alpha,\beta} = V\delta_{\alpha,\beta}$. In the QD framework, this model describes N identical

dots or degenerate dot levels that are coupled to independent leads, so that no inter-dot hybridization is present, while at the same time the inter-dot Coulomb repulsion is as strong as the on-site interaction. This is a rather unphysical situation for a QD. The physical application of this model is found in the description of rare-earth impurity systems, where it very effectively describes the degenerate $f-$orbitals of the impurities with their orthogonal wavefunctions [22]. Additionally this model allows to judge the ability of fRG to describe the influence of an inter-dot interaction on the dynamics of a multi-dot system. This is possible because the scaling of the Kondo temperature with the degeneracy factor, i.e. the number of dots N, is known for the Coqblin-Schrieffer model, which is a generalization of the Kondo model [62].

The free propagator for this problem as well as the self-energy and the full propagator are diagonal in the impurity indices since there is no inter-dot hybridization. The high symmetry of this model makes it possible to use only one frequency-dependent function for the parametrization of the two-particle vertex. The flow equations are basically the same as for the SIAM. The degeneracy factor N only enters the flow equations as a multiplying factor. For this reason the treatment of arbitrary degeneracy factors is easily possible within the fRG scheme. Here only the particle-hole symmetric case ($\epsilon_d = -U(N - 1/2)$) will be studied.

From mean-field considerations one would expect the effective interaction strength to increase with growing N. The result of this increased interaction would be an increase of the effective mass and consequently a decrease of the Kondo temperature and a sharpening of the Kondo resonance in the spectral function. 2PTh shows exactly this behaviour. The self-energy from 2PTh can be related to the one from the SIAM. If the self-energy for the SIAM as calculated in chapter 3 is given by

$$\Sigma^{2PTh,N=1}(i\omega) = U^2\chi(\omega) \, ,$$

with χ being the evaluated diagram shown in fig.(3.2) for $U = 1$, the self-energy for arbitrary N is given in second order perturbation theory by

$$\Sigma^{2PTh}(i\omega) = \left(U^2 + 2(N - 1)U^2\right)\chi(\omega),$$

i.e. the diagrammatic structure does not change. Therefore the effective mass, which is given by the slope of $\Sigma(i\omega)$ at $\omega = 0$, is scaled up with growing N.
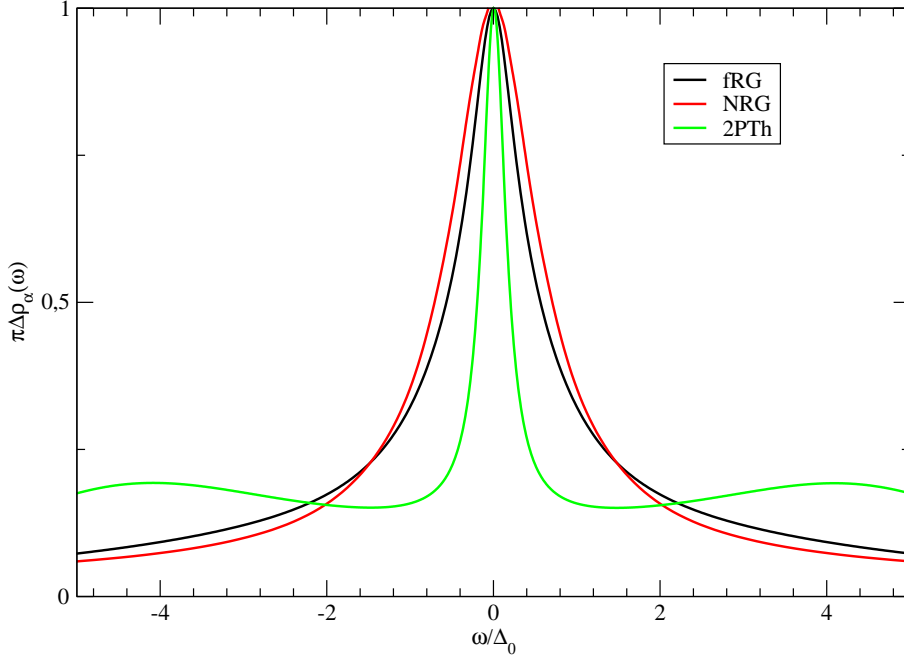
Figure 5.2: $SU(N)$ SIAM: Spectral functions for $U/\Delta_0 = 5$ and $M = 2$ impurities.

Calculations using NRG and Bethe ansatz show that the Kondo temperature is increasing instead of decreasing with growing N. This seems plausible, since the on-site interaction favours a single-occupancy of the impurity levels leading to a local moment and the Kondo resonance. At the same time the inter-dot interaction suppresses this single-occupancy and therefore counteracts the on-site interaction and suppresses the Kondo effect.

Fig.(5.2) shows the spectral functions from NRG, fRG and 2PTh for $N = 2$ and $U/\Delta_0 = 5$. 2PTh already shows severe discrepancies to fRG and NRG, while the latter two are in good agreement. This means that while 2PTh is not able of correctly including an inter-impurity interaction, fRG is capable of correctly treating the effects of such an interaction.

While NRG can be used to obtain results for systems with two impurities, it is not capable of going beyond this, due to an exponential rise of the numerical effort. For fRG this is no problem as pointed out above. The spectral functions for $U/\Delta_0 = 5$ are depicted in fig.(5.3) for different degeneracy factors N. While it generally looks like in the single impurity case, the Kondo resonance shows severe differences. With growing N the Kondo resonance is getting broader. This is caused by the influence of the inter-impurity interaction that suppresses the Kondo effect by suppressing a single occupancy of the impurity sites. The more impurity levels are involved, the greater the influence of
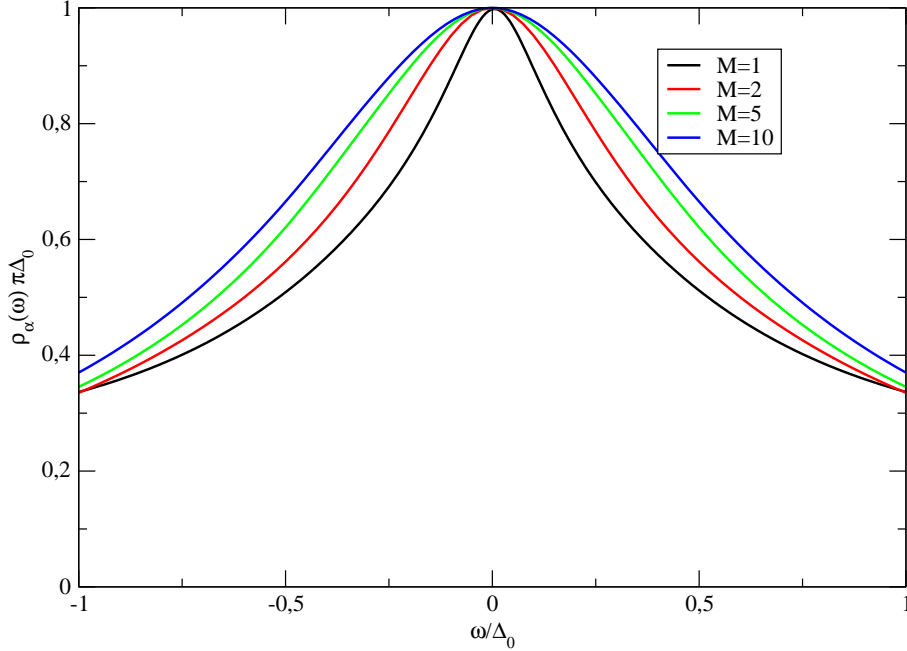
Figure 5.3: $SU(N)$ SIAM: Spectral functions for $U/\Delta_0 = 5$ and different impurity numbers M.

the inter-dot interaction is. For constant interaction strength, the shape of the spectral function is getting closer to the one of the non-interacting SIAM.

To further analyze the way the dynamics of a multi-impurity system change with growing impurity number, the effective mass is shown as a function of the degeneracy factor N for different interaction strengths (fig.(5.4)). In the non-interacting case it naturally takes the value of 1. For all values of U the effective mass drops rather fast for small impurity numbers and seems to saturate for large impurity numbers. It is noticeable that all three curves seem to converge against different values. That means that for $N \to \infty$ there is a finite Kondo temperature, that depends on the interaction strength $U = U'$, and that the Kondo temperature is not scaled to infinity as the impurity number grows.

For the SU(N)-symmetric Coqblin-Schrieffer model it was predicted that the exponent of the effective mass scales like $1/N$ [62]. Consequently m^N_{eff} should show the same exponential behaviour as a function of U for different values of N. Although fRG is not capable of reproducing the exponential behaviour in the strong coupling limit, the curves in fig.(5.5) display the same logarithmic derivative (the curves are almost parallel). That means fRG shows the predicted scaling behaviour with growing N. This scaling behaviour cannot be observed in fig.(5.4), due to additional prefactors in the effective mass.
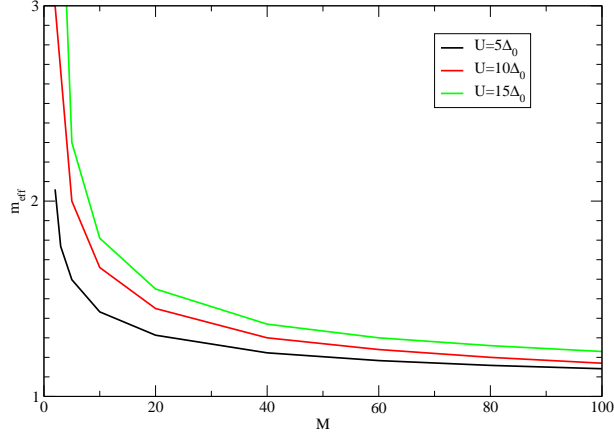
Figure 5.4: Effective mass as a function of the impurity number for different interaction strengths.
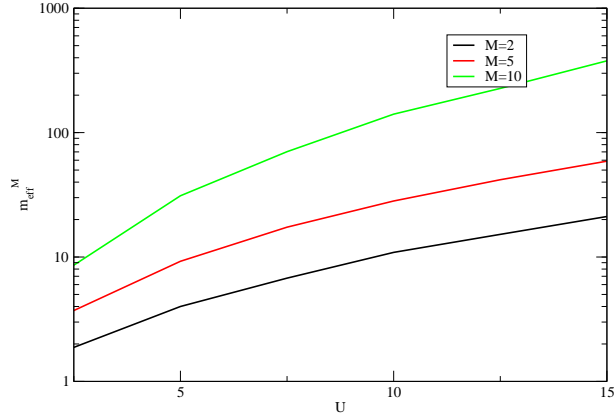

Figure 5.5: $SU(N)$ SIAM: $(m_{eff})^N$ as a function of the interaction strength for different impurity numbers.

Overall it can be said that in contrast to 2PTh, fRG correctly describes the influence of an inter-dot interaction on the one-particle dynamics. It can be used to reliably calculate spectral properties of the SU(N)-symmetric SIAM, as long as the interaction strength does not get too large. The value of U, up to which reliable data can be obtained increases with growing N.

5.2.2 Linear Double Quantum Dot

The double quantum dot (DQD), that is investigated in this section, consists of a left and a right lead with one quantum coupled to each. Both dots are connected with a direct
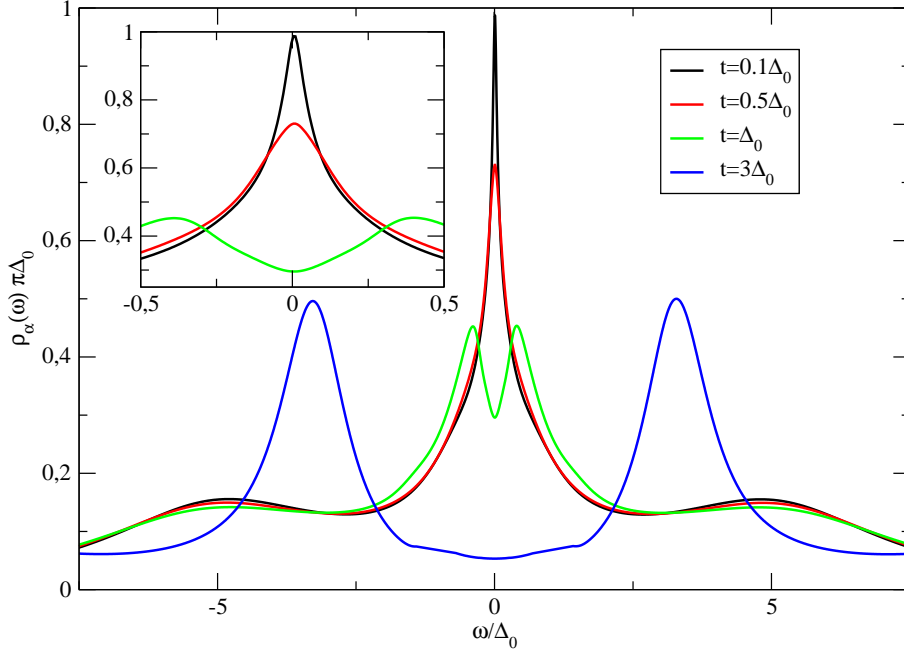
Figure 5.6: Lin. DQD: Spectral functions for $U/\Delta_0 = 10$, $U' = 0$

hopping t. Experimentally such a setup was studied in [63]. The parameters in eq.(5.1) are set to $N = M = 2$, $V_{\alpha,\beta} = V\delta_{\alpha,\beta}$, $t_{\alpha,\alpha'} = t$, $U'_{\alpha,\alpha'} = U'$, $\epsilon_\alpha = -U/2 - U' - V_g$, where V_g is an external gate voltage. The free propagator in this section is the same as for the TIAM (eq.(4.3)) with

$$\Gamma_{1,1}(i\omega) = -i \, \text{sign}(\omega)\Delta_0, \quad \Gamma_{1,2}(i\omega) = t \; . \tag{5.2}$$

For $t = \Delta_0$ and $U' = 0$ this model is equivalent to the TIAM with the linear chain as electronic host if the frequency dependence of the hybridization matrix is neglected. The $R = 1$ case of the linear chain TIAM, where the frequency dependence is not important, has an almost identical spectral function as this linear DQD. Thus the results from the DQD can be applied to the TIAM for small values of R and vice versa. This is especially true for the dependence on the inter-impurity interaction U', that was not investigated for the TIAM.

First of all the influence of the direct hopping on the one-particle dynamics is going to be analyzed. The inter-impurity interaction is set to $U' = 0$ for the moment as well as the gate voltage $V_g = 0$. Using various numerical methods for the calculation of transport properties, especially the conductance, it has been shown that a DQD has three phases

depending on the strength of the direct hopping t [67]. For small t both dots form an individual Kondo singlet with their adjacent leads. For larger t the system displays a local singlet state, where the electrons on both dots are antiferromagnetically coupled. At very large t the system is in a molecular orbital state, where the even parity orbital, that is defined in the same way as for the TIAM, is doubly occupied. The system shows a smooth cross-over from one state to the other. In fig.(5.6) spectral functions for various values of t are shown. The three phases are clearly visible. For $t/\Delta_0 = 0.1$ the spectral function looks like the one from the SIAM. Both dots form an individual Kondo singlet with their lead. With growing t the Kondo resonance is suppressed and for $t/\Delta_0 = 1$ the system is in a local singlet phase. If the hopping is increased further, there are two orbital resonances instead of the split Kondo resonance. Only in this phase the high-energy physics are effected by the hopping. For very large t only the orbital peaks remain in the spectral function.

Like in the previous chapter the splitting of the Kondo resonance can be understood in terms of a level shift in the even and odd parity channel. This shift δ of the resonance in the even and odd spectral function is depicted in the left panel of fig.(5.7). Without interaction the resonance is shifted exactly by a value of t. With interaction the shift is suppressed for small values of t before growing linearly with t. The three phases can be observed here as well. In the Kondo singlet phase the level-shift is close to 0. In the phase where the system forms an antiferromagnetic singlet the shift is slowly increasing and in the orbital molecular phase the shift is growing linearly with t. One can observe very clearly that for a larger interaction strength a larger value of t is needed to drive the
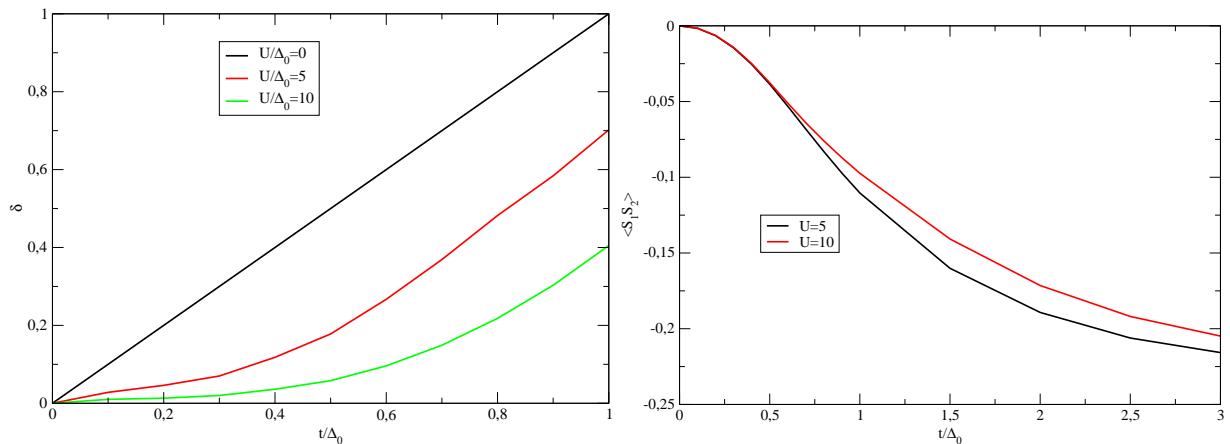

Figure 5.7: Lin. DQD: Splitting of the spectral function as a function of t.
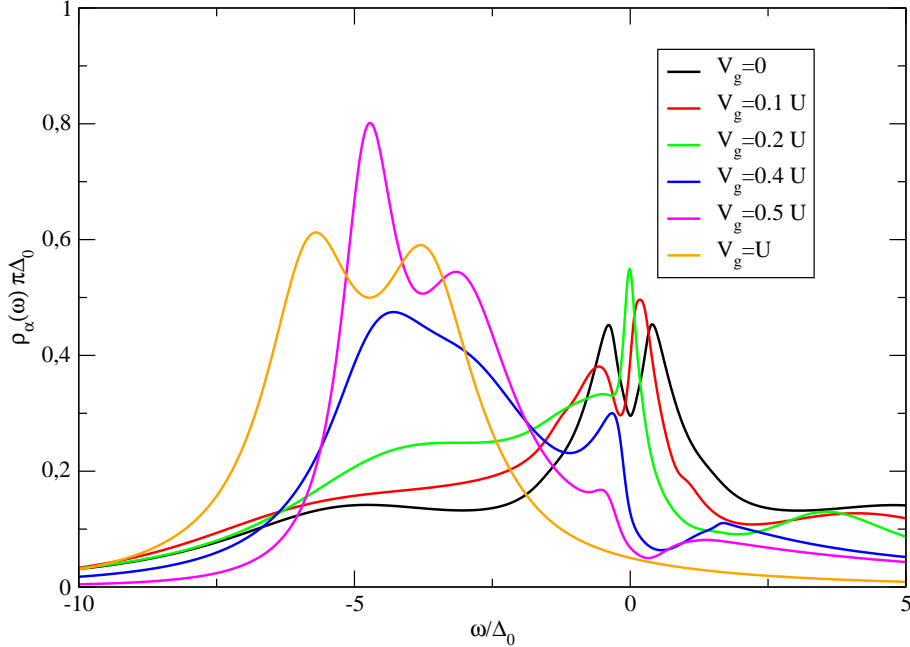
Figure 5.8: Lin. DQD: Spectral functions for $U/\Delta_0 = 10, t = \Delta_0$ and various values of V_g.

system out of the Kondo phase or into the molecular orbital phase. The splitting of the resonance in the total spectral function is influenced not only by the level shift, but also by the width of the resonances in the even and odd parity channel. If the resonances are sharper, the resonance shift that is necessary to observe a splitting of the total resonance is smaller. For this reason the splitting of the resonance in the total spectral function appears around $t = 0.7\Delta_0$ for interaction strengths from $U = 0$ to $U = 15\Delta_0$.

These phases can also be found in the spin-spin correlation function. In the Kondo phase the spin-spin correlation is weak. The local moments on both dots are almost uncorrelated and are individually screened. The correlation continuously increases in the local singlet phase, before it saturates in the molecular orbital phase, where both electrons form a spin singlet in the even orbital.

In contrast to systems of impurity atoms in metal, in a quantum dot system it is often possible to tune the impurity level position by applying an external gate voltage V_g. The influence of such a gate voltage on the single particle dynamics is now going to be analyzed in a system that is in the combined singlet phase. The way V_g is defined here, a positive V_g shifts the impurity levels down. Only positive V_g will be considered since negative gate voltages would just shift the spectral function in the opposite direction. The spectral
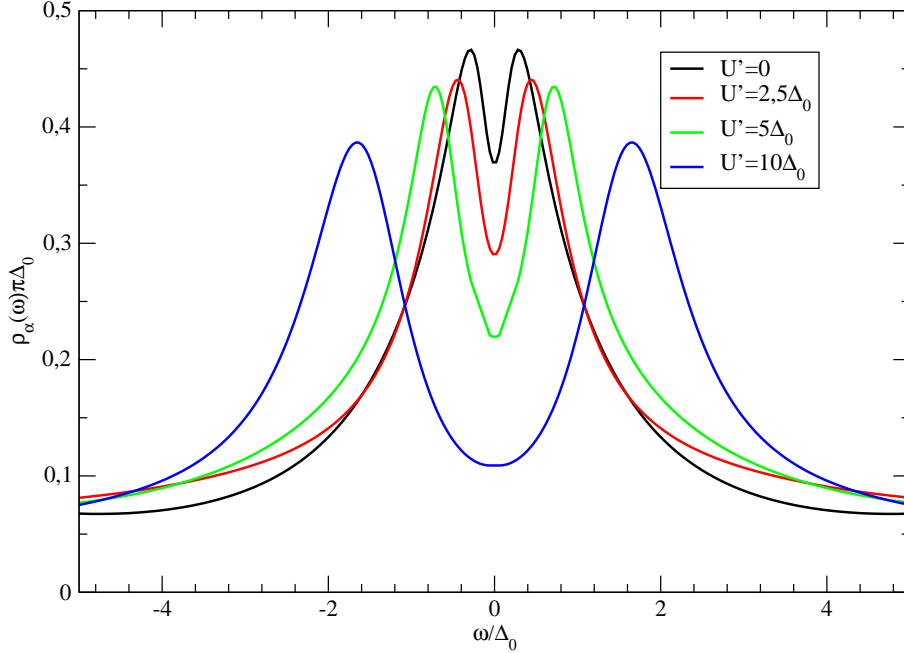
Figure 5.9: Lin. DQD: Spectral functions for $U/\Delta_0 = 10, t = \Delta_0$ and various values of U'.

functions for $U/\Delta_0 = 10$, $t = \Delta_0$ and different gate voltages are presented in fig.(5.8). For small gate voltages the peak above the chemical potential, which is caused by the shift in the odd parity channel, approaches $\omega = 0$. The gate voltage counteracts the shift of the resonance in the odd parity channel due to the hopping. Like the shift due to the hopping the effect of the gate voltage is suppressed by the on-site interaction. For not too large gate voltages the odd parity resonances are pinned against the chemical potential. This pinning effect is stronger for a larger interaction strength. Approaching the chemical potential the weight of the odd parity resonance is increased. For a sufficiently large gate voltage the odd parity resonance is shifted below the chemical potential and the spectral weight is quickly shifted away. The even parity resonance, that was below the chemical potential, is suppressed first and then shifted by a value of approximately V_g.

This behaviour can be understood when looking at the occupation numbers. Increasing V_g, the occupancy of the even parity channel quickly approaches 2. Consequently the Kondo resonance in this channel disappears very fast. In the odd parity channel, the interaction counteracts the double occupancy causing the pinning effect. When a sufficiently large V_g leads to a doubly occupied odd parity channel, the Kondo resonance is suppressed here as well. For large V_g the hole spectral weight is concentrated around

the right atomic peak that is now at $\omega = -V_g$. The spectral function now has the same shape as in the non-interacting case only shifted by a value of $V_g - U/2$. The system is now occupied by four electrons. The interaction does not influence the systems dynamics anymore.

The inclusion of an inter-dot interaction U' has a severe impact on the spectral properties of the DQD. For $U/\Delta_0 = 10$ and $t = \Delta_0$ the results of a growing inter-impurity interaction for the spectral function are displayed in fig.(5.9). Like in the case of the SU(N)-symmetric SIAM the inter-dot interaction counteracts the Kondo effect caused by the on-site interaction. The effective mass is lowered and the splitting of the Kondo resonance is increased. Besides the effect already known from the SU(N) SIAM, which leads to a lowering of the effective mass, the reason for this behaviour is that the inter-dot interaction creates a constant contribution to the off-diagonal part of the self-energy that serves as an effective hopping that is much larger than the bare hopping. Consequently the system is driven away from the Kondo singlet phase already for rather small values of t and the transition to the molecular orbital phase takes place for smaller t as well. Summarizing one can say that an inter-dot interaction strengthens the correlation effects between the dots while it suppresses the forming of an individual Kondo singlet on each dot.

5.2.3 Linear Triple Quantum Dot

In this section the dynamics of a linear triple quantum dot (TQD) are investigated. The system consists of a left (1) and a right dot (3), which are connected to a left and a right lead. Both dots are connected to a central dot (2) with a hopping amplitude t. This system is obtained from the Hamiltonian given in eq.(5.1) with the parameters $N = 3$, $M = 2$, $V_{1,1} = V = V_{3,2}$ and $V_{\alpha,\beta} = 0$ in all other cases, $t_{1,2} = t_{2,3} = t$, $t_{1,3} = t'$. The inter-dot interaction and the gate voltage will be set to 0 in this section ($U'_{\alpha,\alpha'} = 0$, $\epsilon_\alpha = -U/2$). The free propagator is obtained by the inversion of an 3×3-matrix, which reads

$$
\mathcal{G}^0(i\omega) = \begin{pmatrix} i\omega + U/2 + i\,\mathrm{sign}(\omega)\Delta_0 & -t & -t' \\ -t & i\omega + U/2 & -t \\ -t' & -t & i\omega + U/2 + i\,\mathrm{sign}(\omega)\Delta_0 \end{pmatrix}^{-1} . \quad (5.3)
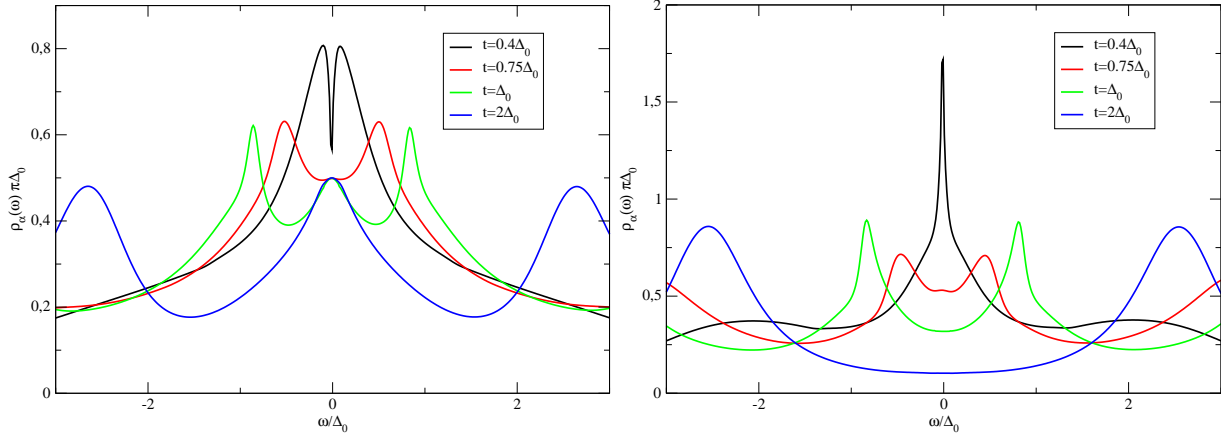$$

88

Figure 5.10: Lin. TQD: Spectral functions of dot 1 (left) and dot 2 (right) for $U/\Delta_0 = 5$ and various values of t.

Here only the case $V_g = 0$ and $t' = 0$ is treated. For these values the system shows particle-hole symmetry and the total number of electrons on the TQD is three. Consequently there is a magnetic moment interacting with the lead electrons in every possible configuration. The phases of a linear TQD have been analysed in [70],[71] as a function of the hopping strength t.

Like the DQD, this model has three phases. If t is small, the system shows a two stage Kondo effect (TSK). The spins on dot 1 and 3 are screened by conduction electrons in the adjacent leads. The spin on the middle dot causes a Kondo effect with a much lower Kondo temperature and a much higher effective mass than the other two. The spins on the three dots are almost uncorrelated. When t is increased, the hopping causes antiferromagnetic correlations between the neighbouring dots. The system forms an antiferromagnetic spin chain (AFM) with a total spin $1/2$, that is screened by the conduction electrons. For large t the system crosses over to a molecular orbital (MO) regime like in the DQD case. The bonding orbital is filled with two electrons. The spin of the third electron in the antibonding orbital is screened by the lead electrons.

 In the TSK regime fRG cannot be used to obtain reliable data. The strong Kondo effect on the middle dot results in a very large effective on-site interaction. Like in other systems with a very low Kondo temperature, fRG is not capable of describing this strong coupling regime. For larger t the spectral functions are shown in fig.(5.10). For the smallest value of t, one can still see that the Kondo resonance on the middle dot is a lot sharper than on the outer dots.

The AFM regime is characterized by strong spin-spin correlations with an absolute value depending on the interaction strength. The local moments on the three dots bind into a rigid antiferromagnetic chain with total spin 1/2. The coupling between the spins has been estimated to be $J = 4t^2/U$ in [70]. The red curve in fig.(5.10) ($t = 0.75\Delta_0$) belongs to this phase. The spectral functions on all three dots are almost identical here. They are dominated by two peaks at $\omega \approx \pm J$. These peaks correspond to the spin chain and are not shifted Kondo resonances. Although the total spin 1/2 is Kondo screened, there is hardly any Kondo resonance in this case. The total spin is screened by the electrons in both leads. This leads to an effective hybridization of $\Delta_{0,eff} = 2\Delta_0$. The consequence is not only a greater width of the resonance but also a reduced height, which is now $1/\pi\Delta_{0,eff} = 1/2\pi\Delta_0$. Knowing this, the Kondo resonance can be identified as the tiny maximum at $\omega = 0$.

For larger values of t the system crosses over to the MO phase. The broad peaks of the bonding and the antibonding orbital form on all three dots, while their weight on the middle dot is approximately twice as large as on the outer dots. The unpaired electron leads to a clear Kondo resonance on the outer dots as it is screened by the lead electrons. This can be understood by looking at the eigenfunctions of a three-site tight-binding model without interaction and open boundary conditions. The wavefunction of the binding orbital in this case is a sine-function with knots on the boundaries and a single maximum in the middle. Therefore the corresponding resonance has the most weight on the middle dot. The wavefunction of the antibonding orbital is a sine-function with knots on the boundaries and in the middle. Consequently the Kondo resonance from the electron in the antibonding orbital is visible only on the outer dots but not on the middle dot. The height of this Kondo resonance is again $1/2\pi\Delta_0$, like in the AFM phase. One electron is screened by the electrons in two leads. The Kondo temperature belonging to the screening of the antibonding electron is determined by U and Δ_0. For large t it approaches the single impurity value corresponding to $U/2\Delta_0$.

The values of t belonging to a certain phase are non-universal and depend on U. For the cross-over from the TSK to the AFM phase the interplay between the single impurity Kondo temperature $T_{1,K}$ and the coupling of the spins J is relevant. For the crossover from the AFM to the MO phase the relation between J and the hopping t is important. Generally the value of t, where the transitions take place, is larger the stronger the interaction is.
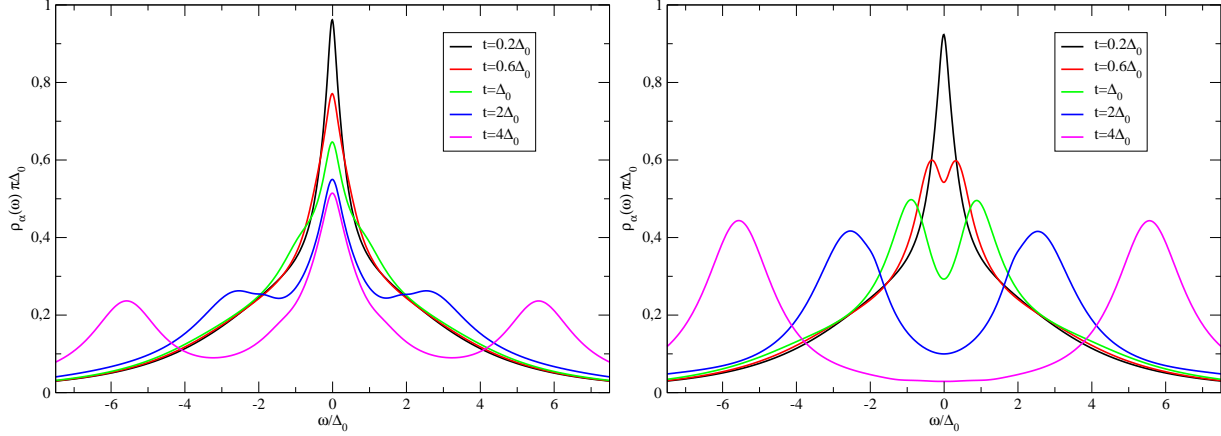
Figure 5.11: YTQD: Spectral functions of dot 1 (left) and dot 2 (right) for $U/\Delta_0 = 5$, $t' = 0$ and various values of t.

5.2.4 Triple Quantum Dot with Y-Geometry

The configuration investigated in this section is very similar to the one in the last section. The only difference is that not only the outer dots 1 and 3 are coupled to leads. Here the middle dot is coupled to a lead as well. The parameters in the Hamiltonian (eq.(5.1)) are $N = M = 3$, $V_{\alpha,\beta} = \delta_{\alpha,\beta}$, $t_{1,2} = t_{2,3} = t$, $t_{1,3} = t'$ and $U'_{\alpha,\alpha'} = U'$. The level position is set to $\epsilon_\alpha = -U/2 - U'$. The case $U' \neq 0$ will only be considered at the end of the section for the symmetric situation $t = t'$. The free propagator is the same as in the previous section except for one difference: Due to the additional coupling of the middle dot to a lead, all diagonal elements of the inverse propagator are identical including a hybridization term. Besides its application to quantum dot geometries, this configuration can be used to study clusters of atomic impurities in metals, like Cr-clusters in Au [64]. In [69] Savkin et al. used a Green function for the electronic host, which is given by

$$\mathcal{G}_c^{-1}(i\omega, R) = \mathcal{G}_c^{-1}(i\omega, |\vec{R}_\alpha - \vec{R}'_\alpha|) = \delta_{\alpha,\alpha'}\mathcal{G}_c^{-1}(i\omega, 0) - t_{\alpha,\alpha'} \ . \tag{5.4}$$

The inter-impurity hybridization is given by $t_{\alpha,\alpha'}$. By the use of this conduction band Green function, a connection between quantum dots and impurity atoms in a metal is possible. Since all impurities have a direct hybridization with the embedding metal, this connection between QDs and impurity atoms can only be made if all dots are connected to a lead. In this section only real $t_{\alpha,\alpha'}$ will be considered, leading to antiferromagnetic correlations. Like in the previous section the case $t' = 0$ will be studied first. As the

linear TQD, this system is particle-hole symmetric for $t' = 0$ and the above choice for ϵ_α. The TQD with Y-geometry (YTQD) shows some similarities to the linear TQD and some similarities to the DQD. Like the linear TQD, this system is filled with three electrons in the particle-hole symmetric case. Depending on the strength of the hopping parameter t, the system can be in different phases. For small t the system rather behaves like a DQD than like a linear TQD. Due to the additional lead, the system is not in a TSK regime but all three dots are screened individually with the same Kondo temperature, that is approximately given by the single impurity value. The spin-spin correlations are weak in this phase. The spectral functions of the outer and the middle dot look like in the single impurity case (fig(5.11)).

For larger t the antiferromagnetic coupling is increased. Unlike the linear TQD this system does not show a separate AFM phase, in which the three spins bind into an antiferromagnetic spin chain. The spin-spin correlations behave like in the DQD case. They increase monotonically and saturate for large values of t. At intermediate values of t the system behaves very similar to the DQD in the local singlet phase. In the spectral function on the outer dots, the Kondo resonance is suppressed and approaches the resonance caused by the screening of the electron in the antibonding orbital. On the middle dot the splitting of the Kondo resonance known from the DQD can be observed as the molecular orbitals develop. Overall, the system shows a smooth transition from the individual Kondo phase to the MO phase.

The MO phase is very similar to the one in the linear TQD. The Kondo screening of the electron in the antibonding orbital is completely unaffected by the third lead, since the relevant wavefunction has no weight on the middle dot. The height and width of the Kondo resonance are the same as for the linear TQD. Only the bonding is slightly different. The additional lead causes charge fluctuations that result in a greater width of the peaks. Therefore the peaks belonging to the bonding orbital are less well developed for a given value of t than in the case of the linear TQD. Again values of t, where the system shows a certain behaviour, are non-universal and depend on the interaction strength U. Like in the other dot systems, that were investigated for larger values of U, also larger values of t are needed for correlation effects to influence the systems properties. Compared to the linear case, the hopping has to be a little bit larger to enter the MO phase.

Especially for the description of atomic clusters in a metal but also for the description of QDs the inclusion of t' is important. A non-zero value of t' corresponds to a triangular arrangement of the dots instead of a linear one. In the special case $t = t'$ the three dots
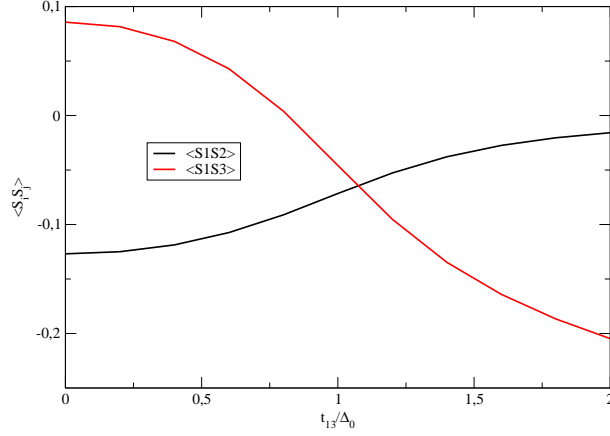
Figure 5.12: YTQD: Spin-spin correlation function for $U/\Delta_0 = 5$ and $t = \Delta_0$ as a function of the hopping t'.

form an equilateral triangle. First the influence of an increasing t' is studied while t is kept constant. Afterwards the case $t = t'$ will be studied, including the influence of an inter-impurity interaction.

For $t' = 0$ the system has been described above. The spins of adjacent dots are antiferromagnetically coupled by the hopping t. The inclusion of t' leads to frustration effects. One expects the spin correlations to be suppressed first before, for larger $t' > t$, the dots 1 and 3 form a dimer with an almost uncorrelated dot 2. The spin-spin correlation function shown in fig.(5.12) shows the expected behaviour. The antiferromagnetic correlation between the outer and the middle dot is suppressed and goes to 0 for $t' > t$ while the
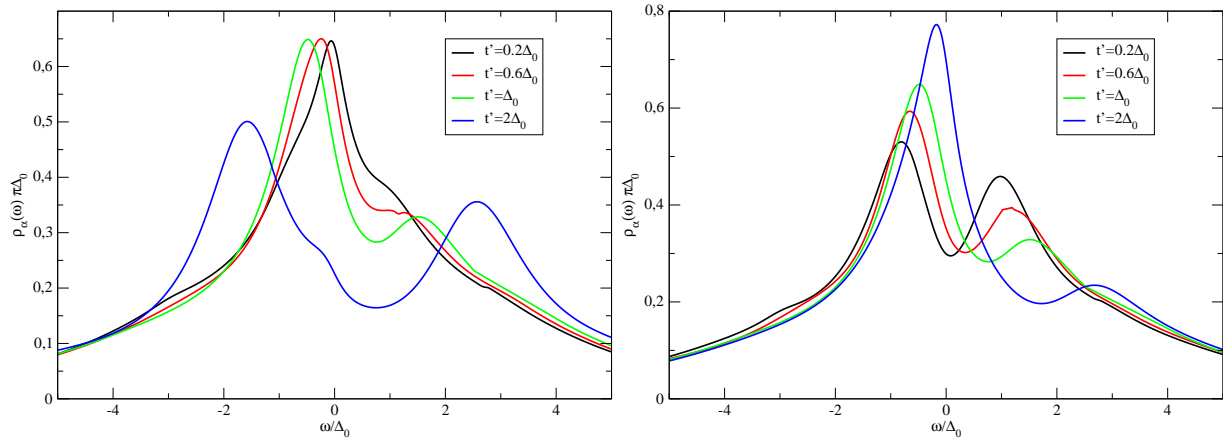

Figure 5.13: YTQD: Spectral functions of dot 1 (left) and dot 2 (right) for $U/\Delta_0 = 10$ and various values of t.
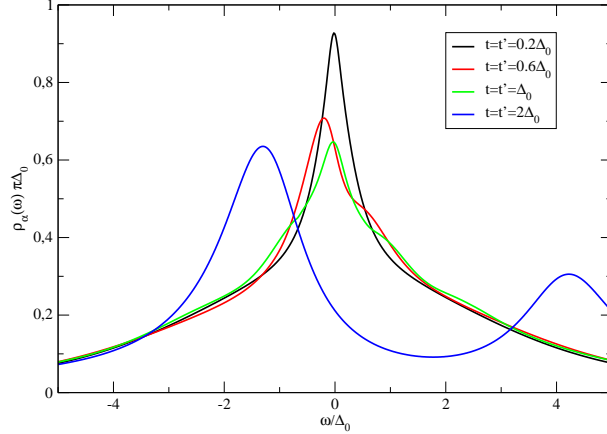
93

Figure 5.14: YTQD: Spectral functions for $U/\Delta_0 = 5$ and for various $t = t'$.

ferromagnetic correlation between dot 1 and 3 is suppressed for small t' as well and turns into a strong antiferromagnetic correlation for large $t' > t$.

The spectral functions mirror this development (fig.(5.13)). On the outer dots the increased t' leads to a broadening and to a shift of the Kondo resonance. While for small t' the shift is suppressed, for larger t' the resonance shift grows linearly with t'. For large t' the spectral function shows the same MO behaviour as for the DQD. The system has changed from a trimer to a dimer with an additional dot. The spectral function of the middle dot displays the inverted development. A single Kondo resonance is forming that has the shape of a single impurity resonance for large t'. These results agree qualitatively with the ones from [69] for antiferromagnetically coupled Kondo impurities. For different interaction strengths the influence of t' is very similar. The relation that is important for the influence of t' is the relation between t' and t.

A special case is given for $t = t'$. The three dots now form an equilateral triangle. For clusters of identical atoms in a metal this setup is of great importance [64]. Since this system is not particle-hole symmetric, the value of t' influences the occupation number. While for $t = 0$ the total occupancy of the dot is three, it approaches four as t increases. In this case the four electrons form a total spin 0 on the dot. Consequently the system does not display any Kondo effect in this case. Since the spin-spin correlations in such a frustrated system are rather weak compared to other geometries with comparable hopping parameters, t will have to be rather large for a complete suppression of the Kondo resonance.

The spectral functions shown in fig.(5.14) show exactly this behaviour. For small t they
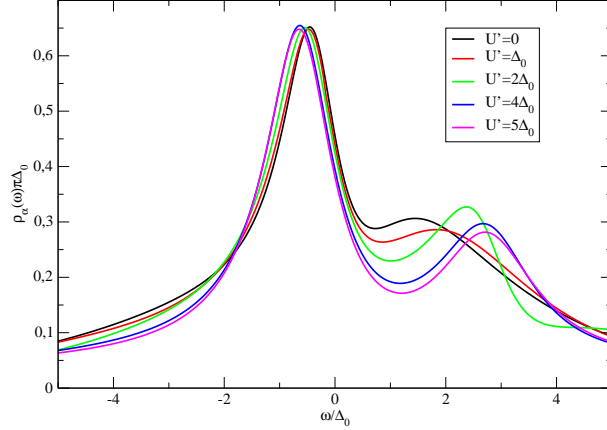
94

Figure 5.15: YTQD: Spectral functions for $U/\Delta_0 = 5$, $t = t' = \Delta_0$ and various U'.

show no great difference to the single impurity case. With growing t the Kondo resonance is suppressed due to the developing antiferromagnetic correlations that reduce the net spin of the system. The shift of the Kondo resonance is suppressed by the on-site interaction U. Only for fairly large t no resonance can be found around the chemical potential.

Due to the symmetry of the system the influence of an additional inter-dot interaction can be easily investigated in this system. Fig.(5.15) shows spectral functions for constant U and constant $t = t'$. Qualitatively the influence is the same as in the DQD system. The inter-dot interaction generates an additional effective hopping and suppresses the Kondo effect by increasing the correlations between the dots. Qualitatively the picture has changed. While in the DQD an inter-dot interaction of $U' = U$ had a major impact on the one particle dynamics and significantly suppressed the Kondo effect, here the effective mass and the width of the Kondo resonance are only influenced very slightly. This is caused by the frustration in the system. It was already stated above that the hopping has a smaller influence on this system than on non-frustrated systems. The same is true for the effective hopping. This frustration does not only suppress the influence of the hopping but also suppresses correlations caused by the inter-dot interaction. Summarizing, one can generally say that an inter-dot interaction creates an effective hopping and supports correlation effects, but that the impact on frustrated systems is much smaller than on other systems.

5.3 Summary

In this chapter the single particle dynamics of quantum dot systems described by an Anderson impurity Hamiltonian were calculated using fRG. After a brief description of the technical details needed to derive fRG flow equations for these systems, spectral properties for four different systems were presented.

The first system that was investigated was not a typical QD system but a SU(N) symmetric SIAM. In the QD framework this model describes N dots without an inter-dot hybridization with every dot being coupled to its own lead. The inter-dot interaction is equal to the on-site interaction. Besides its application on rare-earth impurity systems, this model can serve as a benchmark for the ability of fRG to correctly describe the influence of an inter-dot interaction on the one-particle dynamics. It was shown that, while 2PTh completely fails to include the inter-dot interaction, fRG correctlydescribes the impact of the inter-dot interaction on the one-particle dynamics.

The second system studied was a linear double quantum dot. The spectral properties were analyzed depending on the strength of the hopping between the dots, an external gate voltage and an inter-dot interaction. It was found that the system can be in three different phases depending on the strength of the inter-dot coupling. For a weak coupling a Kondo singlet phase was observed. At intermediate couplings the two dots form a local singlet before going over to a molecular orbital phase at large couplings. These three phases could be identified in the spectral functions of the system. The inter-dot interaction was found to create an effective hopping and to enhance coupling effects.

In the next section a linear triple quantum dot was analyzed. Like the DQD it has three phases depending on the strength of the hopping parameter: a two stage Kondo effect phase for small couplings, a phase where the three dots form an antiferromagnetic spin chain and a MO phase. In the TSK phase the local moments on all three dots are individually screened but with a much smaller Kondo temperature on the middle dot. In the AFM phase the three spins bind into a rigid spin chain and the total spin is screened. The MO phase is characterized by a Kondo resonance on the outer dots due to the screening of an unpaired electron in the antibonding orbital.

The last system studied was a TQD with a Y-shaped geometry. Three dots are coupled to individual leads and are coupled by a direct hopping between the dots. If there is no direct coupling between the dots 1 and 3, the system can be in two different phases depending on the strength of the hopping parameter. For small hoppings a Kondo singlet

phase is found. With a growing hopping parameter, the system crosses over to a MO phase that behaves very similarly to the MO phase in the linear TQD. Additionally the influence of a hopping between the dots 1 and 3 was studied. In this system frustration effects between the spins become relevant. It was found that these frustrations suppress the correlation effects. If the hopping between the dots 1 and 3 is large, these dots form a dimer behaving like a DQD, while the third dot displays an individual Kondo effect.

The special case of three impurities on an equilateral triangle was studied, depending on the strength of the hopping parameter. It was found that for large t the system was occupied by four electrons with a total spin 0. Consequently the spectral function of such a system shows no Kondo resonance for large t. Additionally the impact of an inter-dot interaction was analyzed in this system. The result was that the qualitative effect is the same as in the DQD case, i.e. an effective hopping is created and the Kondo effect is suppressed. Quantitatively the impact of an inter-dot interaction is much smaller than in the DQD case because of the frustration of the spins.

Summarizing, fRG was found to be capable of correctly describing single-particle dynamics in quantum dot systems, as long as the systems are not dominated by strong coupling physics. Especially in three dot systems up to now spectral functions and other dynamical properties have only been calculated in very special cases. Using fRG, it was possible to calculate spectral functions for systems that have been analyzed only by their static properties up to now.

Chapter 6

Conclusion and Outlook

In this work the functional renormalization group scheme was successfully used to calculate the one-particle dynamics of Anderson-like impurity models. First, the general framework of the fRG was presented. The flow equations for the self-energy, the two-particle vertex and selected observables were derived for an arbitrary fermionic system.

In the next chapter the fRG was applied to the Single Impurity Anderson Model. A brief description of the technical proceedings was given. The results from fRG were compared to second order perturbation theory, which can be recovered from fRG and to NRG. The flow equations were used to analytically calculate the self-energy and the two-particle vertex in 2PTh. It was found that fRG is capable of reliably describing the single particle dynamics of the SIAM for small and intermediate interaction strengths. In the strong coupling regime it loses accuracy. Unlike 2PTh the fRG scheme works equally well in different parameter regimes. While perturbation theory loses accuracy very quickly if the system is away from particle-hole symmetry, fRG keeps its accuracy for values away from $\epsilon_d = -U/2$. Apart from the self-energy and spectral functions, selected observables were calculated and compared. The earlier results, that fRG is a reliable tool as long as the interaction is not too strong, were validated. Finally possible approximations to the full fRG scheme were discussed. In particular one scheme was presented, that kept most of the benefits from fRG, while reducing the numerical effort considerably.

Chapter 4 dealt with the Two Impurity Anderson Model with a linear tight binding chain and with a 3d free electron gas as electronic hosts. After a short description of technical details, fRG was used to calculate spectral properties and selected observables. In particular the interplay between a coupling of the impurity spins due to a RKKY-interaction

and the Kondo effect caused by the on-site interaction was studied. In the case of the linear chain it was found that both, an increased interaction strength at a constant inter-impurity distance as well as an increased distance at a given interaction, do not lead to an individual Kondo screening. In this system the antiferromagnetic RKKY-interaction always has a relevant impact on the single particle dynamics. Using the 3d electron gas as electronic host, the behaviour was completely different. Due to the fast decay of the spin-spin correlations with growing inter-impurity distance, the dynamics of the system were dominated by an individual Kondo screening of the impurity spins already for rather small inter-impurity distances.

In chapter 5 the Anderson model was used to calculate the dynamics of quantum dot systems. Four different types of systems were studied. First, a $SU(N)$-symmetric SIAM was analyzed. In the QD-framework this system consists of N dots, with each dot coupled to its own lead. The dots do not have a hybridization between them, but the inter-dot interaction is as strong as the on-site interaction. The application of this model is found rather in rare-earth impurity systems, but it can be used very well to analyze the ability of fRG to treat an inter-dot interaction. It was found that while 2PTh completely fails to correctly describe the effects of such an inter-dot interaction on the single-particle dynamics, fRG was able to give correct results here.

The next system studied was a linear double quantum dot. Depending on the strength of the inter-dot hopping this system displays three different phases. A Kondo singlet phase, where both spins are screened individually, a local singlet phase, where the spin-spin correlations increase and a molecular orbital phase. In the local singlet phase, the system behaves almost like two single dot systems. In the local singlet phase, the spectral function shows a splitting of the Kondo resonance due to a shift in the even and odd parity channel. For large t, in the molecular orbital phase, the system has a doubly occupied even orbital and an empty odd orbital. Additionally the influence of an external gate voltage and an inter-dot interaction on the single particle dynamics were studied.

A linear triple quantum dot was studied next. Again the dependence on the hopping strength was analyzed. Like the DQD this system has three different phases. A two-stage Kondo effect phase, where the spins on all three dots are screened individually but with a much lower Kondo temperature on the middle dot, a phase where the spins bind into a antiferromagnetic spin chain and a molecular orbital phase. In the MO phase two electrons occupy the bonding orbital and one electron is in the antibonding orbital. The antibonding electron causes a Kondo resonance on the outer dots.

Finally a triple quantum dot with a Y-shaped geometry was analyzed. If the outer dots are not directly connected, the system behaves very similar to the linear TQD, but does not show an AFM phase. The individual Kondo resonance on the outer dots is directly transformed into the Kondo resonance of the antibonding electron with growing t. The resonance on the middle dot is split and smoothly transforms to the molecular orbital resonances.

The inclusion of a direct hopping between the outer dots causes frustration effects. If the hopping between the dots 1 and 3 gets very large, these two behave like a dimer, while the third dot shows an individual Kondo effect.

In the special situation of all three dots being on an equilateral triangle, the increase of the hopping causes the total occupancy to approach four. The total spin of the three dots consequently approaches zero, suppressing all Kondo effects in the system. For this symmetric situation the influence of an inter-dot interaction was studied once again. Like in the DQD case it strengthens correlation effects and creates an effective hopping, but the quantitative effect in frustrated systems is much smaller than in non-frustrated systems.

Up to now, the dynamics in TQDs or systems with three impurities have only been studied in very special situations and usually in the Kondo limit. Using fRG it was possible to calculate spectral function for three Anderson impurities in various situations.

It has been shown throughout this work that the truncated fRG scheme used here is capable of reliably calculating dynamical properties of zero-dimensional quantum impurity systems if the interaction strength is not too strong. The SIAM has been used as a benchmark. Unlike NRG, fRG cannot capture exponential behaviour in the strong coupling regime, but also unlike NRG, it is applicable to systems with two and more impurities without losing accuracy. Although the truncation of the scheme used here is motivated by perturbation theory, it does not show the drawbacks of perturbation theory. In the absence of particle-hole symmetry or with an included inter-impurity interaction, fRG works as good as for the symmetric SIAM, if not better. In more complex systems, where the Kondo temperature is raised, due to antiferromagnetic couplings, fRG works even better. In systems with strong ferromagnetic couplings fRG does not work very well. The inclusion of a magnetic field has already been presented when calculating the static spin susceptibility for the SIAM. With a suitable parametrization of the two-particle vertex an inclusion of Hund's coupling should be possible. An extension to finite temperatures should also be possible, especially using the approximation scheme App3 presented in chapter 3. With this approximation scheme the treatment of systems with four, five or

even six impurities should be possible without losing accuracy.

Already the study of the triple quantum dots made it clear that with increased number of impurities, the number of possible geometries and parameters rises very quickly. The fRG scheme used here does not require any special geometries or symmetries. It should be possible to treat a broad variety of problems with this scheme in the future.

Appendix A

Padé Approximation

A problem that turns up when using fRG, is the analytic continuation of the numerical data for e.g. the self-energy to the real axis. This is generally an ill posed problem and therefore no 'solution' can be offered. Nevertheless it is possible to obtain data for the real axis, by calculating an analytically known approximation to the numerical data and performing the analytic continuation on this approximation. The easiest and most often used approximation technique, polynomial approximation is of no great use here for two reasons. First a polynomial is not able to describe poles in the complex plane and second a polynomial will always go to $\pm\infty$ as the frequencies go to infinity. The functions considered in the context of this work will rather go to zero instead to infinity for large frequencies. A better way of approximation that includes existing poles and displays the right behaviour for large frequencies is a rational approximation, e.g. to use a quotient of two polynomials as approximant. If the power series of the original function agrees with the power series of the approximant to highest possible order, such a rational approximation is called *Padé approximation*. A basic introduction in rational interpolation and Padé approximation can be found in [25].

One problem using Padé approximation is that most algorithms need the coefficients of the power series of the function to be approximated. Although these coefficients can be determined from numerical data, this is not a stable process. To overcome this problem a method presented in ref.[30] is used in this work that determines the value of the approximant without calculating any coefficients. This method is used throughout this work.

Still, the question of accuracy and stability arises. It turns out, that although the presented scheme usually works rather well, it occasionally produces results that are clearly

unphysical and for larger interaction strengths the details of the results show a dependence on the frequency mesh of the supplied data.

In this work two ways of judging the reliability of data from Padé approximation have been used. First, if repeated calculations with changed frequency mesh give the same result, this result is considered reliable. The second option is perform a spline interpolation on the numerical data and to choose the data used for continuation from this approximation. If the result is stable for different choices of data sets, the approximation seems reliable. It turned out that for small frequencies the results are very stable and reliable. The width and lineshape of the central resonance of the spectral function can be calculated very accurately with this method. In the region of the atomic peaks the results can give a qualitative picture but are not stable enough for a quantitative analysis.

Appendix B

Approximative fRG Scheme

In chapter 3 a approximation to the full fRG scheme was presented and discussed. It was shown that this scheme is able to reproduce most of the features from the truncated fRG scheme without any further approximations. Especially the low-energy region is described very well with this scheme. A detailled description of how to derive this scheme is given here.

The starting point are the full fRG eqs.(3.9) and (3.10). First, the frequencies $\omega_1', \omega_2', \omega_1$ and $\omega_2 = \omega_1' + \omega_2' - \omega_1$ are replaced by

$$
\begin{aligned}
\nu_1 &= \omega_1' + \omega_2', \\
\nu_2 &= \omega_1' - \omega_1, \\
\nu_3 &= \omega_2' - \omega_1.
\end{aligned}
\tag{B.1}
$$

The frequency dependent part of the two-particle vertex can then be written as

$$
\mathcal{U}^\Lambda(i\omega_1', i\omega_2'; i\omega_1, i\omega_2) = \tilde{\mathcal{U}}^\Lambda(i\nu_1, i\nu_2, i\nu_3).
\tag{B.2}
$$

The flow equations can be expressed in the new $\tilde{\mathcal{U}}^\Lambda$ as well. For the self-energy it reads:

$$
\frac{d}{d\Lambda}\Sigma_\sigma^\Lambda(i\omega) = -\frac{1}{2\pi}\sum_{\alpha=\pm 1}\frac{1}{G_\sigma^{(0)}(i\alpha\Lambda)^{-1} - \Sigma_\sigma^\Lambda(i\alpha\Lambda)}\Big[2\tilde{\mathcal{U}}^\Lambda(i\omega + i\alpha\Lambda, 0, i\alpha\Lambda - i\omega) - \tilde{\mathcal{U}}^\Lambda(i\alpha\Lambda + i\omega, i\alpha\Lambda - i\omega, 0)\Big]
\tag{B.3}
$$

The next step is to write $\tilde{\mathcal{U}}^\Lambda(i\nu_1, i\nu_2, i\nu_3)$ as a sum

$$\tilde{\mathcal{U}}^\Lambda(i\nu_1, i\nu_2, i\nu_3) = \tilde{\mathcal{U}}_1^\Lambda(i\nu_1, i\nu_2, i\nu_3) + \tilde{\mathcal{U}}_2^\Lambda(i\nu_1, i\nu_2, i\nu_3) + \tilde{\mathcal{U}}_3^\Lambda(i\nu_1, i\nu_2, i\nu_3) + U \ . \quad \text{(B.4)}$$

By the addition of U in the end the initial condition of all three $\tilde{\mathcal{U}}_i^\Lambda$ becomes zero. The $\tilde{\mathcal{U}}_i^\Lambda$ represent the three parts of the flow equations: the particle-particle channel, the particle-hole channel and the particle-hole' channel. Their flow equations are

$$\frac{d}{d\Lambda}\tilde{\mathcal{U}}_1^\Lambda(i\nu_1, i\nu_2, i\nu_3) = -\frac{1}{2\pi}\int_{-\infty}^{\infty} d\nu \left[\mathcal{P}^\Lambda(i\nu, i\nu_1 - i\nu) \right. \qquad \text{(B.5)}$$

$$\left(-\tilde{\mathcal{U}}^\Lambda(i\nu_1, i\nu - \tfrac{1}{2}(i\nu_1 - i\nu_2 - i\nu_3), \tfrac{1}{2}(i\nu_1 + i\nu_2 + i\nu_3) - i\nu) \right.$$

$$\tilde{\mathcal{U}}^\Lambda(i\nu_1, i\nu - \tfrac{1}{2}(i\nu_1 + i\nu_2 - i\nu_3), i\nu - \tfrac{1}{2}(i\nu_1 - i\nu_2 + i\nu_3))$$

$$-\tilde{\mathcal{U}}^\Lambda(i\nu_1, \tfrac{1}{2}(i\nu_1 + i\nu_2 + i\nu_3) - i\nu, i\nu - \tfrac{1}{2}(i\nu_1 - i\nu_2 - i\nu_3))$$

$$\left. \left. \tilde{\mathcal{U}}^\Lambda(i\nu_1, i\nu - \tfrac{1}{2}(i\nu_1 - i\nu_2 + i\nu_3), i\nu - \tfrac{1}{2}(i\nu_1 + i\nu_2 - i\nu_3)) \right) \right] ,$$

$$\frac{d}{d\Lambda}\tilde{\mathcal{U}}_2^\Lambda(i\nu_1, i\nu_2, i\nu_3) = -\frac{1}{2\pi}\int_{-\infty}^{\infty} d\nu \left[+\left\{ \mathcal{P}^\Lambda(i\nu, i\nu_2 + i\nu) \right. \right. \qquad \text{(B.6)}$$

$$\left(2\mathcal{U}^\Lambda(i\nu + \tfrac{1}{2}(i\nu_1 + i\nu_2 - i\nu_3), i\nu_2, i\nu - \tfrac{1}{2}(i\nu_1 - i\nu_2 - i\nu_3)) \right.$$

$$\tilde{\mathcal{U}}^\Lambda(i\nu + \tfrac{1}{2}(i\nu_1 + i\nu_2 + i\nu_3), -i\nu_2, i\nu - \tfrac{1}{2}(i\nu_1 - i\nu_2 + i\nu_3))$$

$$-\tilde{\mathcal{U}}^\Lambda(i\nu + \tfrac{1}{2}(i\nu_1 + i\nu_2 - i\nu_3), i\nu_2, i\nu - \tfrac{1}{2}(i\nu_1 - i\nu_2 - i\nu_3))$$

$$\tilde{\mathcal{U}}^\Lambda(i\nu + \tfrac{1}{2}(i\nu_1 + i\nu_2 + i\nu_3), i\nu - \tfrac{1}{2}(i\nu_1 - i\nu_2 + i\nu_3), -i\nu_2)$$

$$-\tilde{\mathcal{U}}^\Lambda(i\nu + \tfrac{1}{2}(i\nu_1 + i\nu_2 - i\nu_3), i\nu - \tfrac{1}{2}(i\nu_1 - i\nu_2 - i\nu_3), i\nu_2)$$

$$\left. \tilde{\mathcal{U}}^\Lambda(i\nu + \tfrac{1}{2}(i\nu_1 + i\nu_2 + i\nu_3), -i\nu_2, i\nu - \tfrac{1}{2}(i\nu_1 - i\nu_2 + i\nu_3)) \right)$$

$$\left. \left. +(\nu_2 \leftrightarrow -\nu_2; \nu_3 \leftrightarrow -\nu_3) \right\} \right]$$

and

$$\frac{d}{d\Lambda}\tilde{\mathcal{U}}_3^\Lambda(i\nu_1, i\nu_2, i\nu_3) = -\frac{1}{2\pi}\int_{-\infty}^{\infty} d\nu \left[-\left\{\mathcal{P}^\Lambda(i\nu, i\nu_3 + i\nu)\right.\right. \tag{B.7}$$

$$\tilde{\mathcal{U}}^\Lambda(i\nu + \tfrac{1}{2}(i\nu_1 - i\nu_2 + i\nu_3), i\nu - \tfrac{1}{2}(i\nu_1 - i\nu_2 - i\nu_3), i\nu_3)$$

$$\tilde{\mathcal{U}}^\Lambda(i\nu + \tfrac{1}{2}(i\nu_1 + i\nu_2 + i\nu_3), i\nu - \tfrac{1}{2}(i\nu_1 + i\nu_2 - i\nu_3), -i\nu_3)$$

$$\left.\left.+(\nu_2 \leftrightarrow -\nu_2; \nu_3 \leftrightarrow -\nu_3)\right\}\right] .$$

It is important to note, that up to here, no approximation has been made. The approximation is made by setting

$$\tilde{\mathcal{U}}_1^\Lambda(i\nu_1, i\nu_2, i\nu_3) = \tilde{\mathcal{U}}_1^\Lambda(i\nu_1, 0, 0),$$

$$\tilde{\mathcal{U}}_2^\Lambda(i\nu_1, i\nu_2, i\nu_3) = \tilde{\mathcal{U}}_2^\Lambda(0, i\nu_2, 0),$$

$$\tilde{\mathcal{U}}_3^\Lambda(i\nu_1, i\nu_2, i\nu_3) = \tilde{\mathcal{U}}_3^\Lambda(0, 0, i\nu_3). \tag{B.8}$$

This approximation reduces the 3-dimensional frequency mesh to three one-dimensional ones, which reduces the numerical effort hugely. In second order perturbation theory this relation is fulfilled exactly. Therefore the results from the approximative scheme are still correct up to order U^2.

Appendix C

TIAM Flow Equations

In chapter 4 a very brief description of the flow equations for the frequency dependent functions in the two-particle vertex was given. Here the derivation of the flow equation for $\mathcal{U}_1^\Lambda$ is presented as a example.

Starting with the parametrization of the two-particle vertex as given in eq.(4.9) and the flow equation for the two particle vertex (eq.(2.26)) the first step is to set the external spin indices to

$$m_1' = m_2' = m_1 = m_2 \tag{C.1}$$

This leaves the derivative of $\mathcal{M}_1^\Lambda$ on the lhs of eq.(2.26) and the rhs has to be evaluated. On the rhs the terms

$$\bar{\gamma}_2^\Lambda(\xi, \xi'; \xi_1, \xi_2) \bar{\gamma}_2^\Lambda(\xi_1', \xi_2'; \xi', \xi)$$

$$= [\delta_{m_1,m}\delta_{m_1,m'}\delta_{m_1,m_1} \ \mathcal{M}_1^\Lambda + \delta_{m_1,m}\delta_{m_1,m'}\delta_{m_1,\bar{m}_1} \ \mathcal{M}_2^\Lambda - \delta_{m_1,m'}\delta_{m_1,m}\delta_{m_1,\bar{m}_1} \ \mathcal{M}_3^\Lambda$$

$$+ \delta_{m_1,m_1}\delta_{m,m'}\delta_{m_1,\bar{m}} \ \mathcal{M}_4^\Lambda]$$

$$[\delta_{n',m_1}\delta_{n,m_1}\delta_{n',n} \ \mathcal{M}_1^\Lambda + \delta_{n',m_1}\delta_{n,m_1}\delta_{n',\bar{n}} \ \mathcal{M}_2^\Lambda - \delta_{n',m_1}\delta_{n,m_1}\delta_{n',\bar{n}} \ \mathcal{M}_3^\Lambda$$

$$+ \delta_{n',n}\delta_{m_1,m_1}\delta_{n',\bar{m}_1} \ \mathcal{M}_4^\Lambda],$$

$$\bar{\gamma}_2^\Lambda(\xi_1', \xi; \xi_1, \xi')\bar{\gamma}_2^\Lambda(\xi_2', \xi'; \xi_2, \xi)$$

$$= [\delta_{m_1,m_1}\delta_{m',m}\delta_{m_1,m'}\,\mathcal{M}_1^\Lambda + \delta_{m_1,m_1}\delta_{m',m}\delta_{m_1,\bar{m}'}\,\mathcal{M}_2^\Lambda - \delta_{m_1,m}\delta_{m',m_1}\delta_{m_1,\bar{m}'}\,\mathcal{M}_3^\Lambda$$

$$+\delta_{m_1,m'}\delta_{m_1,m}\delta_{m_1,\bar{m}_1}\,\mathcal{M}_4^\Lambda]$$

$$[\delta_{m_1,m_1}\delta_{n,n'}\delta_{m_1,n}\,\mathcal{M}_1^\Lambda + \delta_{m_1,m_1}\delta_{n,n'}\delta_{m_1,\bar{n}}\,\mathcal{M}_2^\Lambda - \delta_{m_1,n'}\delta_{n,m_1}\delta_{m_1,\bar{n}}\,\mathcal{M}_3^\Lambda$$

$$+\delta_{m_1,n}\delta_{m_1,n'}\delta_{m_1,\bar{m}_1}\,\mathcal{M}_4^\Lambda]$$

and

$$\bar{\gamma}_2^\Lambda(\xi_2', \xi; \xi_1, \xi')\bar{\gamma}_2^\Lambda(\xi_1', \xi'; \xi_2, \xi)$$

$$= [\delta_{m_1,m_1'}\delta_{m',m}\delta_{m_1,m'}\,\mathcal{M}_1^\Lambda + \delta_{m_1,m_1'}\delta_{m',m}\delta_{m_1,\bar{m}'}\,\mathcal{M}_2^\Lambda - \delta_{m_1,m}\delta_{m',m_1'}\delta_{m_1,\bar{m}'}\,\mathcal{M}_3^\Lambda$$

$$+\delta_{m_1,m'}\delta_{m_1',m}\delta_{m_1,\bar{m}_1'}\,\mathcal{M}_4^\Lambda]$$

$$[\delta_{m_1,m_1}\delta_{n,n'}\delta_{m_1,n}\,\mathcal{M}_1^\Lambda + \delta_{m_1,m_1}\delta_{n,n'}\delta_{m_1,\bar{n}}\,\mathcal{M}_2^\Lambda - \delta_{m_1,n'}\delta_{n,m_1}\delta_{m_1,\bar{n}}\,\mathcal{M}_3^\Lambda$$

$$+\delta_{m_1,n}\delta_{m_1,n'}\delta_{m_1,\bar{m}_1}\,\mathcal{M}_4^\Lambda]$$

appear in the three channels. Eq.(C.1) has already been used here. The evaluation of the sum over m, m', n and n'. Gives eq.(4.10). For a further evaluation, the external spins are set to be

$$\sigma_1 = \sigma_1' \neq \sigma_2 = \sigma_2'. \tag{C.2}$$

On the lhs the derivative of $\mathcal{U}_1^\Lambda$ remains. On the rhs the spin sums over σ and σ' with terms like $(x_i = (\sigma_i, i\omega_i))$

$$\mathcal{M}(x, x'; x_1, x_2)\mathcal{M}(x_1', x_2'; x', x)$$

$$= (\delta_{\sigma_1,\sigma}\delta_{\sigma_2,\sigma'}\,\mathcal{U}_1^\Lambda + \delta_{\sigma_1,\sigma}\delta_{\sigma_2,\sigma'}\,\mathcal{U}_2^\Lambda)(\delta_{\sigma',\sigma_1'}\delta_{\sigma,\sigma_2'}\,\mathcal{U}_1^\Lambda + \delta_{\sigma',\sigma_1'}\delta_{\sigma,\sigma_2'}\,\mathcal{U}_2^\Lambda), \qquad \text{(C.3)}$$

$$\mathcal{M}(x_1',x;x_1,x')\mathcal{M}(x_2',x';x_2,x)$$

$$= (\delta_{\sigma_1,\sigma_1'}\delta_{\sigma',\sigma}\,\mathcal{U}_1^\Lambda + \delta_{\sigma_1,\sigma_1'}\delta_{\sigma',\sigma}\,\mathcal{U}_2^\Lambda)(\delta_{\sigma_2,\sigma_2'}\delta_{\sigma,\sigma'}\,\mathcal{U}_1^\Lambda + \delta_{\sigma_2,\sigma_2'}\delta_{\sigma,\sigma'}\,\mathcal{U}_2^\Lambda) \qquad \text{(C.4)}$$

and

$$\mathcal{M}(x_2',x;x_1,x')\mathcal{M}(x_1',x';x_2,x)$$

$$= (\delta_{\sigma_1,\sigma_2'}\delta_{\sigma',\sigma}\,\mathcal{U}_1^\Lambda + \delta_{\sigma_1,\sigma_2'}\delta_{\sigma',\sigma}\,\mathcal{U}_2^\Lambda)(\delta_{\sigma_2,\sigma_1'}\delta_{\sigma,\sigma'}\,\mathcal{U}_1^\Lambda + \delta_{\sigma_2,\sigma_1'}\delta_{\sigma,\sigma'}\,\mathcal{U}_2^\Lambda) \qquad \text{(C.5)}$$

have to be evaluated. The result looks very similar to eq.(3.10) but the total number of terms is increased approximately by a factor of four. To derive flow equations for the other $\mathcal{U}_i^\Lambda$ the external impurity indices and spins have to be set accordingly.

Bibliography

[1] K.G. Wilson, Rev. Mod. Phys. **47**, 773 (1975).

[2] J. Polchinski, Nucl. Phys. B **231**, 269 (1984).

[3] F.J. Wegner and A. Houghton, Phys. Rev. A **8**, 401 (1973).

[4] C. Wetterich, Phys. Lett. B **301**, 90 (1993).

[5] T.R. Morris, Int. J. Mod. Phys. A **9**, 2411 (1994).

[6] C. Wieczerkowski, Commun. Math. Phys. **120**, 149 (1988).

[7] M. Salmhofer, *Renormalization* (Springer, 1998).

[8] D. Zanchi and H.J. Schulz, Phys. Rev. B **61**, 13609 (2000).

[9] C.J. Halboth and W. Metzner, Phys. Rev. B **61**, 7364 (2000).

[10] C. Honerkamp, M. Salmhofer, N. Furukawa and T.M. Rice, Phys. Rev. B **63**, 035109 (2001).

[11] T. Busche, L. Bartosch and P. Kopietz, J. Phys.: Condens. Matter **14**, 8513 (2002).

[12] V. Meden, W. Metzner, U. Schollwöck and K. Schönhammer, Phys. Rev. B **65**, 045318 (2002).

[13] V. Meden, W. Metzner, U. Schollwöck and K. Schönhammer, J. Low Temp. Phys. **126**, 1147 (2002).

[14] S. Andergassen, T. Enss, V. Meden, W. Metzner, U. Schollwöck and K. Schönhammer, Phys. Rev. B **70**, 075102 (2004).

[15] S. Andergassen, T. Enss and V. Meden, Phys. Rev. B **73**, 153308 (2006).

[16] C. Karrasch, T. Enss and V. Meden, Phys. Rev. B **73**, 235337 (2006).

[17] J.W. Negele and H. Orland, *Quantum Many-Particle Physics* (Addison-Wesley, 1988).

[18] A.A. Katanin, Phys. Rev. B **70**, 115109 (2004).

[19] P.W. Anderson, Phys. Rev. **124**, 41 (1961).

[20] R. Schrieffer and P.A. Wolff, Phys. Rev. **149**, 491 (1966).

[21] J. Kondo, Prog. Theo. Phys. **32**, 37 (1964).

[22] A.C. Hewson in D. Edwards and D. Melville, eds., *The Kondo Problem to Heavy Fermions* (Cambridge University Press, 1993).

[23] H.R. Krishnamurthy, J.W. Wilkins and K.G. Wilson, Phys. Rev. B**21**, 1003 (1980).

[24] H. Keiter, J.C. Kimball, Int. J. Magn. **1**, 233 (1971).

[25] W.H. Press et al., *Numerical Recipes in C* (Cambridge University Press, 1993).

[26] D. Logan, M. Eastwood and M. Tusch, J. Phys.: Condens. Matter **10**, 2673 (1998).

[27] D. Logan and M. Glossop, J. Phys.: Condens. Matter **12**, 985 (2000).

[28] V. Meden and U. Schollwöck, Phys. Rev. B **67**, 035106 (2003).

[29] R. Hedden, V. Meden, Th. Pruschke and K. Schönhammer, J. Phys.: Condensed Matter **16**, 5279 (2004).

[30] H.J. Vidberg and J.W. Serene, J. Low Temp. Phys., **29**, 3/4 (1977).

[31] V. Zlatić and B. Horvatić, Phys. Rev. B **28**, 6905 (1983).

[32] B. Kjöllerström, D.J. Scalapino and J.R. Schrieffer, Phys. Rev. **148**, 665 (1966).

[33] P. Nozières, J. Low-Temp. Phys. **17** 31 (1974).

[34] T.C. Li, O. Gunnarsson, K. Schönhammer and G. Zwicknagl, J. Phys. C: Solid State Phys. **20** 405-417 (1987).

[35] K. Yamada, Progr. Theor. Phys. **53** 970 (1975).

[36] Y.C. Tsay and M.W. Klein, Phys. Rev. B **7**, 352 (1973).

[37] C. Jayaprakash, H.R. Krishnamurthy and J.W. Wilkins, J. Appl. Phys. **53**, 2142 (1982).

[38] S. Chakravarty and J.E. Hirsch, Phys. Rev. B **25**, 3273 (1982).

[39] R.M. Fye, J.E. Hirsch and D.J. Scalapino, Phys. Rev. B **35**, 4901 (1987).

[40] B.A. Jones, B.G. Kotliar and A.J. Millis, Phys. Rev. B **39**, 3415 (1989).

[41] O. Sakai, Y. Shimizu and T. Kasuya, Solid State Comm. **75**, 2, 81-87 (1990).

[42] T. Saso, Phys. Rev. B **44**, R450 (1991).

[43] T. Saso and H. Kato, Prog. Theo. Phys. **87**, 331 (1992).

[44] L.C. Andreani and H. Beck, Phys. Rev. B **48**, 7322 (1993).

[45] A. Schiller and V. Zevin, Phys. Rev. B **47**, 14297 (1993).

[46] G.E. Santoro and G.F. Guiliani, Phys. Rev. B **49**, 6746 (1994).

[47] W. Klein, G. Xianlong and L. Ji, Phys. Rev. B **60**, 15492 (1999).

[48] C.A. Büsser, A.L. Lima, M.A. Davidovich and G. Chiappe, Phys. Rev. B **62**, 9907 (2000).

[49] T.I. Ivanov, Phys. Rev. B **62**, 12577 (2000).

[50] A.M.J.C. Neto and R.E. Lagos, Physica B **312-313**, 176 (2002).

[51] R. Aguado and D.C. Langreth, Phys. Rev. B **67**, 245307 (2003).

[52] P. Durganandini, Phys. Rev. B **74**, 155309 (2006).

[53] S. Nishimoto, Th. Pruschke and R.M. Noack, J. Phys.: Condens. Matter **18**, 981 (2006).

[54] T.T. Ong and B.A. Jones, cond-mat 0602223 (2006).

[55] R.M. Fye and J.E. Hirsch, Phys. Rev. B **40**, 4780 (1989).

[56] R.M. Fye, Phys. Rev. Lett. **61**, 125 (1994).

[57] B.A. Jones and C.M. Varma, Phys. Rev. Lett. **58**, 843 (1987).

[58] B.A. Jones, C.M. Varma and J.W. Wilkins, Phys. Rev. B **61**, 125 (1988).

[59] B.A. Jones and C.M. Varma, Phys. Rev. B **40**, 324 (1989).

[60] I. Affleck and A.W.W. Ludwig, Phys. Rev. Lett. **68**, 1046 (1992).

[61] I. Affleck, A.W.W. Ludwig and B.A. Jones, Phys. Rev. B **52**, 9528 (1995).

[62] A.C. Hewson and J.W. Rasul, J. of Magnetism a. Magnetic Mat. **47**, 339 (1985).

[63] H. Jeong, A.M. Chang and M.R. Melloch, Science **293**, 2221 (2001).

[64] T. Jamneala, V. Madhavan and M.F. Crommie, Phys. Rev. Lett. **87**, 256804 (2001).

[65] D. Boese, W. Hofstaetter and H. Schoeller, Phys. Rev. B **66**, 125315 (2002).

[66] R. Zitko and J. Bonca, Phys. Rev. B **74**, 045312 (2006).

[67] W. Izumida and O. Sakai, Phys. Rev. B **62**, 10260 (2000).

[68] B.R. Bulka and T. Kostyrko , Phys. Rev. B **70**, 205333 (2004).

[69] V.V. Savkin, A.N. Rubtsov, M.I. Katsnelson and A.I. Lichtenstein, Phys. Rev. Lett. **94**, 026402 (2005).

[70] R. Zitko, J. Bonca, A. Ramsak and T. Rejec, Phys. Rev. B **73**, 153307 (2006).

[71] R. Zitko and J. Bonca, Phys. Rev. B **74**, 045312 (2006).

Acknowledgements

This thesis could not have been realized without the contribution of several people. They helped me solve problems that occured or posed new ones that lead to new insight. Some people had nothing to do with problems but enabled me to deal with them. I am very grateful to all of these people.

Many, many thanks to all of you!

Curriculum Vitae

16.2.1977	Geboren in Oldenburg (Oldb.) als Sohn von Karl Hedden und Christa Hedden, geb. Duwe
August 1983 bis Juli 1987	Besuch der Grundschule: Paulus-Grundschule in Haselünne und Grundschule Bloherfelde in Oldenburg
August 1987 bis Juli 1989	Besuch der Orientierungsstufe: Orientierungsstufe Eversten in Oldenburg
August 1989 bis Juni 1996	Besuch des Gymnasiums: Gymnasium Eversten in Oldenburg
Juni 1996	Abitur
Februar 1997 bis Februar 1998	Zivildienst in den Städtischen Kliniken Oldenburg
Oktober 1998 bis Juni 2003	Physikstudium an der Georg-August-Universität Göttingen
Sommersemster 2000	Vordiplom
Oktober 2001 bis Juni 2003	Diplomarbeit im Institut für theoretische Physik bei Prof. Schönhammer
Juni 2003	Diplomprüfung
Seit Juli 2003	Wissenschaftlicher Mitarbeiter und Beginn einer Dissertation am Institut für theoretische Physik der Universität Göttingen bei Prof. Schönhammer